No. 35, 2004

nucleus

ISBN 0864-084X

Publicación semestral

Agencia de Energía Nuclear y Tecnologías de Avanzada en Cuba

Ministerio de Ciencia, Tecnología y Medio Ambiente

En éste número:

Memorias

NURT 2003

La Habana, Cuba

SUMMARY

NUCLEAR OUTLOOK

NUCLEAR SCIENCES

Director: Manuel Fernández Rondón / **Editor Jefe:** Jorge Alvarado Cartaya / **Redactor Técnico:** Marta Contreras Izquierdo / **Edición:** Dulce María García Medina / **Diseño:** Marietta Fernández Martín / **Composición:** Magaly Cruz Jorge / **Traducción:** Lázaro O´Farrill Lazo, Odalys González Solasabal / **Referencias:** Katia González Sánchez / **Fotomecánica:** Alain Ciérvides Sánchez / **Producción:** Adolfo Estévez González, Ricardo Gavilla Moreno / **Encuadernación:** María Cristina Herrera Rosell / **Canje:** Iraida Oviedo Rivero.

Revista arbitrada. Referenciada en la Base de Datos INIS.

SUMARIO

PANORAMA NUCLEAR

CIENCIAS NUCLEARES

Publicación semestral de la **Agencia de Energía Nuclear y Tecnologías de Avanzada** del Ministerio de Ciencia, Tecnología y Medio Ambiente (CITMA).

Edición e Impresión: Cubaenergía / Calle 20 No. 4111-4113 e/ 18A y 47, Playa, Ciudad de La Habana, Cuba, CP 11300/ Apartado Postal 6317 y 6318 / Tel.: (537)2027527 / Fax: (537)204 1188 / c.e.: nucleus@cubaenergia.cu

Inscripta como impreso periódico. **Registro Nacional de Publicaciones Seriadas No. 0061**. Inscripta en la Dirección de Correos y Telégrafos con el No. 94021/184.

CEADEN: 17 YEARS AT THE SERVICE OF CUBAN SCIENCE AND TECNOLOGY

CEADEN: 17 AÑOS AL SERVICIO DE LA CIENCIA Y LA TECNOLOGÍAS CUBANAS

Dtor. Juan G. Darias González
Centro de Aplicaciones Tecnológicas y Desarrollo Nuclear (CEADEN)
Calle 30 No. 502, e/ 5ta y 7ma
Playa, Ciudad de La Habana, Cuba
email:root@ceaden.edu.cu

The Center of Technological Applications and Nuclear Development was founded in 1987 on the basis of the existing since 1976 National Institute for Nuclear Researches (ININ). CEADEN is attached to the Nuclear Energy and Advanced Technologies Agency (AENtA), and belongs to the Ministry of Science, Technology and Environmental Care (CITMA). CEADEN is also part of the West Pole of R&D institutions supervised by the Cuban State Department.

The CEADEN scientific and technological activities are focused on to the performance of basic and applied researches in the fields of nuclear and related fields, fundamental and experimental Physics, optics and laser applications. Offering high added value scientific and technical services and the construction of small parties of equipment and devices upon customer's requirements for several areas of the economics and the social life are also a major part of our activities. Our main customers are institutions or enterprises from the public health, the agriculture and the industry sectors, among others. The biotechnology and biopharmaceutical industry have become one of the major recipients of CEADEN services in the last decades, due to the high level of specialization and of the quality requirements imposed by this sector.

The Center is functionally organized in 4 Divisions (Research, Scientific & Technical Services, Instrumentation and Administration) that subordinate to the main Management Council and that are responsible for accomplishing our mission:

"To generate and commercialize products and services based on Nuclear, Optics and Laser techniques and sciences".

The high proficiency and qualification of the working personnel, as well as the following of a Quality Assurance Policy according to the ISO 9000 and ISO 9002 standards, have been the main premises for CEADEN development and growth. QAS have been implemented in all of the departments, and the main laboratories and services have been credited according to the ISO 17025 requirements.

Currently, CEADEN researchers head 33 Projects of R&D, including 2 founded by National Programs,19 from the AENtA Nuclear Program, 8

El Centro de Aplicaciones Tecnológicas y Desarrollo Nuclear, se fundó en 1987 contando como antecedente inmediato en el país, la existencia desde el año 1976 del Instituto Nacional para las Investigaciones Nucleares (ININ). El CEADEN está adscrito a la Agencia de Energía Nuclear y Tecnologías de Avanzada y pertenece al Ministerio de Ciencia, Tecnología y Medio Ambiente, es además uno de los centros del Polo Científico del Oeste que atiende el Consejo de Estado de la República de Cuba.

Las actividades científico-técnicas del CEADEN incluyen las investigaciones básicas y aplicadas de las técnicas nucleares y conexas, además de la física teórica y experimental, la óptica y el láser, también forma parte de su actividad fundamental la prestación de servicios científico-técnicos, con alto valor agregado y el desarrollo y la producción de equipos en pequeñas series, componentes y partes. Tanto los resultados de las investigaciones, como los servicios científico-técnicos y las producciones tienen aplicaciones en los diferentes sectores socio-económicos del país como son: la salud pública, la industria médico-farmacéutica, la industria en general y la agricultura, que constituyen los principales clientes del Centro.

El CEADEN está estructurado en una Dirección y cuatro subdirecciones: Investigaciones, Servicios Científico-Técnicos, Instrumentación y Administrativa, las cuales garantizan el cumplimiento satisfactorio de su misión:

"Generar y comercializar, productos y servicios a partir de la Ciencia y la Técnica Nuclear, Láser, Óptica y Conexas".

Una de las premisas principales para el desarrollo y crecimiento del CEADEN es el establecimiento de una Política de Aseguramiento de la Calidad según las Normas ISO 9000 e ISO 9002, lo cual ha garantizado la implantación del sistema de calidad en la mayoría de sus áreas de investigación, producción y servicios, así como la acreditación o certificación de sus servicios, laboratorios y ensayos fundamentales.

Actualmente, el CEADEN participa como centro cabecera en un total de 33 proyectos de investigación, de ellos 2 de Programas

from the AENtA Optics and Laser Program, 1 Project in the Environmental Care Program and 3 projects not directly associated to Programs.

The International Atomic Energy Agency (IAEA) is the main partner in the international collaboration. 3 ARCAL projects, 1 Technical Assistance Project and 3 Research Co-ordinated projects are in due course. Several CEADEN specialists often pay technical assessment to developing countries as IAEA experts. CEADEN researchers take part in bilateral collaborative projects with ININ and CIO (Mexico), EPFL (Switzerland), UA (Belgium), INFN (Italy), as well as in two international projects: ALPHA (EU) and ALICE (CERN).

Two international conferences are organized biannually to join scientists working in our fields of research: TECNOLÁSER and NURT.

TECNOLÁSER is included in the Convention and International Fair of Metallurgy, Mechanics and Recycling Industries (METÁNICA) and its scope extends to:

· Laser processing of materials.
· Laser techniques in medicine and biology.
· Optics in spectroscopy and measurement.
· Optic and laser instrumentation in mechanics and automation.
· Opto-electronics
· Laser in industrial applications
· Image processing.

The NURT Symposia (Nuclear and Related Techniques) are one of the key Cuban scientific meetings dealing with the peaceful applications of nuclear techniques in all domains of the society. They are arranged with a two-year frequency and provide a unique opportunity for the international scientific community to meet outstanding researchers and to discuss current trends and tasks in several areas of applied, nuclear related topics.

The first four editions of the NURT were organized under the auspices of the International Atomic Energy Agency in 1997, 1999, 2001 and 2003, and hosted around 150 delegates and invited scientists from more than 40 countries from all over the world. Since 2001 NURT is organized by CEADEN and joins simultaneous Workshops devoted to specific topics. Selected papers from NURT´2003 are presented in this issue of NUCLEUS.

Nacionales, 19 del Programa Ramal Nuclear, 8 del Programa Ramal de Óptica y Láser, 1 Proyecto del Programa Ramal de Medio Ambiente y 3 Proyectos no Asociados a Programas.

Desde el punto de vista internacional, el Organismo Internacional de Energía Atómica (OIEA) representa la principal institución con la cual CEADEN mantiene relaciones de colaboración, en estos momentos: 3 Proyectos ARCAL*, 1 Proyecto Nacional de Cooperación Técnica y 3 contratos dentro de los Proyectos Coordinados de Investigación. Además, especialistas del Centro participan en proyectos de colaboración internacional con el ININ y CIO de México, EPFL de Suiza, en un Proyecto ALFA patrocinado por la Unión Europea y un proyecto de la Organización Europea de Investigaciones Nucleares (CERN).

Para la confrontación entre especialistas de las diferentes temáticas que están en las líneas de investigación del CEADEN, se organizan dos eventos de carácter internacional: El TECNOLÁSER y el NURT.

TECNOLÁSER es un evento bianual que se desarrolla en el contexto de la Convención y Feria Internacional de las Industrias Metalúrgica, Mecánica y del Reciclaje, METÁNICA, y tiene entre sus temáticas principales:
· Procesamiento de materiales con láser.
· Tecnologías láser en la medicina y biología, técnicas ópticas de medición y espectroscopía.
· Instrumentación óptica, electrónica, mecánica y automatización asociadas a la técnica láser.
· Desarrollo y construcción de instalaciones láseres.
· Optoelectrónica.
· Aplicaciones del láser en la industria.
· Procesamiento de imágenes.

El Simposium NURT (Nuclear and Related Techniques) constituye un evento de gran significación para la comunidad científica nacional e internacional, por cuanto brinda una oportunidad única para discutir las tendencias actuales e importantes resultados alcanzados en las investigaciones básicas y aplicadas que se realizan en diferentes campos de aplicaciones nucleares.

Organizados con una frecuencia bianual desde 1997, las cuatro primeras ediciones de esta importante reunión han contado con una asistencia promedio de alrededor de 150 delegados, de los cuales aproximadamente la mitad provienen de numerosas instituciones de casi 40 países. Desde la tercera edición (2001) este evento se organiza en forma de talleres dedicados a temas específicos y que sesionan de forma simultánea. En este número de la revista se presentan una parte de los trabajos expuestos en el NURT 2003.

*Acuerdo Regional de Cooperación para la Promoción de la Ciencia y Tecnología Nucleares en América Latina

TXRF ANALYSIS OF Cu AND Zn IN BLOOD SERUM FROM HEMODIALYSIS PATIENTS

Román Padilla Álvarez[1], Jorge F. Pérez-Oliva[2], Iván Pupo González[1]

[1]Centro de Aplicaciones Tecnológicas y Desarrollo Nuclear (CEADEN), calle 30 No. 502, e/ 5ta Ave. y 7ma, Playa, Ciudad de La Habana, Cuba
[2]Instituto de Nefrología "Dr. Abelardo Buch López"
padilla@ceaden.edu.cu

ANÁLISIS FRXRT DE Cu Y Zn EN SUERO SANGUÍNEO DE PACIENTES CON HEMODIÁLISIS

Resumen

Durante los últimos años muchos estudios de nutrición se han concentrado en revelar la importancia del zinc y el cobre en varios procesos del metabolismo. Los pacientes que padecen de enfermedad crónica renal constituyen un grupo poblacional cuya nutrición está afectada por el proceso de diálisis. Esta investigación estuvo encaminada a determinar los niveles de concentración de zinc y cobre en pacientes con hemodiálisis que presentan un estado diferente de condición nutritiva. Se implementó y se validó un procedimiento para el análisis del suero sanguíneo por fluorescencia de rayos X por reflexión total. Los beneficios del método aplicado son su simplicidad y especificidad, asegurando una reproducibilidad y exactitud superiores al 15%. Se da una interpretación preliminar de los resultados.

Abstract

Researches to study the role of essential trace elements in the metabolism have considerably increased during the last years. Among them, nutrition studies have focused into revealing the relevance of both zinc and copper in several metabolism processes.
The patients suffering from chronic renal disease constitute a population with nutrition being affected by the process of dialysis. The present research was aimed to determine the concentration levels of zinc and copper in hemodialysis patients presenting different state of nutritional condition.
A procedure for direct total reflection X-ray fluorescence analysis of blood serum was implemented and validated. The benefits of the implemented method are its simplicity and express features, ensuring reproducibility and accuracy better than 15%. A preliminary interpretation of the results of the analysis of 60 patients is given.

Key words: blood serum, elements, X-ray fluorescence analysis, dialysis, kidneys, patients

INTRODUCTION

The attention paid to the role of metals in the biochemical processes of the human methabolism has considerably increased during the last years. Researches have focused into two major stream directions: to reveal the relevance for life metabolism of essential metals and to assess the toxicity levels of other metals and the mechanisms of their assimilation. Among the first category, an important field is the study of nutritional problems.

Undernourishment is present in a significant part of the patients suffering of different levels of chronic renal disease. An unpublished study carried out at the Hospital "Hermanos Ameijeiras" revealed that 53% of the patients undergoing hemodialysis showed symptoms of undernourishment or were about to fall into that condition.

Symptoms of energetic and/or protein depletion can be recognized in undernourished patients. The depletion on zinc or copper are not so evident, and even when they can be indirectly inferred from changes in the skin or mucus, a direct estimation is possible only by analytical methods.

The low concentration levels hamper the analysis of metals in body fluids. Most of the analytical instrumentation with sensitivity reaching the sub-ppm level is rather expensive, and therefore is often not available to institutions from developing countries. Total reflection X-ray fluorescence (TXRF) is probably one of the techniques offering a reasonable cost to benefit ratio for the intended purpose. The technique was firstly implemented at the end of the 1970's [1,2], and has been improved by several instrumental modifications [3-5]. The introduction of reflecting multilayer structured devices [6] allowed tuning the energy of the excitation radiation and drastically to reduce the

spectral background resulting from scattering by the sample of the incident radiation. Such monochromation of the excitation radiation has been of great advantage when analyzing higher density solutions, in particular biological fluids [7-9]. TXRF has been successfully applied to the analysis of biological materials [10], body fluids [11-14], biological tissues [15-21], and lately to the study of the mechanisms of action of different enzymes and pharmaceuticals [22-24].

The present study was aimed to determine the concentration levels of zinc and copper in hemodialysis patients presenting different nutritional condition. A procedure for direct TXRF analysis of blood serum was implemented and validated, being its main advantages simplicity and express feature. The procedure ensures reproducibility and accuracy better than 15%. Some tendencies in the obtained results are commented.

MATERIALS AND METHODS

The information on micro and trace elements concentration in blood serum from chronic renal disease is seldom available. The more recent results reported by a research team comparing the concentrations of trace elements in blood between patients and control subjects are summarized in two papers [25,26]. These results were used as background information in this work and are summarized in table 1.

Notes: CAPD - Patients from continuous ambulatory peritoneal dialysis
HD - patients from hemodialysis
N - number of cases

The concentration values of both copper and zinc are around one part per million, thus making TXRF a suitable technique for their analysis. In order to avoid sample dilution or contamination from reagents used in sample digestion, a direct measurement procedure was implemented.
60 individuals undergoing hemodialysis at the Instituto de Nefrología conformed the studied population. The age of the patients was between 30 and 80 years, and all of them had undergone HD treatment for more than 6 months. Individuals suffering from *Diabetes Mellitus* were excluded from the study. The patients were subdivided into two groups, corresponding to the criteria shown in table 2.

Although both creatinine and urea are not direct indexes of nutrition (in fact their values are elevated for all HD patients), the changes in time for an individual may provide and indirect measure of the nutrition. As far as creatinine is related to muscular mass, its decrease can indicate a nutritional depletion, and urea can drop to extreme low levels in cases of undernourishment.
Three rounds of sampling were conducted (November-2002, April-2003 and August-2003).

Table 1. Comparison of Zn and Cu concentrations between chronic renal disease patients and control populations

	Trace element	Patients	Controls
[25]: plasma, CAPD, N=51	Zn (µg/L)	857 ±176	1105 ±175
	Cu (µg/L)	1208 ±249	1136 ±172
[26]: blood, HD, N=151	Zn (µg/L)	688.5 ±969.1	1066.6 ±493.5
	Cu (µg/L)	1224.1 ±369.9	1070.6 ±305.9

Table 2. Criteria of differentiation between groups

Criterion	Group 1	Group 2
Subjective clinical valuation of nutritional status: Phenotype status Index of age/weight Index age/height Index of corporal mass Retraction of cutaneous fold Coloration of skin and mucus Direct indexes:	Acceptable	Depletion
Albumin level during the six months preceding the study BMI [weight (kg)/ height (cm)]^2	> 35 g/L 22 - 30	< 35 g/L < 18
Indirect indexes to assess general condition: Cholesterol: (Normal : 3.2 5.2 mmol/L; > 6.2 mmol/L) Creatinine: (Normal : 97 128 µmol/L; > 128 µmol/L) Urea: (Normal : 2.5 8.0 mmol/L; > 8.0 mmol/L)		

10 mL of blood were collected from patients in acid leached glass tubes before the start of the midweek hemodialysis session, in an effort to avoid concentrations altered by the weekend recess. The samples were allowed to settle for two days in refrigeration (8 °C) before taking the serum fraction. The collected serum was centrifuged at 3 500 rpm for five minutes and 1.8 mL were transferred to a 2 mL flask containing 200 mL of 50 mg/mL Ga solution. 5 mL of the spiked serum (final concentration of the internal standard being of 500 mg/L) were deposited and evaporated on quartz reflectors for three successive times in order to increase the counting statistics [9].

Sample evaporation was carried out in a vacuum chamber within a laminar flow cabinet to avoid contamination. Further deposition showed no increase in the measured TXRF spectrum. The concentration of each element (W_i) was calculated from the measured ratio of its fluorescent peak area (N_i) to the peak area of the internal standard (N_{st}) using the resulting internal standard concentration (W_{St}) and the linear relative sensitivity calibration curve.

$$\frac{N_i}{N_{St}/W_{St}} = \frac{S_i}{S_{St}} W_i \qquad (1)$$

RESULTS

Method validation:
A pool serum sample was used to assess the characteristics of performance of the method. The validity of TXRF 'thin' layer assumption was checked by plotting the relative increase of the fluorescent peak area while increasing the amount of deposited drops (figure 1). For Fe, Cu and Zn the relative increase in peak areas showed a good correlation on linear tendency. For lighter elements (K, Ca) this assumption is not valid, thus constraining the analysis to the determination of only those elements with energies larger than 6.4 keV (Fe-Ka).

Detection limits were calculated from expression (1) substituting the peak areas by three times the square root of the background under the peak ($3\sqrt{N_b}$). No significant improvement was noticed when depositing more than 3 drops, and a measuring time of 30 minutes was found to be a good trade off to reduce the time of the analysis without affecting the sensitivity (see figure 2).

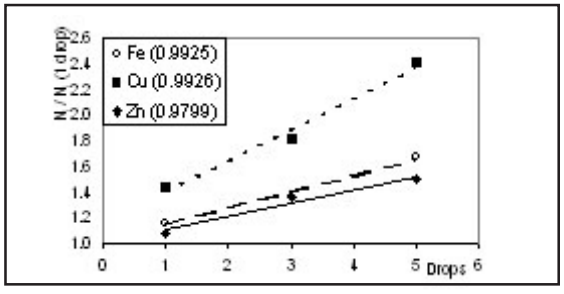

Figure 1. Validity of thin film assumption.

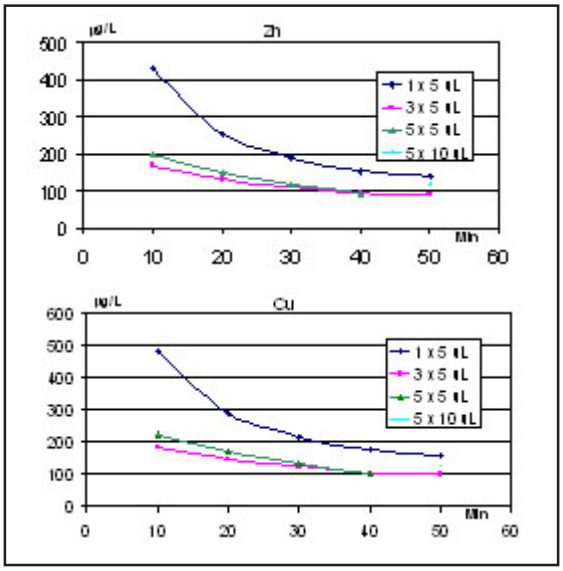

Figure 2. Detection limits achieved.

The reproducibility of the results from five different replicates was found better than 8%. The accuracy of the results was compared with two other different methods: External standard addition and Direct TXRF analysis and atomic absorption spectroscopy (AAS).

For external standard addition a series of 5 samples was prepared, with final added concentrations of 0, 500, 1000, 1500 and 2000 mg/L. Volumes of N x 0.1 mL of 50 mg/mL Fe, Cu and Zn solutions were added to 10 mL flasks (N = 0, 1, 2, 3, 4, respectively). 0.2 mL of 50 mg/mL Ga solution and 1.8 mL of the serum composite sample were added to each flask, which were completed to final volume with bi-distilled and de-ionized water.

For AAS 10 mL of the composite serum sample were heated to dryness in a platinum die. The dry residue was burned at 800 °C in an oven and dissolved with 2 mL of HNO_3 (PA). The sample was then diluted to 10 mL with bi-distilled and de-ionized water and further measured in a flame spectrometer.

The results obtained by the three independent methods are shown in table 3. The discrepancies were found to be less than 10% of the average value of the three analyses.

An assessment of the main sources contributing to the overall uncertainty of the method revealed as the most relevant the uncertainties related to peak areas *N* (analyzed element and internal standard) and relative instrumental sensitivity *S* [27]. The contribution due to reproducibility uncertainty was estimated from the relative standard deviation of five replicate analyses. A summarized budget of the uncertainties is given in table 4.

Table 3. Comparison of the results of three independent methods

Element	Direct TXRF	External standard addition + TXRF	AAS
Fe	1444 ± 112	1495 ± 163	1340 ± 106
Cu	860 ± 75	899 ± 66	930 ± 30
Zn	838 ± 52	912 ± 113	930 ± 18

Table 4. Uncertainty budget estimation

	$\frac{u_c^2(N_i)}{N_i^2}$	$\frac{u_c^2(N_{Si})}{N_{Si}^2}$	$\frac{u_c^2\left(S_i/S\right)}{\left(S_i/S\right)^2}$	$\frac{u_c^2(W_{Si})}{W_{Si}^2}$	$u_c(W_i)$	$\frac{stdev(W_i)}{W_i}$	$u_c(W_i)'$
Fe	0.0103	0.00104	0.426	0.01	0.15	0.046	0.16
Cu	0.0018	0.00104	0.769	0.01	0.13	0.021	0.13
Zn	0.0048	0.00104	0.904	0.01	0.15	0.079	0.17

The combined uncertainty of the method is calculated by the expression (2).

$$u_c(W_i)' = \sqrt{\left(\frac{stdev(W_i)}{W_i}\right)^2 + u_c^2(W_i)} \quad (2)$$

$$u_c^2(W_i) = W_i^2 \left(\frac{u_c^2(N_i)}{N_i^2} + \frac{u_c^2(N_{Si})}{N_{Si}^2} + \frac{u_c^2\left(S_i/S\right)}{\left(S_i/S\right)^2} + \frac{u_c^2(W_{Si})}{W_{Si}^2} \right)^{1/2} \quad (3)$$

$$u_c^2(N_{i,Si}) = \frac{\left(\sigma_{i,Si}^{AXIL} \times \chi^2_{i,Si}\right)^2}{N_{i,Si}^2} \quad (4)$$

$$u_c^2\left(S_i/S_{Si}\right) = \left(S_i/S_{Si}\right)^2 \mathrm{var}(y_q) \quad (5)$$

where s and c^2 are the peak area error and goodness of fitting as provided by the AXIL software and $var(y_q)$ is the variance of the calibration line (1) for element *i*.

Interpretation of the results of the analyses

The collected data consisted of the concentrations of copper and zinc in three consecutive measurements. As an initial exploration, the possible correlation with some clinical parameters was inspected (figures 3 and 4).

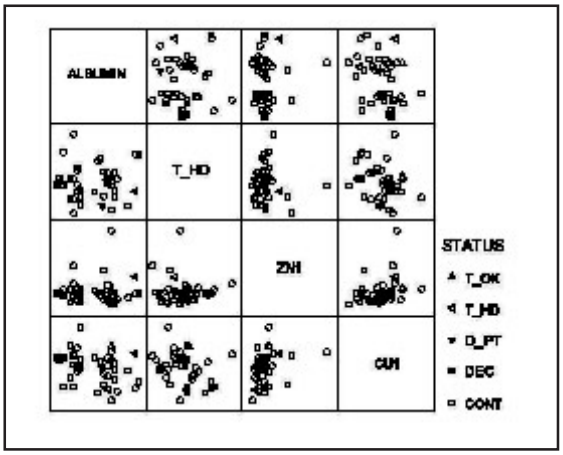

Figure 3. Correlation between values at the start of the study and further evolution of the patients.
Legend: T_OK – Stable condition after kidney transplantation; T_HD – Return to hemodialysis after kidney transplantation; D_PT – Decease after kidney transplantation; DEC – Decease; CONT – Continuing on hemodialysis.

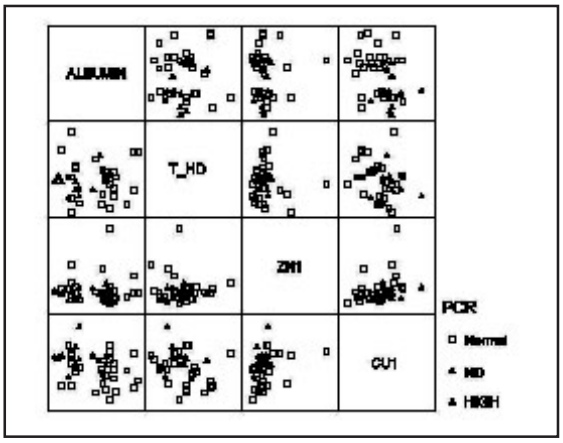

Figure 4. Correlation between values at the start of the study and results of the C-Reactive protein.

No evident correlation was found with albumin values neither for zinc or copper concentrations. However, all of the cases of decease during the term of the study presented lower values of albumin and higher concentrations of copper. The evolution of the patients and the respective tendencies in the concentrations of zinc and copper is more clearly shown in figure 5.

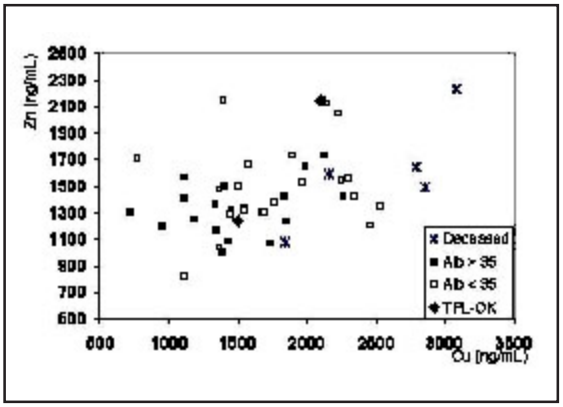

Figure 5. Evolution of the patients.

Another figure of interest was the concurrence of high values of the C-reactive protein with large values of copper concentration. Four of the five cases of decease revealed anomalous values of the C-reactive protein as well (PCR in figure 4). C-reactive protein has been considered as an index of chronic inflammatory condition in the international practice, and it is therefore expected to be associated to cardiovascular caused mortality.

The increase of copper concentration with the time on hemodialysis practice reported in [26] was not observed in our study. The smaller amount of analyzed cases, as well as the relative larger spread in our results might be contributing to such disagreement. However, the concentration of zinc seems to decrease with the age, while the concentration of copper tends to slightly increase (figure 6).

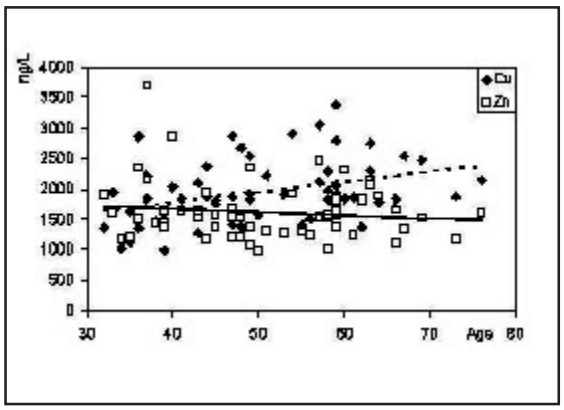

Figure 6. Tendencies in Copper and Zinc concentration changes with age.

The albumin values of several patients changed during the study. The increase on albumin seems to be correlated with the increase of zinc and the decrease of copper concentrations (see figure 7). It can be assumed that the increase in zinc concentration expresses an improvement in the nutritional status of the patients, and probably inhibits the increase in copper concentration.

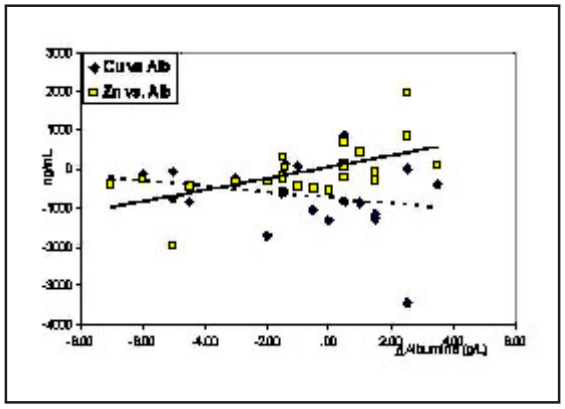

Figure 7. Correlation between albumin changes and metal concentrations.

The whole data set was re-arranged into four categories to explore the feasibility of using their respective median values of copper and zinc as differentiating markers. Group 1 corresponds to patients with albumin values higher than 35 g/L and group 2 to patients with values less than 35 g/L. Group 3 comprises the cases of decease after kidney transplant and group 4 includes the cases of decease while still on hemodialysis.

The mean ranks of each group are shown in table 5. For all of the cases corresponding to decease the values of albumin are the lowest, while copper concentrations are the highest. The patients that did not survive the transplant have the lowest levels of zinc. The results of the Kruskal-Wallis test revealed as the most significant differentiating variables the albumin and copper levels.

Table 5. Mean ranks for each category

	GR ST	N	Mean Rank
Albumin	1.00	25	37.60
	2.00	19	16.00
	3.00	1	1.00
	4.00	5	6.00
	Total	50	
Cu	1.00	25	22.60
	2.00	20	24.90
	3.00	1	47.00
	4.00	5	43.20
	Total	51	
Zn	1.00	25	25.16
	2.00	20	26.85
	3.00	1	5.00
	4.00	5	37.00
	Total	51	

Kruskal-Wallis test

	Albumin	Cu	Zn
Chi-Square	37.274	10.106	2.706
df	3	3	3
Asymp. Sig.	000	018	439

CONCLUSIONS

The average concentration levels of copper and zinc found in this study are slightly larger than the values reported elsewhere. Such differences might be conditioned both by dietary causes and by differences in the type of hemodialysis products.

The lowest concentrations of zinc were found in the cases of worst nutritional condition, reflecting the importance of this element for nutrition. A direct indication is the correlation found with the changes in time on albumin concentration.
The mortality was found correlated with the higher values of copper, in particular with values exceeding 2500 mg/L.

REFERENCES

[1] AIGINGER, H., WOBRAUSCHEK, P., A method for Quantitative X-ray fluorescence analysis in the Nanogram Region. Nucl. Instr. and Meth., 114(1974)457.
[2] WOBRAUSCHEK, P., AIGINGER, H., Total reflection X-ray fluorescence spectrometric determination of elements in nanogram amounts. Anal. Chem., 47(1975)852.
[3] KNOTH, J., SCHWENKE, H., A new totally reflecting X-ray fluorescence spectrometer with detection limits 10-11 g, Fresenius Z. Ana. Chem., 301(1980)7.
[4] MICHAELIS, W., KNOTH, J., PRANGE, A., SCHWENKE, H, Adv. X-Ray Anal. 28, 1985.
[5] AIGINGER, H., WOUBRASCHEK, P., Adv. X-Ray Anal. 28, 1, 1985.
[6] SCHUSTER, M., Spectrochim. Acta. 46B(1991)1341.
[7] GREAVES, ED, MEITIN J., LIENDO, J., CASTELLI, C., SAJO-BOHUS L., .BORBERG, C., Adv. in X-Ray Chem. Anal.. 26s(1995)47.
[8] GREAVES, E.D. BERNASCONI, G. WOBRAUSCHEK, P. STRELI, C., Direct TXRF trace analysis of organic matrix materials with semiempirical standards. Spectrochim. Acta,1997.
[9] PADILLA, R., CHINEA, E., ESTÉVEZ, J.R., GREAVES, E.D., Instrumental detection limits in TXRF: Comparison of Cut-Off and monochromatic excitation Devices, Radioan and Nucl, Chem., Vol. 240, No.2(1999)517-522.
[10] WOBRAUSCHEK, P., Use of total reflection X-ray fluorescence analysis in the life sciences, Biol Trace Elem Res 1994 Fall, 43-45:65-71.
[11] FALEIRO, C., GODINHO, I., REUS, U., DE SOUSA, M., Cobalt-chromium-molybdenum but not titanium-6aluminium-4vanadium alloy discs inhibit human T cell activation in vitro. Biometals, Oct.9(4) (1996)321-326.
[12] PELLA, P.A., Dobbyn RC. Total reflection energy-dispersive X-ray fluorescence spectrometry using monochromatic synchrotron radiation: application to selenium in blood serum. Anal Chem, Apr. 1;60(7) (1988)684-687.
[13] DOGAN, P., DOGAN, M., KLOCKENKAMPER, R., Determination of trace elements in blood serum of patients with Behcet disease by total reflection X-ray fluorescence analysis Clin Chem Jun 39(6) (1993)1037-1041.
[14] MANSOOR, MA, BERGMARK, C., HASWELL, S.J., SAVAGE, I.F., EVANS, P.H., BERGE, R.K., SVARDAL, A.M., KRISTENSEN, O., Correlation between plasma total homocysteine and copper in patients with peripheral vascular disease, Clin Chem, Mar. 46(3) (2000)385-391.
[15] NIEMANN, A., von BOHLEN, A., KLOCKENKAMPER, R, KECK, E., Quantification of biomineralization: an in-vitro tissue culture system and microanalysis of calcium, phosphorus and trace elements by total-reflection X-ray fluorescence, Biochem Biophys Res Commun Aug 16;170(3) (1990)1216-1222.
[16] MAJEWSKA, U., BRAZIEWICZ, J., BANAS, D., KUBALA-KUKUS A., GOZDZ, S., PAJEK, M., SMOK J., URBANIAK, A., An elemental correlation study in cancerous breast tissue by total reflection X-ray fluorescence, Biol Trace Elem Res, Oct-Nov;60(1-2) (1997)91-100.
[17] ZECCA, L, SHIMA, T., STROPPOLO, A., GOJ, C., BATTISTON, G.A., GERBASI, R., SARNA, T., SWARTZ, H.M., Interaction of neuromelanin and iron in substantia nigra and other areas of human brain. Neuroscience, Jul,73(2) (1996)407-415.
[18] von BOHLEN, A., KLOCKENKAMPER, R., OTTO, H., TOLG, G., WIECKEN, B., Qualitative survey analysis of thin layers of tissue samples, Heavy metal traces in human lung tissue. Int Arch Occup Environ Health 59(4) (1987)403-411.
[19] ZECCA, L., SWARTZ, H.M., Total and paramagnetic metals in human substantia nigra and its neuromelanin, J Neural Transm Park Dis Dement Sect,5(3) (1993)203-213.
[20] GUNTHER, K., VON BOHLEN, A., Simultaneous multielement determination in vegetable foodstuffs and their respective cell fractions by total-reflection X-ray fluorescence (TXRF), Z Lebensm Unters Forsch, Apr;190(4) (1990)331-335.
[21] von BOHLEN, A., RECHMANN, P., TOURMANN, J.L., KLOCKENKAMPER, R., Ultramicroanalysis of dental plaque films by total reflection X-ray fluorescence, J Trace Elem Electrolytes Health Dis, Mar,8(1) (1994)37-42.
[22] WITT, H., WITTERSHAGEN, A., BILL, E., KOLBESEN, B.O., LUDWIG, B., Asp-193 and Glu-218 of subunit II are involved in the Mn2+-binding of Paracoccus denitrificans cytochrome c oxidase, FEBS Lett Jun 9;409(2) (1997)128-130.
[23] GONZÁLEZ, V.M., AMO-OCHOA, P., PÉREZ, J.M., FUERTES, M.A., MASAGUER, J.R., NAVARRO-RANNINGER, C., ALONSO, C., Synthesis, characterization, and DNA modification induced by a novel Pt-berenil compound with cytotoxic activity, J Inorg Biochem Jul;63(1) (1996) 57-68.
[24] ZICKERMANN, V., WITTERSHAGEN, A., KOLBESEN, B.O., LUDWIG, B., Transformation of the CuA redox site in cytochrome c oxidase into a mononuclear copper center, Biochemistry Mar 18;36(11) (1997)3232-3236.
[25] JEN-WEN, HUANG., M.D., KUAN-YU HUNG, M.D., SU-HUI LEE, M.D., et al., Trace elements in blood and dyalisate among continuous ambulatory peritoneal dialysis patients: A prospective, multicenter collaborative study. Dialysis and Transplantation, Vol. 29, No. 2, February (2000) 62-67.
[26] HUNG,K. Y. HO,C. Y. KUO Y. M., LEE S. H., HSEIH S. J., et al., Trace elements burden in geriatric hemodialysis patients: A prospective, multicenter collaborative study, The International Journal of Artificial Organs, Vol. 20, No. 10(1997)53-556.
[27] PADILLA, R., MONTERO, A, Informe de Validación. Suero Sanguíneo. Determinación de Ca, Fe, Cu y Zn por Fluorescencia de Rayos X por Reflexión Total, Laboratorio Químico, CEADEN, 2002.

Received: December 16, 2003
Accepted: February 4, 2004

BREAK-UP VS. COMPLETE FUSION FOR WEAKLY BOUND NUCLEI

Paulo Roberto Silveira Gomes[1], Jesus Lubian Rios[1], Roberto Meigikos dos Anjos[1], Ivan Padrón Díaz[2], Guillermo V. Martí[3], Antonio Jorge Pacheco[3], Oscar A. Capurro[3], Jorge O. Fernández Niello[3], Jorge E. Testoni[3], Andrés Arazi[3], Daniel Abriola[3], Marcelo Ramírez[3], Matías D. Rodríguez[4]

[1]Instituto de Física, Universidade Federal Fluminense, Av. Litoranea s/n, Gragoatá, Niterói, R.J., 24210-340, Brazil
[2]Centro de Aplicaciones Tecnológicas y Desarrollo Nuclear (CEDEAN), calle 30 No. 502 e/ 5ta Ave. 7ma, Playa, Ciudad de La Habana, Cuba
[3]Laboratorio Tandar, Departamento de Física, Comisión Nacional de Energía Atómica, Av. del Libertador 8250, Buenos Aires, 1429, Argentina
[4]Departamento de Física, Facultad de Ciencias Exactas y Naturales, Universidad de Buenos Aires, Buenos Aires, Argentina
ipadrondiaz@yahoo.com.ar

RUPTURA VS. FUSIÓN TOTAL PARA NÚCLEOS DE ENLACES DÉBILES

Resumen

Se midieron las secciones eficaces de fusión para los sistemas ^{6,7}Li + ^{27}Al, ^{64}Zn, a energías superiores a la barrera de Coulomb con el objeto de estudiar la influencia de la ruptura de núcleos estables débilmente enlazados en el proceso de fusión. El análisis se completó con la inclusión de los datos de fusión inducida por ^{9}Be y los proyectiles firmemente enlazados en los mismos blancos, y con la fusión de estos proyectiles débilmente enlazados en los blancos pesados. Las funciones de excitación de fusión para los blancos pesados se suprimen, al compararlas con las predicciones de modelos de penetración de barrera simple y cálculos de canales acoplados que no tienen en cuenta el proceso de ruptura. Sin embargo, para los blancos medianamente ligeros no hay ninguna marca de obstrucción de fusión.

Abstract

Fusion cross sections were measured for the ^{6,7}Li + ^{27}Al, ^{64}Zn systems, at energies above the Coulomb barrier, in order to study the influence of the break-up of stable weakly bound nuclei on the fusion process. The analysis was completed by the inclusion of the data of fusion induced by ^{9}Be and tightly bound projectiles on the same targets, and fusion of the same weakly bound projectiles on heavy targets. The fusion excitation functions for the heavy targets are suppressed, when compared with predictions of single barrier penetration models and coupled channel calculations that do not take into account the break-up process. However, for the medium-light targets there is no signature of fusion hindrance.

Key word: beryllium 9 reactions, breakup reactions, cross sections, elastic scattering, incomplete fusion reactions, lithium 6 reactions, lithium 7 reactions, sinc 64 target

INTRODUCTION

The effect of the break-up process on the fusion cross section has been investigated in the last years, and in the present it is still far from being full understood. There is a special interest on this subject due to the recently available radioactive beams of very weakly bound nuclei. Due to the low intensities of the radioactive beams, it is very convenient to produce fusion reactions with the high intensity stable beams that are weakly bound, and consequently should have a significant break-up probability.

Theoretically there are models that predict the fusion cross section enhancement, when compared with the fusion induced by strongly bound nuclei, due to the presence of low lying weakly-bound or unbound states, particularly important at sub-barrier energies, where the coupling effects on the fusion may be strong. On the other hand, some models suggest the hindrance of the complete fusion, due to the loss of incident flux in this channel, caused by the break-up. There are also predictions of fusion cross section enhancement at sub-barrier energies and fusion hindrance at above barrier energies.

If one wants to have a comprehensive view of this problem, one has to study different energy regimes, from the sub-barrier to well above barrier energies and also one has to span different nuclear masses, in order to investigate the effect, on the fusion, of nuclear and Coulomb break-ups. The suitable nuclei for this kind of study are ^{9}Be, ^{6}Li and ^{7}Li, that have small separation energies: ^{6}Li breaks-up into ^{4}He + ^{2}H, with

separation energy Sα = 1.48 MeV; ^{7}Li into ^{4}He + ^{3}H, with Sα= 2.45 MeV and ^{9}Be into ^{8}Be+n® n+^{4}He+ ^{4}He, with S_n = 1.67 MeV or into ^{5}He + ^{4}He, with Sα= 2.55 MeV. The comparison between the fusion cross sections induced by them and by tightly bound nuclei on the same targets is important for the understanding of the effect of the break-up on the fusion process.

In such studies, different reaction mechanisms should be considered: elastic break-up (BU) corresponding to either large or low partial waves; inelastic break-up, particularly incomplete fusion (ICF) and complete fusion (CFBU) of the break-up fragments. In order to contribute to this field, we have measured the fusion cross sections for the ^{6,7}Li + ^{27}Al, ^{64}Zn systems, at energies above the Coulomb barrier [1]. The group at UFF have measured the fusion of ^{9}Be with the same targets [2,3] and the fusion with heavy targets [4,5]. In this paper we try to give an overall view of the field, based on those results.

THE EXPERIMENTAL SET-UP AND MEASUREMENTS

The experiments were performed at the 20-UD tandem accelerator of the TANDAR Laboratory, at Buenos Aires. Beams of ^{6,7}Li were produced by a SNICS type ion source, from cathodes consisting of a mixture of 70% lithium isotopes, with 30% silver powder. The beam energies at the laboratory system ranged from 24.0 to 43.0 MeV, well above the nominal Coulomb barriers ($V_{B\ Lab}$ ≈15 MeV and ≈10 MeV for ^{64}Zn and ^{27} Al targets, respectively). The incident beam was collimated, at the entrance of the scattering chamber, by a 2 mm lead collimator. The ^{27}Al target was self supported, with thickness of 46 mg/cm^2. The metallic ^{64}Zn target, with thickness of 50 mg/cm^2, was deposited on a 10 mg/cm^2 carbon backing. The detector system was a time of flight (TOF) heavy ion system, specially designed and built for these experiments, and described in details in another paper from this conference [6].

The masses of the residual nuclei originated from the complete fusion (CF) and those from the incomplete fusion (ICF) are mostly the same, and therefore we were not able to separate CF from ICF. So, the measured fusion cross sections correspond to the sum of these two processes.

THE FUSION CROSS SECTIONS

Differential fusion cross sections were measured for q_{Lab} = 10°, 12°, 150° and 20°, for the ^{6,7}Li + ^{27}Al and for q_{Lab} = 10°, 12°, 15°, 20° and 30° for the ^{6,7}Li + ^{64}Zn reactions. The maxima of the angular distributions are located at θ_{Lab} ≈10° to 15°, and the measured angular ranges cover around 60% of the complete angular distributions, according to the shape of the theoretical predictions obtained by the statistical code PACE [7]. The extrapolation to the most forward and backward parts of the angular distributions were performed using the code PACE. The precision of this method allows the evaluation of the complete angular distributions with accuracy of the order of 5%.

The efficiency of the MCP start detector was calculated for each spectrum, as the ratio between the number of coincidence events with the MCP detector recorded by the PIPS detector, and the number of counts in the single spectrum recorded by this stop detector. Its value is within the range 0.13-0.20 obtained for the ^{7}Li + ^{64}Zn reactions, and 0.28-0.38 obtained for the ^{7}Li + ^{27}Al reactions. The associated uncertainties in these values are in the range 2-4%.

The normalization of the fusion cross sections were obtained by counting the elastic scattering events in the spectra, when the experimental conditions were such that the scattering was purely Rutherford. Otherwise, it was obtained using the integrated beam current in the Faraday cup. From the comparison of the normalization factors obtained when both methods could be applied imultaneously, it was proved that the normalization method using the Faraday cup was quite reliable. When the first method was used, the associated uncertainty was around 2%, otherwise it was the sum of three contributions: around 2% from the beam intensity, 5% from the target thickness and 1% from the solid angle detection system determination.

The overall error bar for the total fusion cross sections was found to be of the order of 6-8% for the ^{6,7}Li + ^{64}Zn systems, and 7-10% for the ^{6,7}Li + ^{27}Al systems (see table 1).

Table 1. Total fusion cross sections measured in this work

E_{Lab} (MeV)	^{6}Li + ^{27}Al σ_{fus}(mb)	^{7}Li + ^{27}Al σ_{fus}(mb)	^{6}Li + ^{64}Zn σ_{fus}(mb)	^{7}Li + ^{64}Zn σ_{fus}(mb)
24	1090 ± 93	1050 ± 94	597 ± 45	656 ± 56
28	1014 ± 93	1116 ± 94	823 ± 59	883 ± 66
31	1173 ± 100	1238 ± 99	869 ± 60	922 ± 64
34	1152 ± 90	1210 ± 95	984 ± 68	1002 ± 69
37	1162 ± 86	1237 ± 91	1053 ± 71	1134 ± 77
40	1148 ± 78	1238 ± 84	1022 ± 65	1105 ± 75
43	1170 ± 77	1252 ± 83	1166 ± 71	1254 ± 81

DISCUSSION OF THE RESULTS

Before the discussion of our results, we will comment the main results from the measurements, performed by the UFF group and collaborators, for the fusion of heavy targets, within the general overview that we propose to give. Complete fusion cross sections were measured for the ^{6,7}Li + ^{209}Bi [5] and ^{9}Be + ^{208}Pb [4] systems. For all of them, single barrier penetration calculations (SBPC) and coupled channel calculations (CCC), without the inclusion of any projectile break-up effect, predict larger values than the experimental ones at above barrier energies. Agreement between the measured and calculated CF cross sections at high energies can only be obtained if the calculated cross sections are scaled by factors equal to 0.66 for ^{6}Li, 0.74 for ^{7}Li and 0.68 for ^{9}Be.

It is interesting to notice that although the suppression of the CF cross sections at high energies was found to be similar for the different systems, the strongest CF suppression occurs for the ^{6}Li projectile, that has the smallest break-up separation energy, and the smallest occurs for the ^{7}Li, for which this value is the highest among the three projectiles. Therefore, the data at high energies show that the break-up process inhibits the CF cross section at this energy regime, and there is a signature that the suppression factor increases as the break-up separation energy decreases, although the differences in the fusion cross sections are not so remarkable as the differences in the break-up threshold energy and in the elastic break-up cross sections of similar systems might suggest.

These cross sections were found to be large and much higher than the fusion cross sections at sub-barrier energies, and there is a very strong dependence of the elastic break-up cross section with the break-up threshold energy. The reaction cross sections derived for some of these systems also increase strongly when the projectile break-up threshold energy decreases. However, the large difference between the break-up cross sections for different weakly bound projectiles are not reflected in the fusion cross section (see table 2).

The question now is the following: Is it possible to extend the conclusions for heavy targets to medium–light mass ($19 \leq A \leq 64$) target nuclei? In order to answer this question we have performed similar analysis for our data and we have also compared the fusion excitation functions of several systems: the weakly bound ^{6,7}Li and ^{9}Be, and the tightly bound ^{16,17,18}O, ^{14}N, ^{12}C and ^{10,11}B nuclei as projectiles and the ^{19}F, ^{27}Al, ^{29}Si and ^{64}Zn nuclei as targets. Only the CF + ICF cross sections were determined for all the systems, except for the ^{9}Be + ^{64}Zn, for which the CF cross sections were measured and the ICF cross section was found to be negligible [3]. We suppose that the ICF is also not important for similar systems, as opposed to the behavior when systems with heavy targets are used. Each fusion excitation function was fitted by SBPC. This is justified in the energy region above the Coulomb barrier, where inelastic and transfer channels couplings do not affect the fusion cross section significantly. If the break-up process had an important influence on the fusion cross section, the derived barrier parameters should have anomalous values. However, reasonable fits were obtained for all the systems, and the barrier parameters agree with the values from systematic, within the usual fluctuations around the average values.

Figure 1 shows the reduced fusion excitation functions for the ^{6,7}Li, ^{9}Be, ^{16}O + ^{64}Zn systems. The fusion excitation functions for these systems are very similar, regardless of the presence or absence of weakly bound nuclei. The same behavior is found when we compare the excitation functions of the ^{6,7}Li, ^{9}Be, ^{11}B, ^{16}O +^{27}Al systems, as shown in figure 2; ^{9}Be +^{27}Al, ^{29}Si and ^{11}B +^{27}Al systems (the last one leads to the same compound nucleus as ^{9}Be +^{29}Si); ^{18}O+^{10}B, ^{17}O + ^{11}B, ^{19}F + ^{9}Be - all the three leading to the same compound nucleus; ^{19}F + ^{9}Be and ^{19}F + ^{12}C. Therefore, the fusion excitation functions, which we expect to correspond to CF, for the medium-light systems do not seem to be influenced by the break-up process and do not show any dependence on the projectile separation energy, within the ~ 10% uncertainties of the measurements.

Table 2. Barrier Parameters obtained by the fitting of the fusion excitation functions, using the Wong model, and the barrier parameters obtained from the systematic

System	$V_{B\ c.m.}$ (MeV)	$r_{o\,exp}$ (fm) / [$r_{o\,syst}$ (fm)]	R_B (fm)	$r_{o\,exp}$ (fm) / [$r_{o\,syst}$ (fm)]
^{6}Li +^{27}Al	7.55	1.55 / [1.82]	7.21	1.54 / [1.66]
^{7}Li + ^{27}Al	7.38	1.55 / [1.82]	7.36	1.56 / [1.66]
^{9}Be +^{27}Al	8.81	1.67 / [1.79]	7.29	1.44 / [1.63]
^{11}B + ^{27}Al	11.2	1.60 / [1.76]	7.69	1.47 / [1.61]
^{16}O + ^{27}Al	16.1	1.69 / [1.70]	7.05	1.44 / [1.56]
^{6}Li +^{64}Zn	14.0	1.61 / [1.72]	7.46	1.28 / [1.57]
^{7}Li + ^{64}Zn	13.8	1.59 / [1.72]	7.71	1.30 / [1.57]
^{9}Be + ^{64}Zn	16.2	1.76 / [1.68]	10.0	1.65 / [1.54]
^{16}O + ^{64}Zn	32.5	1.63 / [1.59]	10.0	1.53 / [1.47]

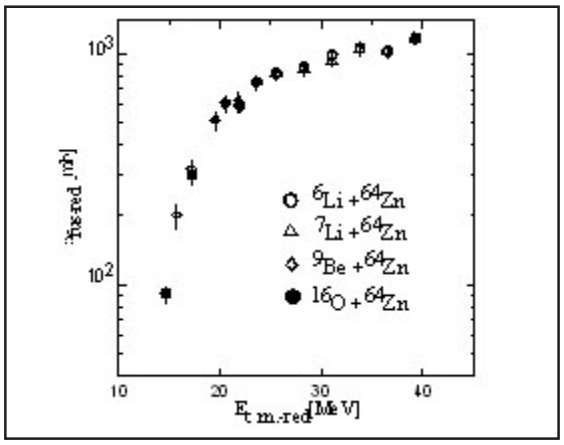

Figure 1. Reduced fusion excitation functions of different projectiles on the ^{64}Zn target.

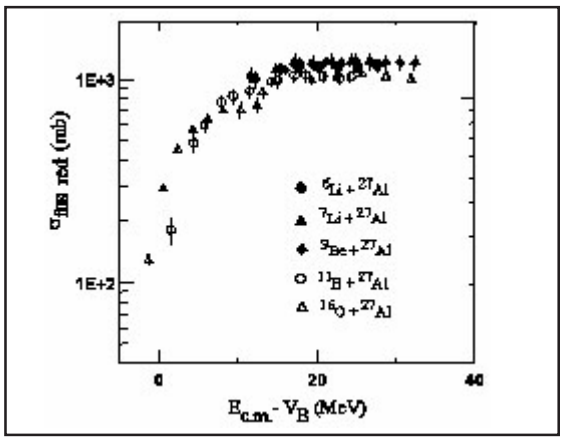

Figure 2. Reduced fusion excitation functions of different projectiles on the ^{27}Al target.

Although more sophisticated quantum mechanical calculations, including continuum discretized coupled channels and nuclear structure effects, are required to understand the correlation between break-up, fusion and scattering mechanisms involving stable weakly bound nuclei, we believe that a simple picture of the process can be given at the moment, based on the experimental results presented in this paper, for energies above the Coulomb barrier. The BU corresponding to large partial waves is related to the measured elastic break-up cross sections, and does not affect the CF cross section, since these mechanisms are concerned with different partial waves. The fusion cross section should be affected by processes and interactions that take place near the nuclear surface of the colliding nuclei, where the fusion is decided. The results show that the sum of ICF + CF cross sections correspond to the predictions of CCC and SBPC, without the inclusion of the BU process, for the whole mass range of the target.

Therefore, the BU process that occurs near the Coulomb barrier radius leads predominantly to the absorption, by the target nucleus, of one or all the fragments. The probability that only one of the fragments fuses with a heavy target, leading to ICF, is likely to occur at any energy above the barrier. This is the mechanism responsible for the CF suppression at energies above the barrier, corresponding to a significant fraction of the total fusion cross section (of the order of 30%). For medium-light mass targets, however, the ICF is negligible, at least within the experimental error bars of the measured fusion cross sections (of the order of 10%). The conclusions related to the negligible ICF cross section for light targets may not be a priori extended to halo nucleus projectiles, due to their abnormal large radii.

ACKNOWLEDGEMENTS

The authors wish to thank the Fundação Vitae and Fundación Antorchas for their financial support that allowed the collaboration Brazil-Argentina. The Brazilian and Cuban authors also would like to thank the CNPq for their partial financial support. Some of us (A J. P., J. O F.N, J.E.T) are fellows of the Carrera del Investigador Científico of the CONICET.

REFERENCES

[1] PADRÓN, I., GOMES, P.R.S., ANJOS, R.M., LUBIAN, J., et al, Fusion of stable weakly bound nuclei with ^{27}Al and ^{64}Zn Physical Review C 66 (2002)044608.
[2] ANJOS, R.M., MURI, C., LUBIAN, J., GOMES, P. R. S, PADRÓN, I., et al, No evidence of break-up effects on the fusion of ^{9}Be with medium-light nuclei, Physics Letters B 534, 45(2002).
[3] MORAES, S.B., GOMES, P.R.S., LUBIAN, J., ALVES, J.J., et al Fusion and elastic scattering of ^{9}Be + ^{64}Zn: A search of the breakup influence on these processes; Physical Review C 61, 064608 (2000).
[4] DASGUPTA, M., HINDE, D.J., BUTT, R.D. ANJOS, et al, Fusion versus break-up: Observation of large fusion suppression for ^{9}Be + ^{208}Pb"; Physical Review Letters 82, (1999)1395.
[5] DASGUPTA, M., HINDE, D.J., HAGINO, K. MORAES, S. B., et al, Fusion and breakup in the reactions of ^{6}Li and ^{7}Li nuclei with ^{209}Bi; Physical Review C 66 (2002)041602R.
[6] PADRÓN, I., MARTÍ, G.V, RAMÍREZ, M., PACHECO, A J., et al., Fusion cross section measurements for the ^{6,7}Li + ^{27}Al, ^{64}Zn systems, by the time of flight technique, Proceedings of this conference 2003.
[7]GAVRON, A., Physical Review C 21, 230(1980).

Received: December 16, 2003
Accepted: February 4, 2004

FUSION CROSS SECTION MEASUREMENTS FOR ^{6,7}Li + ^{27}Al, ^{64}Zn SYSTEMS BY THE TIME-OF-FLIGHT TECHNIQUE

Ivan Padrón Díaz[1], Paulo Roberto Silveira Gomes[2], Jesus Lubian Rios[2], Roberto Meigikos dos Anjos[2]
Guillermo V. Martí[3], Antonio Jorge Pacheco[3], Oscar A. Capurro[3],
Jorge O. Fernández Niello[3], Jorge E. Testoni[3], Andrés Arazi[3], Daniel Abriola[3], Marcelo Ramírez[3],
Matías D. Rodríguez[4]

[1]Centro de Aplicaciones Tecnológicas y Desarrollo Nuclear (CEADEN), calle 30 No. 502 e/ 5ta Ave. y 7ma., Playa, Ciudad de La Habana, Cuba
[2]Instituto de Física, Universidade Federal Fluminense, Av. Litoranea s/n, Gragoatá, Niterói, R.J., 24210-340, Brazil
[3]Laboratorio Tandar, Departamento de Física, Comisión Nacional de Energía Atómica, Av. del Libertador 8250, Buenos Aires, 1429, Argentina
[4]Departamento de Física, Facultad de Ciencias Exactas y Naturales, Universidad de Buenos Aires, Buenos Aires, Argentina
ipadrondiaz@yahoo.com.ar

MEDICIÓN DE LA SECCIÓN EFICAZ DE FUSIÓN PARA LOS SISTEMAS ^{6,7}Li + ^{27}Al, ^{64}Zn POR LA TÉCNICA DE TIEMPO DE VUELO

Resumen

Para estudiar el papel de la desintegración nuclear y coulombiana en la fusión atravesando diferentes masas del núcleo blanco, se desarrolló un Espectrómetro de Ión Pesado de Tiempo de Vuelo. En esta contribución se presentaron las secciones eficaces de fusión para los sistemas ^{6,7}Li + ^{27}Al y ^{6,7}Li+^{64}Zn medidas al bombardear con energías cercanas y superiores a la barrera coulombiana. Los experimentos se realizaron en Acelerador Tándem 20 UD del Laboratorio Tandar, CNEA, Buenos Aires. El equipo de detección incluye un MCP y un BSD (las pipas) como detectores de "comienzo" y "parada," respectivamente, con una distancia de vuelo de 1.70 m. Algunas mejoras para perfeccionar la resolución de tiempo, que se llevan a cabo en este momento, también serán reportadas en este trabajo. Recientemente se han estudiado las secciones eficaces de fusión de las energías sobre la barrera de Coulomb para los sistemas ^{6}Li +^{27}Al y ^{6}Li +^{64}Zn. El trabajo presenta los resultados preliminares (julio de 2003) de la continuación natural de las medidas anteriores, es decir las secciones eficaces de fusión para energías por debajo de la barrera para dichos sistemas.

Abstract

In order to study the role of the nuclear and Coulomb break-up on the fusion by spanning different target nucleus masses, a Time-of-Flight Heavy Ion Spectrometer was developed. In this contribution we present the fusion cross sections for the systems ^{6,7}Li + ^{27}Al and ^{6,7}Li+^{64}Zn measured at bombarding energies near and above the Coulomb barriers. The experiments were performed at the 20 UD Tandem Accelerator of the Tandar Laboratory, CNEA, Buenos Aires. The detection assembly includes a MCP and a BSD (PIPS) as "start" and "stop" detectors, respectively, with a 1.70 m flight distance. Some improvements for optimizing the time resolution, being carried out at this moment, will also be reported in this work. Recently we have studied fusion cross sections at energies above the Coulomb barrier for the ^{6}Li +^{27}Al and ^{6}Li +^{64}Zn systems. In the present work the preliminary results (July 2003) of the natural continuation of the previous measurements, i.e. fusion cross-sections at sub-barrier energies for the same systems, are presented.

Key words: beryllium 9 reactions, breakup reactions, cross sections, elastic scattering, lithium 6 reactions, lithium 7 reactions, zinc 64 target, aluminium 27 reactions

INTRODUCTION

The influence of the break-up of stable and radioactive nuclei on the fusion process at energies above and below the Coulomb barrier, has taken great interest in the last years. Recently we have studied fusion cross sections at energies above the Coulomb barrier for the ^{6}Li +^{27}Al and ^{6}Li +^{64}Zn systems [1]. In the present work the preliminary results (July/2003) of the natural continuation of the previous measurements, i.e. fusion cross-sections at sub-barrier energies for the same systems are presented.

The role of the break-up process of weakly bound nuclei on the fusion mechanism, at near and sub-barrier energies, is not yet quite understood. This subject is nowadays particularly interesting, because radioactive beams with halo nuclei become available. The study of reactions induced by stable weakly bound nuclei, such as ^{6,7}Li and ^{9}Be, may also contribute significantly to the understanding of the processes. The break-up of the valence nucleons in the entrance channel may remove flux from the complete fusion channel, if just one of the parts of the broken nucleus is captured by the target, and consequently decrease the complete fusion probability [2-5].

In order to study the role of the nuclear and Coulomb break-up on the fusion by spanning different target nucleus masses a Time-of-Flight Heavy Ion Spectrometer was developed. Some improvements for optimizing the time resolution, will also be reported in this work.

EXPERIMENTAL SET-UP AND MEASUREMENTS

The experiments were performed at the 20-UD tandem accelerator of the TANDAR Laboratory, at Buenos Aires. Beams of ^{6,7}Li and ^{9}Be were produced by a SNICS type ion source and accelerated at energies ranging from 14 to 43 MeV, below and around the Coulomb barrier. The ^{27}Al target was self-supported, with thickness of 46 Wg/cm^2. The metallic ^{64}Zn, with a thickness of 50 Wg/cm^2, was deposited on a 10 Wg/cm^2 carbon backing. The detector system was a time of flight (TOF) heavy ion system, specially designed and built for these experiments. A zero-time detector (Micro Channel Plate (MCP) (3 stages Burle MCP) was used as a start detector and a passivated implanted planar silicon (PIPS) detector (Canberra TMPD900-27-300) as the stop detector. The total FWHM resolution for the system was 750 ps for a typical time of flight of 400 ns.

Figure 1 shows, schematically, the experimental setup. The incident beam was collimated, at the entrance of the scattering chamber by a 2 mm lead collimator. Another lead collimator was placed at the entrance of the time of flight tube, in order to shield the micro-channel plates of the start detector from the intense X-rays produced when the beam impinges on the target. The flight distance for reaction products between the start and stop detectors was 173 cm.

The reaction products at different scattering angles were detected taking advantage of a sliding flange between the scattering chamber and the TOF line, allowing angular distribution measurements at a reasonably wide angular range, and with angular uncertainties of 0.5º.

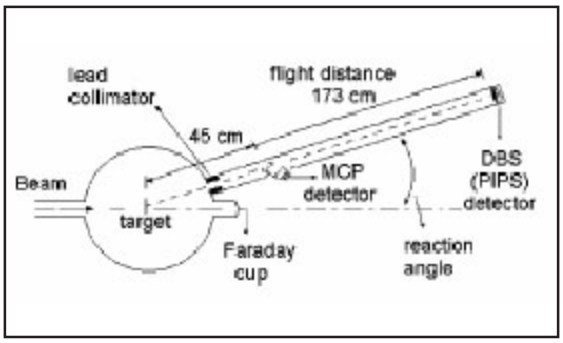

Figure 1. Schematic picture of the experimental set-up of the time of flight device used in the present work.

Figure 2 shows the electronic scheme designed for this experiment. The challenge on our spectrometer was associated with the wide energetic and mass range of reaction products. The detection of heavier fusion products, at energies near to its energy loss limit, was an obstacle for the fast electronic, which should be able to separate the elastic peaks from light ions scattered on ^{64}Zn and the contaminants ^{12}C and ^{16}O.

The acquisition of temporal and energetic spectra by separate and in coincidence was carried out using an AD811 module and the CANDA acquisition code. At the same time the energetic spectrum was collected without coincidences by an ORTEC multi-channel analyser MAESTRO A65 BI.

Figures 3(a) and 3(b) show typical energy vs. TOF spectra, taken for E_{Lab}=43 MeV and θ_{Lab}=10^{o}, for ^{6}Li + ^{64}Zn and ^{27}Al systems, respectively. The enlargement shows that the system was able to separate events differing by one unit of atomic mass and that the fusion reaction products are well separated from the fusion products with ^{12}C backing and ^{16}O contaminants. The electronic cut-off threshold was set close to the minimum values but, even so, the spectra were corrected by the use of the statistical model code PACE [6], in order to take into account the events with energies below that threshold.

The masses of the residual nuclei originating from the complete fusion (CF) and those from the incomplete fusion (ICF) are mostly the same, and the detection assembly was not able to separate CF from ICF. Therefore, the measured fusion cross sections correspond to the sum of these two processes.

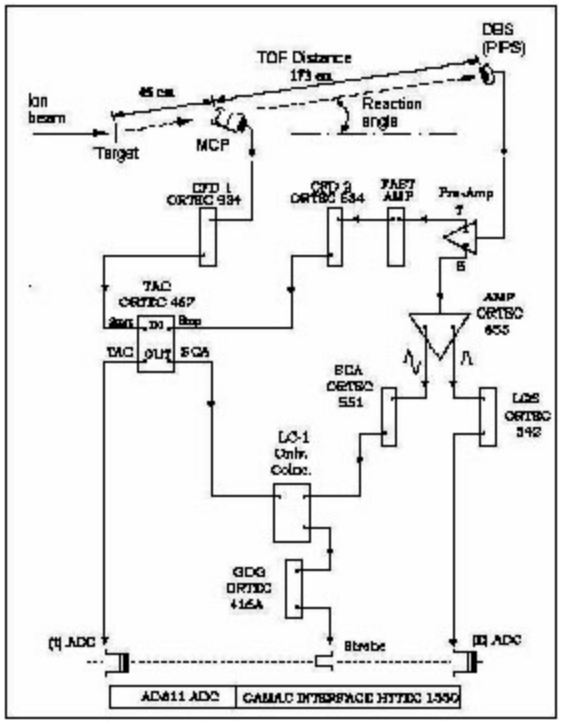

Figure 2. Detection and acquisition data assembly.

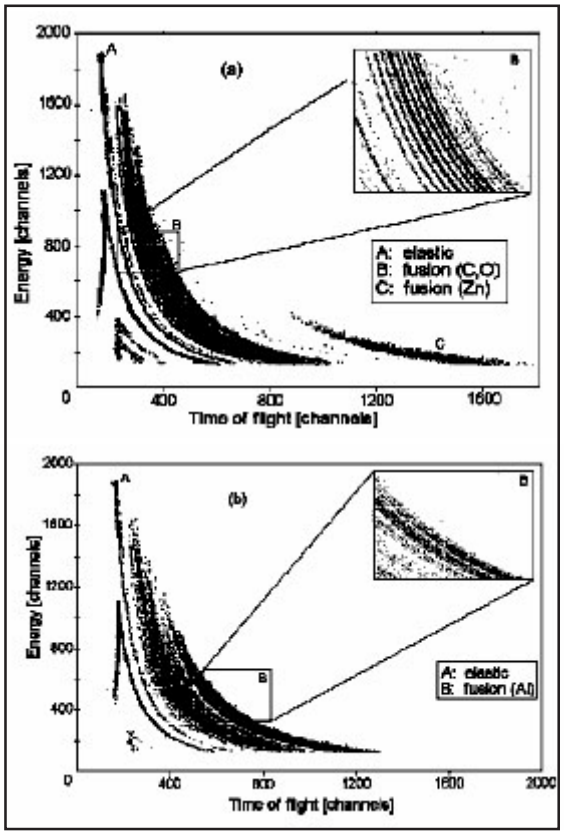

Figure 3. Typical time of flight spectra, for (a) ^{6}Li + ^{64}Zn and (b) ^{6}Li +^{27}Al systems, taken for E_{Lab}= 43 MeV and q_{Lab}= 10º .

EXPERIMENTAL RESULTS

Differential fusion cross sections were measured for angles θ_{Lab} = 10º, 12º, 15º and 20º at energies of 43, 34, 24 and 20 MeV for the ^{6,7}Li+^{64}Zn(C), ^{6,7}Li+^{27}Al(Zn) systems and at 22 MeV for the ^{9}Be+^{27}Al system. The maxima of the angular distributions are located at θ_{Lab} = 10º-12º, and the measured angular ranges cover around 60% of the complete angular distributions, according to the shape of the theoretical predictions obtained by the statistical code PACE. The extrapolation to the most forward and backward parts of the angular distributions was performed using the code PACE.

Figure 4 shows the measured differential fusion cross section for one bombarding energy (43 MeV), for the ^{7}Li+^{64}Zn system, and the prediction of the PACE code represented by the full line. The precision of this method allows the evaluation of the complete angular distributions with an accuracy of the order of 5%.

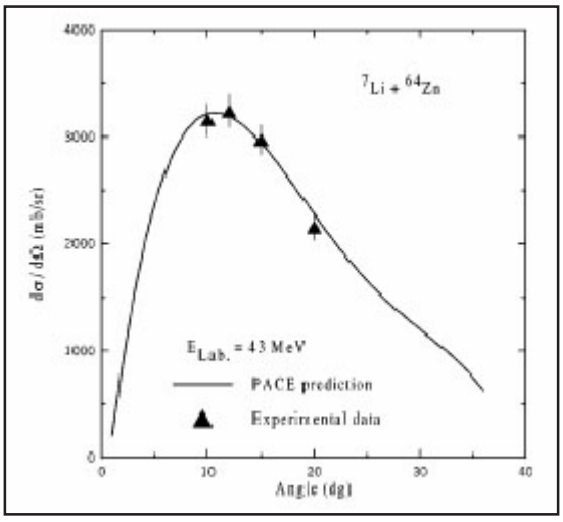

Figure 4. Measured differential fusion cross section for the energy of 43 MeV, for the ^{7}Li+^{64}Zn system, and the prediction of the PACE code, represented by the full line.

The efficiency of the MCP start detector was calculated for each spectrum as the ratio between the number of coincidence events with the MCP recorded by the PIPS detector, and the number of counts in the single spectrum recorded by this stop detector. Its value is within the range 0.13 - 0.20 obtained for the ^{7}Li+^{64}Zn reaction and 0.28 - 0.38 obtained for the ^{7}Li+ ^{7}Al reactions. The associated uncertainties in these values are in the range 2% - 4%.

The normalization of the fusion cross sections was obtained by counting the elastic scattering events in the spectra, when the experimental conditions were such that the scattering was purely Rutherford. Otherwise, it was obtained using the integrated beam current in the Faraday cup. From the comparison of the normalization factors obtained when both methods could be applied simultaneously, it was proved that the

normalization method using the Faraday cup was quite reliable. When the first method was used, the associated uncertainty was around 2%, otherwise it was the sum of three contributions: around 2% from the beam intensity, 5% from the target thickness, and 1% from the solid angle determination.

In the figure 5 the results recently obtained for sub-barrier energies are compared with a previous experimental work. Recent fusion cross section measurements were carried out at energies 14, 16, 18, 20, 22 and 24 MeV, while the previous one were at energies 24, 28, 31, 34, 37, 40 and 43 MeV. The new data seem to follow the same tendency as the fusion cross sections obtained at energies above de Coulomb barrier.

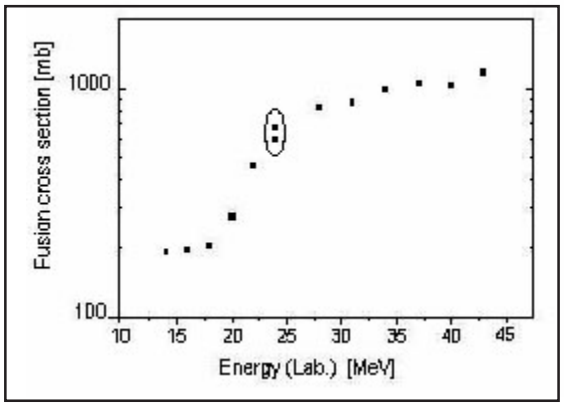

Figure 5. Fusion excitation functions measured for ^{6}Li + ^{64}Zn system. Recent measurements: 14, 16, 18, 20, 22 and 24 MeV; previous work: 24, 28, 31, 34, 37, 40 and 43 MeV.

Finally, as a summary we have designed and built a time of flight heavy ion detector system that is able to measure angular distributions of the evaporation residues of fusion of light projectiles on a wide variety of targets, simultaneously with elastically scattered nuclei. We have measured and analyzed the fusion cross sections at energies below and above the Coulomb barrier, for the ^{6,7}Li+^{64}Zn, ^{6,7}Li+^{27}Al and ^{9}Be+^{27}Al systems. These data complemented by the previously reported data for ^{9}Be on the same targets [2], make an interesting set of available results that allows the comparison of the effect of the break-up of stable weakly bound nuclei on the fusion of medium-light systems.

The new data for the ^{6}Li+^{27}Al and ^{6}Li+^{64}Zn systems seems to follow the same tendency as the previous one down to 18-20 MeV.

At low energies te cross section values are believed to be strongly influenced by the detection efficiency and probably because of the backing of the targets. Those will be further analyzed and at next future both data points will be re-measured with pure ^{27}Al target to test for this presumption. No further conclusions will be given here due to the preliminary character of these previous results.

ACKNOWLEDGEMENTS

The authors wish to thank the Fundação Vitae and Fundación Antorchas for their financial support that allowed the collaboration Brazil-Argentina. The Brazilian and Cuban authors also would like to thank the CNPq for their partial financial support. Some of us (A.J. P., J. O.F.N., J.E.T.) are fellows of the Carrera del Investigador Científico of the CONICET.

REFERENCES

[1] PADRÓN, I., GOMES P.R.S., ANJOS, R.M., LUBIAN, J., et al, Fusion of stable weakly bound nuclei with ^{27}Al and ^{64}Zn; Physical Review C 66(2002)044608.
[2] ANJOS, R.M., MURI,C. LUBIAN, J. GOMES, P. R. S. PADRÓN ,I., et al., No evidence of break-up effects on the fusion of ^{9}Be with medium-light nuclei; Physics Letters B 534, 45(2002).
[3] MORAES, S.B. GOMES, P.R.S. LUBIAN, J. J ALVES, J. S. et al, Fusion and elastic scattering of ^{9}Be + ^{64}Zn: A search of the breakup influence on these processes; Physical Review C 61(2000)064608.
[4] DASGUPTA, M. HINDE, D.J. HAGINO, K. MORAES, S. B. GOMES, P.R.S. , ANJOS, R.M. BUTT, R.D. BERRIMAN, A.C. CARLIN, N. MORTON, C.R. NEWTON, J. TOLEDO, A.S., Fusion and breakup in the reactions of ^{6}Li and ^{7}Li nuclei with ^{209}Bi; Physical Review C 66(2002)041602R.
[5] GOMES, P.R.S., LUBIAN, J., ANJOS, R.M., PADRÓN, I., et al, Breakup v.s. complete fusion for weakly bound nuclei, Proceedings of this conference (2003).
[6] GAVRON, A., Physical Review C 21, 230(1980).

Received: December 16, 2003
Accepted: February 4, 2004

THYROID UPTAKE SOFTWARE

Dolores Alonso Abat[1], Eduardo Arista Romeu[2]
[1]Centro de Protección e Higiene de las Radiaciones (CPHR), Calle 20 No. 4113 e/ 41 y 47, Playa, Ciudad de La Habana, Cuba
[2]Centro de Aplicaciones Tecnológicas y Desarrollo Nuclear (CEADEN), Calle 30 No. 502, e/ 5ta Ave. y 7ma, Playa, Ciudad de La Habana, Cuba
arista@ceaden.edu.cu

SOFTWARE DE CAPTACIÓN TIROIDEA

Resumen

Se desarrolló un software DETECT-PC para un sistema de detección-medición que permite realizar el estudio de captación de yodo en tiroides. El diseño cumple con los principios de la programación orientada a objetos y fue usado el lenguaje C++.
El sistema fija automáticamente los parámetros espectrométricos para la medición y además de la medición de los pacientes, realiza el procesamiento del lote de muestras a utilizar, posee una base de datos PARADOX con toda la información de los pacientes medidos y un sistema de ayuda que se refiere a las opciones del sistema y a los conceptos médicos y nucleares relacionados con el estudio de captación de yodo en tiroides

Abstract

The DETEC–PC software was developed as a complement to a measurement system (hardware) able to perform Iodine thyroid uptake studies. The software was designed according to the principles of object oriented programming using C++ language.
The software automatically fixes spectrometric measurement parameters and besides patient measurement also performs statistical analysis of a batch of samples. It possesses a PARADOX database with all information of measured patients and a help system with the system options and medical concepts related to the thyroid uptake study.

Key words: personal computers, thyroid, computer codes, iodine, uptake, scintillations, nuclear medicine, data acquisition system, programming languages

.

INTRODUCTION

Diseases caused for a malfunction of the thyroid gland are very common. Any general hospital assists dozens of such cases weekly and there are some places where those diseases are endemic. Iodine thyroid uptake is used as diagnostic and therapeutic method in medical practice (nuclear medicine) since the decade of the 50ties. These studies are indicated in all such cases in which it is desired to evaluate the functional state of the thyroid gland as: hyperthyroidism, diffuse toxic goitre, nodular goitre, thyroid's cancer and others, allowing therapeutic results evaluation and ^{131}I treatment planning.
In nuclear medicine, iodine thyroid uptake studies are carried out in order to assess the functional state of the gland by measuring the absorption level of a radiopharmaque and the variations of its concentrations on time.

Iodine thyroid uptake study consists in the oral administration to patient of a radioactive iodine preparation. The radioactive substance is chemically attracted to the gland and produces an emission that can be found by using a detector of ionizing radiations. The Thyroids Iodine concentration degree, as well as its variations on time reflects gland functioning [1].

In this paper, it will be presented the DETEC-PC software designed and developed to be an integral part of the measurement-detection system that allows carrying out thyroid uptake functional studies. In its development were taken in account medical practice in realization of Iodine thyroid uptake studies in a way to implementer and to promote the good medical practices.

The application software controls and directs the operation of the system. It resides in a personal computer and it communicates trough a RS-232 serial interface with the measurement module that has a microcontroller of the 51 family with a tailored BIOS. The microcontroller trough a multiple DAC of 8 bits of resolution (AD7228), supplies the voltages of control necessaries to adjust and to control the different analogical blocks. This software, among other functions, carries out the statistical analysis of the batch of samples and it has a database where the

information of the patient under study is saved. The software was designed according to the principles of Object Oriented Programming (OOP) using C++ language, with a graphic user interface (GUI) under MS-Windows environment, allowing access to all machine resources normally available to users [2]. With present advances in medical electronic instrumentation and the growing processor power, the inclusion in the software of functions that go beyond the primitive functionality and increase the easy of use or friendliness and diagnostic capabilities is a must, to keep in pace with the state of the art and the expectations of the users.

MATERIALS AND METHODS

Problem conceptualization

Typically, every week, a batch of up-to 100 samples of a radioactive Iodine solution is prepared with a dose from 7 to 10 µCi each [3]. This batch is analyzed statistically: the arithmetic mean of counting, the standard deviation, and the coefficient of variation are calculated. If the coefficient is bigger or equal to 5%, the batch of samples is thrown away because of bad preparation. On contrary case, It is determined a pattern sample, it is calculated the confidence interval and the disposable samples are determined.

Based on the pattern sample, the measurement time is determined for all the samples of the batch. Once, the patient ingested the radiopharmaque, it begins the process of serial measurements. These are carried on at 2, 4, 6, 24, 48, 72 and 96 hours. At 2 and 24 hours, an evaluation of the patient is performed and a decision can be taken as shown in the following table:

Classification of patients according to Uptake percent.

Evaluation at 2 hours		
Uptake %	**Diagnosis**	**Decision**
From 0 to 4	Hypothyroidism	Measurement goes on
From 5 to 16	Euthyroidism	End of study
Bigger than 16	Hyperthyroidism	Measurement goes on
Evaluation at 24 hours		
From 0 to 9	Hypothyroidism	End of study
From 10 to 30	Euthyroidism	End of study
Bigger than 30	Hyperthyroidism	Measurement goes on, to calculate Effective Mean Life (EML)

Use of DETEC-PC

The use of DETEC-PC is illustrated through the software's main window (see figure).

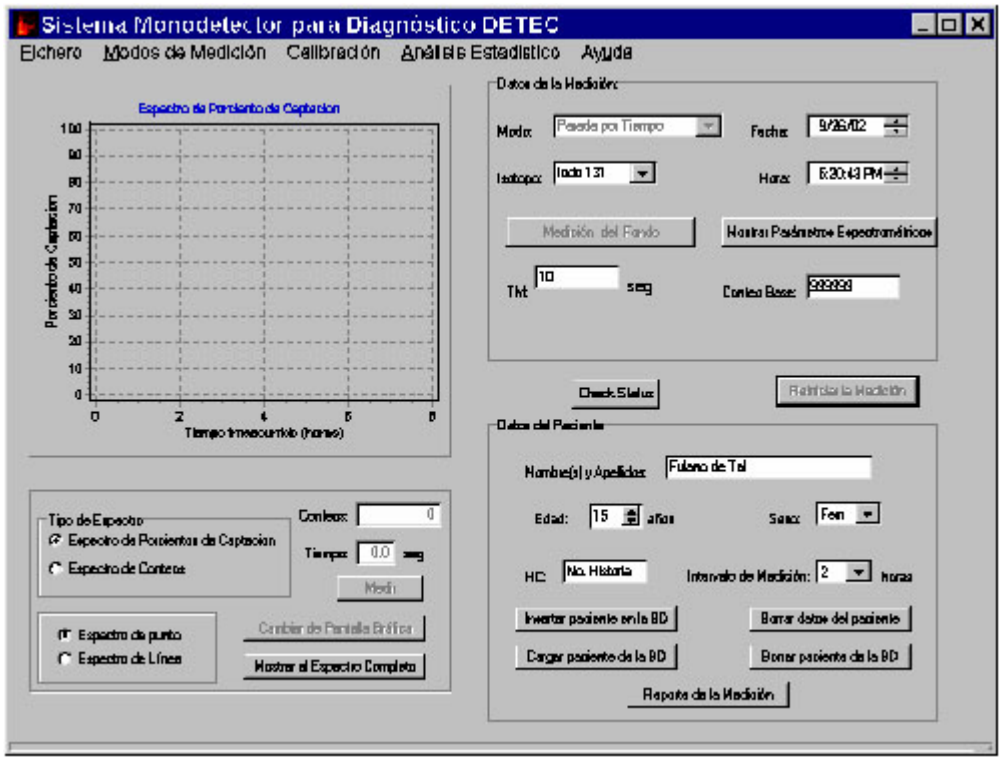

Figure. Main window of the software.

1- Patient registration
In order to include a new patient is necessary to enter the following data: Nombres y Apellidos (name and family), Sexo (sex), Edad (age) and its HC Número de Historia Clínica (clinic history number). This can be done in the editing boxes available in the program main window. The patient will be inserted by clicking the button Insertar paciente en la BD (insert patient in the DB) or automatically when the measurement of the first interval is done.

2- Patient deleting
In order to eliminate a patient from the database follow these instructions:
- Set its Clinic History number (HC).
- Click the button Borrar Paciente de la BD (delete patient from the DB)
- Key in the password for this operation when asked for.

3- Measurement data
The software allows control of the following measurement aspects:
- Intervalo de Medición (measurement interval) Selection. It is the time in hours elapsed from the radiopharmaque ingestion in which it is established to measure according to the study methodology; those are: 2, 4, 6, 24, 48, 72 y 96 hours.
- Measurement mode selection.
The system has two Measurement Modes: Stopping by Time and Stopping by Counting.
- Fecha (date) and Hora (time).
It shows PC date and time.
- Measurement time
It is the time set for measuring the patients under Iodine thyroids uptake study. It is set in the TM editing box located in the Datos de Medición (measurement data) panel in the system main window.

4- Spectrometric parameters
It is the set formed for Lower Threshold, Threshold Window, Gain and High Voltage that allows obtaining the isotope peak under measurement.

5- Isotope selection
It allows selecting with which of the available isotopes the system is going to work: ^{125}I, ^{99m}Tc, ^{59}Fe, ^{51}Cr, ^{57}Ga, ^{57}Co and ^{131}I. With the isotope selection, spectrometric parameters (lower threshold, threshold Window, gain and high voltage) are fixed for said isotope
The selection can be done in two ways:
- Trough the option Modos de Medición - Selección de Isótopo (measurement modes-isotopes selection) from the main menu bar.
- Through the Combo Box Isótopo (isotope) located in the Datos de Medición (measurement data) panel in the system main window.

6- Statistical analysis
It allows the measurement and statistical analysis of a batch of up to 100 samples. This option is entered Trough the option Análisis Estadístico (Statistical Analysis) from the main menu bar.
It takes the measurement time from the main window. And it is necessary to indicate the number of samples of the batch in an editing box to this effect, and to manually activating the measurement of every following sample.

7- System calibration
The calibration option allows obtaining energy spectrum of the radioisotope by sweeping the lower threshold with a fixed threshold window. This option is entered through the option system Calibración (calibration) from the main menu bar. In this mode is necessary to fix the following spectrometric parameters: high voltage, gain, lower threshold of beginning, and fixed threshold window, the spectrum is displayed in a graphics and optimal values for the lower threshold and window for the main peak of the spectrum are found and fixed for the isotope selected in the program main window. The user can override this automatic feature.

RESULTS

System analysis

From the cases of system use derives that it can be divided en three subsystems:
- Measurement subsystem,
- Statistical analysis subsystem,
- Calibration subsystem.

Measurement subsystem

- There were designed two measurement modes: stopping by time and stopping by counting. These modes were implemented through menu bar options and combo list boxes in the measurement panel of the system principal window.
- It is defined as measurement interval the time, in hours, elapsed after the ingestion of the radiopharmaque, to the moment in which it is established to carry out the measurement.
- Measurements are carried out for growing values of measurement intervals.
- It is defined a PARADOX database where are stored the patient data and measurement data. Each registry from the table contents the following information: Name, Age, Sex, Clinic History (CH), Date of beginning of study, Time, Kind of spectra and measured values for each interval. To insert a patient in the database must be specified his clinic history number On the contrary case measurements could be carried on, but information will not be saved in the database.
- A patient can be introduced into the database in two ways: either when it is going to be measured for the first time or through the button Insertar Paciente en la BD (to insert patient into the DB).
- The information of a patient can be loaded in the system on two ways: when its measurement it is going to be carried out, then the system automatically will search for the data of such

patient trough the database and will show it on the screen, adding finally the outcome of the measurement in the interval in question. If the search trough the DB fails, then in that very moment is inserted. The second way is through the button Cargar Paciente de la BD (Load patient from DB). If the patient is not found, then it will be notified trough a screen message.
- For a patient to be eliminated from the database is necessary to specify the password that allows to erase information.
- Visualization on the screen of two kinds of spectra: espectro de conteos (counting spectrum) and espectro de por cientos de captación (percent uptake spectrum).
- Taking into account the characteristics of measurement intervals that: first three are carried out at 2 hours intervals, then the next at 24 hours, and from so on with a frequency of 24; it was decided to show the spectrum in two parts: in the first the axis correspondent al time in hours has a range from 0 to 8 and in the second a range from 24 to 96. These two spectrum zones are swapped through the button Cambiar de pantalla gráfica (Change graphic screen).
- The option of visualizing the full spectrum with measurements of all intervals was implemented through a command button of the measurement panel Mostrar el espectro complete (Show full spectrum).
- Primary evaluation of measurement results at 2 and at 24 hours.

Statistical analysis subsystem

In this subsystem all statistical parameters mentioned before are calculated. The user can cancel batch of samples measurement at any time and results of statistical processing are displayed in a screen Window and can be saved to a file in disk.

Calibration subsystem

The calibration option allows obtaining energy spectrum of the radioisotope by sweeping the lower threshold with a fixed threshold Window. This makes possible to set optimum spectrometric parameters for measurement and to correct any shifting that had happen in these values. The system help gives information about available options and facilitates knowledge of medical and nuclear concepts related to the study.

In the system main window menu bar, the following options were defined: Fichero (file) Modos de medición (measurement modes, análisis estadístico (statistical analysis), Calibración (calibration) and Ayuda (help). Its working area is divided en three panels: Datos de la Medición (measurement data), Datos del Espectro (spectrum data) and Datos del Paciente (patient's data).

Software Facilities

The application software DETEC has the followings facilities:
- Measurement of a batch of samples and performing all its statistical processing.
- Determination of the measurement time to employ in the study.
- Displaying of spectrum in counting or in percents of uptake.
- A PARADOX database where patient and Measurement data are stored.
- Automatic database information handling, from the clinic history number.
- Evaluation, at 2 and at 24 hours, of the measurement and according the percent of uptake calculated value suggestion of a diagnostic for a decision taking. Calculation of EML, in those cases in which is necessary.
- A calibration option, with which the radiopharmaque energy spectrum can be obtained sweeping the lower threshold with a fixed window.
- An on-line help.

The system main window is divided en three panels: measurement data panel, spectrum data panel and patient data panel. They were defined six working modes: stopping by time, stopping by counting, isotope selection, calibration, statistical analysis, effective mean life.
In the system main Window menu bar, there were defined the following entries: file, measurement modes, statistical analysis, calibration and help.

DISCUSSION

Model of objects

It was defined the abstract class EQUIPO as root to the hierarchy, its attributes are: date, time, threshold window, high voltage and gain.

Subclasses are CALIBRACIÓN, LOTE_MUESTRAS, and CAPTACIÓN_YODO. CALIBRACIÓN class attributes are: calibration spectrum number of points, values for this spectrum and maximum counting position. LOTE_MUESTRAS class attributes are: batch size (quantity of samples), batch measurement time and counting values of these samples. CAPTACIÓN_YODO class attributes are: measurement mode, pattern sample counting, and measurement time to measure patients and counting value that is obtained of such measurement on an interval.

Subclasses are PCO_ESTAD_YODO and PACIENTE. PCO_ESTAD_YODO class attributes are: arithmetic mean, standard deviation, variation coefficient, interval of confidence limits and pattern sample number. PACIENTE class attributes are: patient personal data, its clinic history number, measurement interval, the set of all measured values at different intervals and the kind of spectrum. CAPTACIÓN_YODO and

LOTE_MUESTRAS are intermediate classes and CALIBRACIÓN, PCO_ESTAD_YODO and PACIENTE are terminal classes that form the leaves of hierarchy, being the same concrete classes. This hierarchic organization is complex because there are multiple inheritances being PACIENTE class daughter of two parents.
It is defined in the EQUIPO class a pure virtual function: Medir, which functionality is defined in descendant classes and in each one of them is different. This method in the CALIBRACIÓN class measures the pattern source. In the LOTE_MUESTRAS class measures a batch of samples. In the CAPTACIÓN_YODO class measures time to reach base counting to determinate patient measurement time and in the PACIENTE class measures emitted radiations from patient's thyroids gland.

CONCLUSIONS

The application software design follows the concepts of OOP with its inherent characteristic of code reusability [4], allows creating new application softwares for others studies with minimal effort, for that it will just have to add new specific classes for future new applications and these new classes will inherit from the existing ones. In the design of the DETEC–PC have been taken in account the requirements of easiness of use and the good medicals practices. In the software design was taken in account the extensibility of the presented solution to the measurement with others radioisotopes used in Medicine Nuclear as: ^{125}I, ^{99m}Tc, ^{59}Fe, ^{51}Cr, ^{57}Ga, ^{57}Co and not only of ^{131}I.

REFERENCES

[1] Tiroides. Colegio Internacional de Médicos Nucleares A.C. ,1999.
[2] Software Orientado a Objeto, Addison Wesley, 1993.
[3] Física Médica y Biológica, MIR, Moscu,1991.
[4] Object-Oriented Analysis, Yourdon Press Computing Series, Prentice Hall Building, 1991.

BIBLIOGRAPHY

[1] Object-Oriented Modeling and Design, Prentice Hall, Englewood Cliffs.1995, Applying OMT, SIGS Books,1991.
[2] Quality Control of Nuclear Medicine Instruments. TecDoc 602. IAEA, Viena,1988.
[3] Software Orientado a Objeto, Addison Wesley, 1993.
[4] Textbook of Nuclear Medicine, Vol II. Lea & Febiger, Philadelphia,1984.
[5] Strategies for Real-Time System Specification, Dorset House, New York, 1988.
[6] Programando in C++, Editora Campus, 1993.
[7] Object-Oriented Software Engineering: A Use Case Driven Approach. Addison-Wesley, 1992.
[8] Hyperthyroidism, http://cpmcnet.columbia. Edu/dept/thyroid/index3.htlm, 2001.
[9] Ingeniería del Software: Un enfoque práctico. Mc Graw Hill, Madrid, 1993.
[10] Principios básicos de investigación clínica, Editorial Zeneca FARMA, Ediciones Ergon S.A. Madrid,1993.
[11] Windows Wisdom for C and C++ Programmers, John Wiley and S., New York, 1993.
[12] Introducción a la Programación Orientada a Objetos, Addison-Wesley Iberoamericana, 1994.
[13] C++ Tutorial for MS-DOS and Windows Operating Systems, Microsoft C++ Version 7.0, 1992.

Received: December 16, 2003
Accepted: February 4, 2004

RECENT ADVANCES ON X-RAY IMAGING WITH A SINGLE PHOTON COUNTING SYSTEM

Giuseppe Baldazzi[1], Dante Bollini[1], Ana Ester Cabal Rodríguez[2], César Ceballos Sánchez[2] ,Wladyslaw Dabrowski[3], Angelina Díaz García[2]; and other authors*

[1]Dipartimento di Fisica dell'Università di Bologna and INFN, Bologna, Italy
[2]Centro de Aplicciones Tecnológicas y Desarrollo Nuclear (CEADEN), Calle 30 No. 502 e/ 5ta Ave. y 7ma, Playa, Ciudad de La Habana, Cuba
[3]Faculty of Physics and Nuclear Techniques, University of Mining and Metallurgy, Cracow, Poland
[4]Dipartimento di Fisica dell'Università di Ferrara and INFN, Ferrara, Italy
[5]INFN, Torino, Italy
[6]Universidad de los Andes, Bogota, Colombia
[7]Dipartimento di Fisica Sperimentale dell'Università and INFN, Torino, Italy
[8]CINVESTAV, Mexico City, México
[9]DISTA, Università del Piemonte Orientale and INFN, Alessandria, Italy
[10]University of Antwerp, Antwerp, Belgium
acabal@ceaden.edu.cu

ADELANTOS RECIENTES EN LA IMAGENOLOGÍA RADIOGRÁFICA CON UN SISTEMA DE EMISIÓN DE FOTÓN SIMPLE

Resumen

Se presenta un diseño y algunos resultados recientes obtenidos con un sistema de emisión de fotón simple, que consiste en 384 detectores de microbandas de silicio unidos con seis circuitos electrónicos multicanales RX64. Cada circuito consta de un preamplificador de carga, un conformador, un discriminador y un contador de 20 bits para cada uno de sus 64 canales. La resolución energética y la eficiencia relativa del sistema se midieron entre 8 y 36 kev utilizando las líneas de fluorescencia de rayos X tanto de una fuente 241 Am como de un tubo de rayos X, así como usando haces de rayos X cuasi-monocromáticos especialmente desarrollados para ello. La resolución espacial del sistema se verificó por medio de un tubo de rayos X de microfoco equipado con capilares. Se obtuvieron imágenes de objetos de prueba angiográfica y mamográfica, las cuales posteriormente se procesaron con la técnica de substracción de doble energía. En particular, se evaluó el contraste de un fantoma angiográfico para diferentes concentraciones de una solución de yodato, la cual fue inyectada en vasijas de 1 mm y 2 mm de diámetro. Los primeros resultados con la versión del circuito de umbral doble, así como los métodos de prueba tanto del detector como del circuito se presentaron también.

Abstract

We present the design and some recent results obtained with a single photon counting system consisting of 384 silicon microstrips of 100 micron pitch equipped with 6 RX64 ASICs, which include a charge preamplifier, a shaper, a discriminator and a 20-bit counter for each of their 64 channels. The energy resolution and the relative efficiency of the system was measured between 8 and 36 keV using fluorescence X-ray lines from both an Am-241 source and an X-ray tube, and using specially developed quasi-monochromatic X-ray beams. The spatial resolution of the system was verified using a microfocus X-ray tube equipped with capillaries. Images of angiographic and mammographic test objects were obtained in scanning mode with dual energy X-ray beams and were then processed with the dual energy subtraction technique. In particular, the contrast for the angiographic test object was evaluated for different concentrations of an iodate solution injected into 1 mm and 2 mm diameter vessels. First results from the double threshold version of the ASIC, as well as detector and ASIC testing methods, are also presented.

Key words: fluorescence analysis, biomedical radiography, digital systems, image processing, position sensitive detectors, readout system, semiconductor detectors

*Mauro Gambaccini[4], Paolo Giubellino[5], Mirko Gombia[1], Pawel Grybos[3], Marek Idzik[3], Juana López Gaitán[6], Alberta Marzari-Chiesa[7], Luis Manuel Montano Zetina[8], Francesco Prino[9], Luciano Ramello[9], Anna Sarnelli[4], Mario Sitta[9], Krzysztof Swientek[3], Angelo Taibi[4], Enrico Tomassi[7], Alessandro Tuffanelli[4], Piet Van Espen[10], Piotr Wiacek[3]

INTRODUCTION

This paper reports about design, construction and X-ray imaging results obtained with a one-dimensional array of silicon strips. Such an array, consisting of microstrips with 100 mm pitch and 10 mm length, was chosen for the following reasons:

• a good spatial resolution can be obtained with a reduced number of channels;

• spatial resolution in silicon is Compton scattering limited in our energy range (18-40 keV), so reducing the pitch below 50-100 mm is not really useful.

In addition, some important advantages of a digital, single photon counting system for X-ray imaging have been considered: (1) a higher efficiency with respect to conventional screen-film systems can be obtained (to achieve this, at energies above 18 keV, edge-on orientation of the strips is necessary (see figure 1); (2) digital processing, transfer and storage of images is more convenient; (3) by implementing a double threshold scheme in the front-end electronics, double energy imaging with simultaneous exposure becomes possible.

In fact, the dual energy technique introduced by Alvarez and Macovski [1] (see also [2]) allows to isolate materials characterized by a different energy dependence of the linear attenuation coefficient. This technique can be implemented in a small-scale installation thanks to the development of quasi-monochromatic beams [3-5]. The applications foreseen for our detector are dual energy angiography at the iodine K-edge (≈33 keV), and later at the gadolinium K-edge (≈50 keV), and dual energy mammography.

The efficiency of 300 μm thick silicon in the usual "front" configuration is too low in the interesting energy range (see figure 1. left panel); for this reason we have adopted the so called "edge-on" configuration which, for a strip length of 10 mm and an inactive Si layer of 0.765 mm, gives a reasonable efficiency. This has been anticipated with calculations of the efficiency ratio between the two configurations, as shown in figure 1, right panel (where both simple calculations based on the cross-sections and detailed simulations with GEANT 3.21 are reported), and later confirmed experimentally by exposing our detector to quasi-monochromatic beams (see data points in figure 1, right panel).

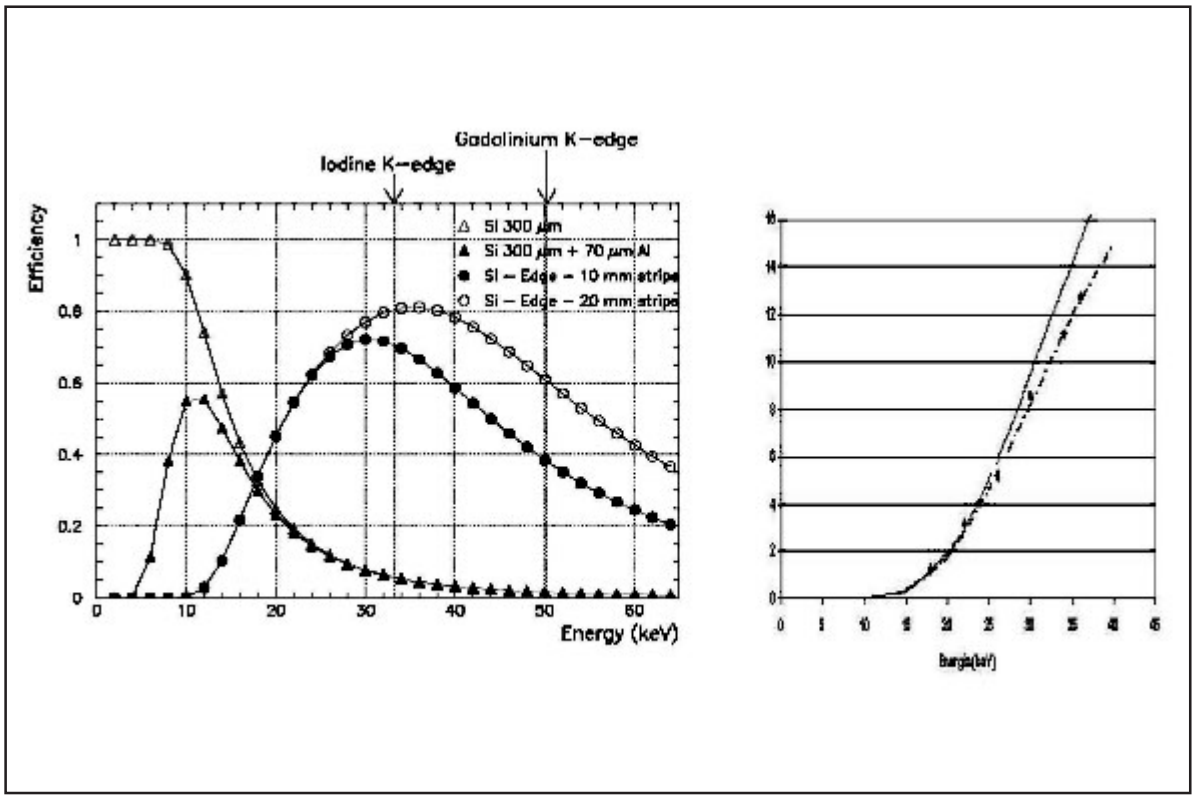

Figure 1. (Left) Calculations of photoelectric conversion efficiency vs. energy for silicon of 300 μm thickness with strips perpendicular (front) or parallel (edge) to the incoming beam. (Right) Ratio of edge to front configuration efficiency vs. energy: calculation (continuous line), result of GEANT 3.21 simulations (broken line) and experimental data (points). Cross-section data from the XCOM database of NIST at http: //physics.nist.gov/PhysRefData.

Detector and electronics

Our silicon microstrip detectors (132 or 400 strips of 0.1 mm pitch, 10 mm length) are AC-coupled ones with FOXFET biasing[1], featuring a low current of about 60 pA per strip at 100 V bias voltage, which is a key requirement for low noise performance. A picture of the corner of one detector is shown in figure 2, where the bias line and the guard ring are visible around the strips.

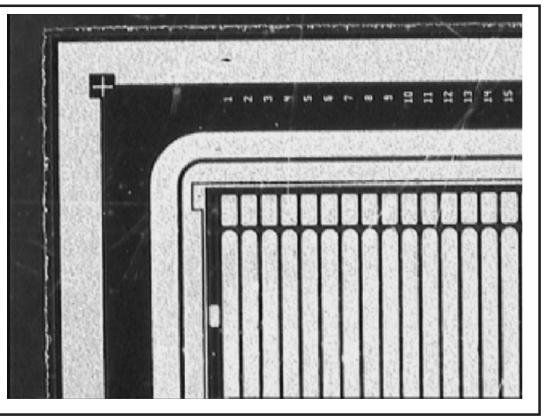

Figure 2. Picture of a corner of the microstrip detector. The physical edge, guard ring, bias line and first 15 strips are visible.

Detectors before assembly were tested with a semiautomatic Alessi probe station REL 4500: I-V and C-V measurements were performed (using the Hewlett Packard semiconductor parameter analyzer 4145B and the LCR meter 4284A) in order to select the ones with fewer defective strips. In particular we have measured the dark current of each strip and the integrity of each decoupling capacitor.

The RX64 ASIC integrates 64 channels of front-end (preamplifier, shaper, discriminator) and 64 counters with 20 bit range, as well as several internal DACs, used to provide internal voltages which control the ASIC's preamplifier gain and shaping time. An internal calibration system is also present, so that the chip can be controlled by a purely digital interface: we have used National Instruments' I/O cards PCI-DIO-96 on a desktop computer and DAQCard-DIO-24 on a portable computer. Detail on the ASIC design and performance are given in [6,7]. Recently we have developed a double threshold version of the RX64 ASIC, featuring two discriminators per channel, and correspondingly two counters per channel; this version is aimed at the dual-energy mammographic application, where it is crucial to count the photons of each of the two energies at the same time, allowing an accurate implementation of the energy subtraction technique.

In the past we have tested the functionality of each ASIC after mounting it on the printed circuit board, a method which requires to strip off a malfunctioning ASIC and replace it with a new one. This has become impractical for assembling arrays of 6 or more ASICs, particularly when the yield is less than 50%. Thus, we have developed a probe card[2] (see figure 3) which allows to test one ASIC at the time, using the same cable, power supply, acquisition card and LabVIEW 6.0 program which is used for ASICs assembled on PCBs. First tests of the double threshold ASICs with the probe card are under way.

Results presented in the following have been obtained with two prototypes, the first one featuring 128 equipped channels (132 microstrip detector read

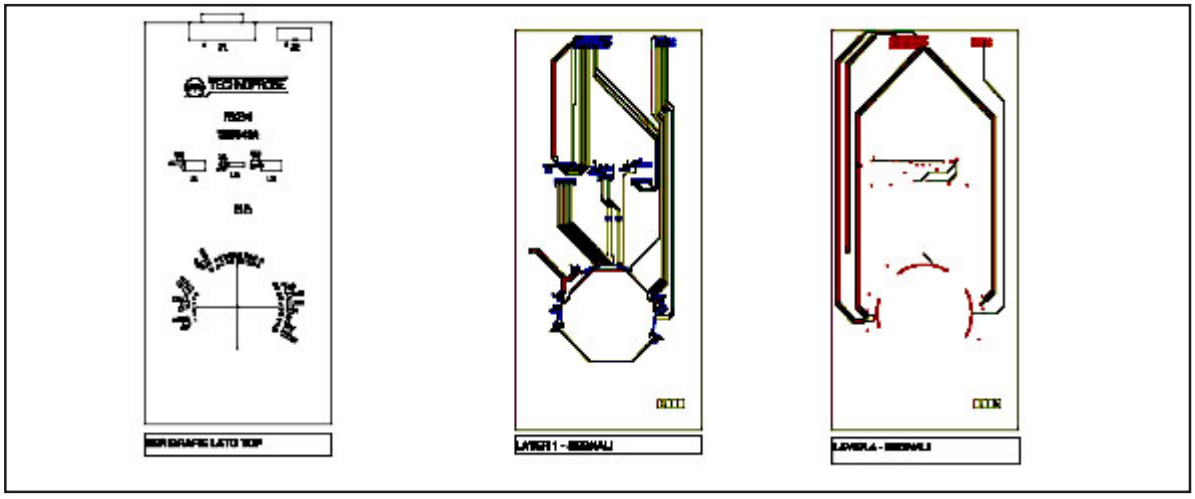

Figure 3. Physical layout of the probe card designed for the RX64 ASIC: placement of components (left), top layer (centre), bottom layer (right).

[1]They were designed and manufactured by ITC-IRST, Trento, Italy.
[2]The probe card has been constructed by Technoprobe S.r.l., Cernusco Lombardone (LC), Italy.

by two ASICs), the second one featuring 384 equipped channels (400 microstrip detector read by six ASICs). For the second prototype, a pitch adapter was inserted in between detector and ASIC (see figure 4), in order to simplify the task of bonding strips to electronic channels and also to allow reworking of the assemblies in case of failure of a component.

Figure 4. Detail of the pitch adapter (middle) which connects the detector (top) to each of the 6 RX64 ASICs (bottom).

Energy resolution

The performance of the two prototypes was tested with several methods, starting from internal calibration, which means injecting a known charge at the input of each electronic channel by means of a test capacitor (75 fF). Dealing with a digital system, the analog performance must be obtained via discriminator threshold scans. Figure 5 (a summary of 12 such scans) shows that the RX64 response is reasonably linear up to ≈8000 electrons (29 keV), after which some saturation is observed.

Further tests were performed by irradiating the prototypes with fluorescence X-rays generated either by an americium source or by a Cu-anode X-ray tube: a collection of spectra is shown in figure 6. They were used to establish the absolute energy calibration of the detector. More details on the energy resolution can be found in [8]. The summary of gain and noise measurements is given in table, which refers to two different peaking time settings (resp. Short and Long), corresponding to different gains as well. The best performance of the 384-channel prototype (last line of the table) is about 150 RMS electrons, corresponding to about 1.3 keV FWHM at 22 keV energy.

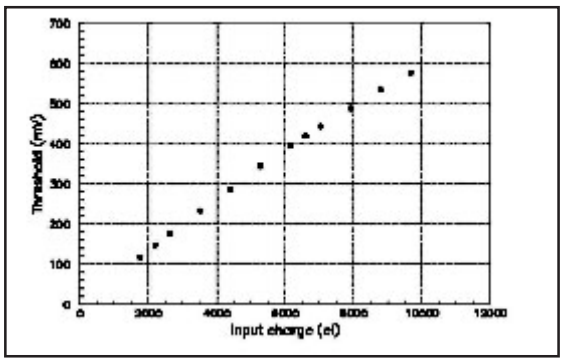

Figure 5. Correlation between injected test charge (electrons) and measured signal (mV).

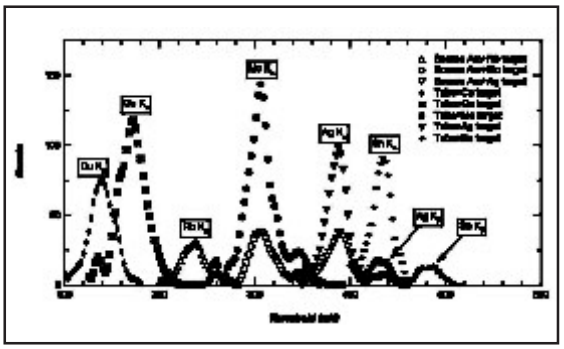

Figure 6. Energy spectra obtained with source or tube fluorescence setups, showing peaks ranging from 8 keV to 28 keV. The horizontal scale, in mV, has not been corrected for non-linearity.

Recently we have obtained first results on the analogue performance of the double threshold version of the RX64 ASIC, where two discriminators per channel have been implemented. First of all, the gain shows good uniformity over the channels of one ASIC, with an average value of 54.8 μV/el and a r.m.s. value of 0.45 μV/el; the offset is also satisfactory, with an average value of 17.8 mV and a r.m.s. value of only 1.1 mV. The superposition of many single channel spectra obtained with the RX64-DT is shown in figure 7; it is important to stress that these differential spectra have been obtained directly with a moving "hardware" energy window, while previously we had to differentiate offline the integral spectra. The equivalent noise charge (196 electrons on average) obtained from the above mentioned spectra shows a moderate increase with respect to the standard ASIC; we believe that the increased noise is due to two sources: on one hand the increased temperature of ASIC and detector, due to a higher power dissipation, on the other hand the shorter shaping time. Peltier cooling is being considered in order to reduce the effects of the first source.

Measured Gain and Noise (ENC = Equivalent Noise Charge) for several detector + ASIC configurations

Module (P.A. - Pitch Adapter)	T (peak)*	Gain μV/electron	ENC RMS electrons
Detector + 2 × RX64	Short	61.6	131
Detector + 1 × RX64 - DT	Short	54.8	196
6 × RX64	Short	63.7	176
6 × RX64	Long	82.8	131
6 × RX64 + P.A.	Short	63.7	184
6 × RX64 + P.A.	Long	82.8	148
Det. + P.A. + 6 × RX64 (Standard preamplifier setting)	Short	63.7	182
Det. + P.A. + 6 × RX64 (Optimized preamplifier setting)	Short	63.7	151

*Short = 0,5 μs , Long = 1,0 μs

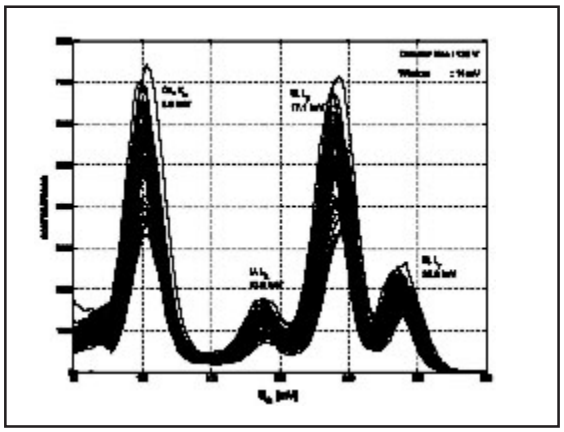

Figure 7. Energy spectra obtained with the RX64-DT ASIC using a Pu source and a Cu absorber.

Spatial resolution

In order to assess the spatial resolution of the silicon strip detector, measurements were taken with a capillary output microbeam [9] at the Antwerp's University Micro and Trace Analysis Center (MiTAC). Preliminary results have been reported in [10]. The microbeam, produced by an X-ray tube with Mo anode operated at 15 kV (followed by the capillary and by a Mo filter), has an RMS of about 28 μm (see figure 8), as deduced from a fluorescence measurement on a Ni-Cr wire. Beam profiles taken with our silicon detector indicate a good correlation between the known beam position and the beam centroid obtained by the detector (see figure 9). The maximum deviation from the straight line is ± 0.12 strips, corresponding to 12 μm. The undulations which are seen in the figure are mainly due to the 100 μm strip quantization; in fact, a simple simulation (which neglects both charge diffusion in silicon and Compton scattering) shows that they are compatible with a gaussian beam having 28 μm RMS.

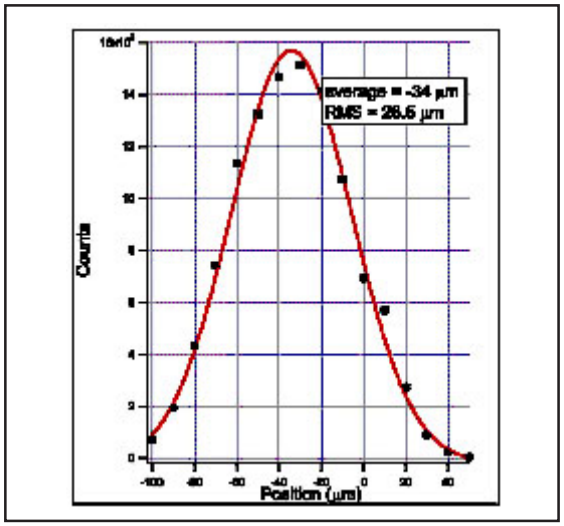

Figure 8. Position scan of the X-ray microbeam obtained by counting fluorescence photons from a 25 μm diameter Ni-Cr wire (filled circles). Also shown is a gaussian fit (continuous line).

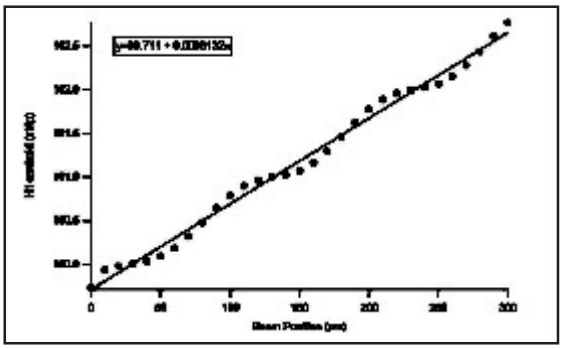

Figure 9. Correlation between centroid measured by microstrip detector (in strip units) and real beam position (in μm).

Later on we have also taken data with a 100 μm diameter pinhole (see figure 10) interposed between the capillary output and the detector, in order to reduce the non-gaussian tail of the microbeam, which can significantly affect our position resolution. A preliminary analysis of these data indicates that the maximum deviation from a straight line in the correlation between the known beam position and the measured beam centroid has been considerably reduced.

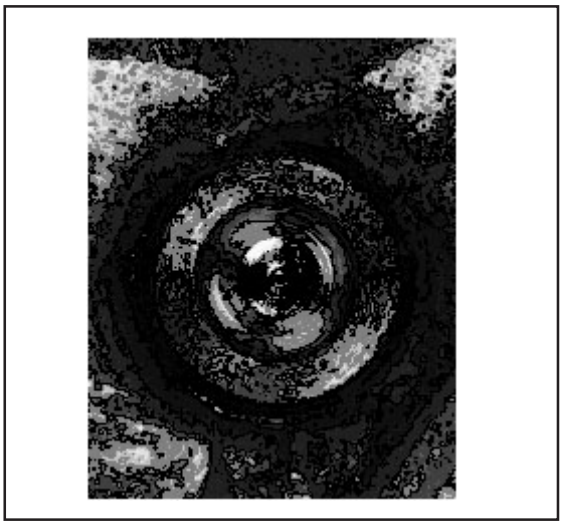

Figure 10. The 100 μm diameter pinhole (seen from the beam side) in a 2 mm dia. In disc, inserted in a Pb sheet.

Mammographic imaging

The 384-channel prototype has been used for a test on the dual energy quasi-monochromatic beams at the University of Ferrara. For this test, a mammographic phantom consisting of a PMMA block with 6 mm diameter cylindrical inclusions of polyethylene and water (for more details see [11]) has been placed between the beam and the silicon detector, as shown in figure 11. Image were collected separately at three pairs of energies, namely low (16, 18 and 20 keV) and high (32, 36 and 40 keV), since the double threshold ASIC was

not yet available at that time. A projection algorithm [2,11] has been implemented in order to find the projection angle which makes the contrast between two chosen materials to vanish, as shown in figure 12 for the energy pair (18, 36) keV. Thanks to the good signal-to-noise ratio at 36.5 degrees (where the contrast between PMMA and water vanishes), the polyethylene pattern is well visible in the combined experimental image, shown in figure 13 (top). Detailed simulations of the experimental setup are in fair agreement with measurements at two of the three energy pairs, while it appears that the images taken at the highest energy pair are limited by insufficient statistics.

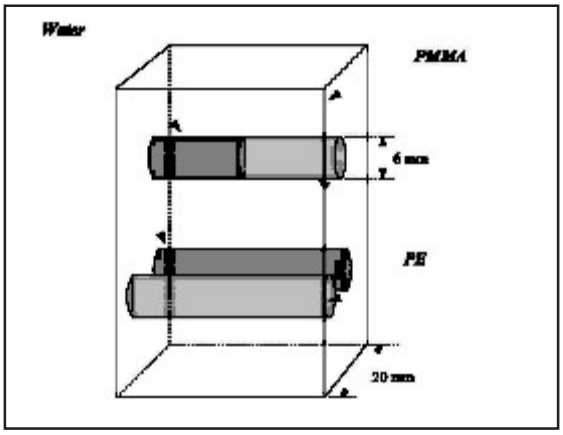

Figure 11. Slice of the mammographic phantom.

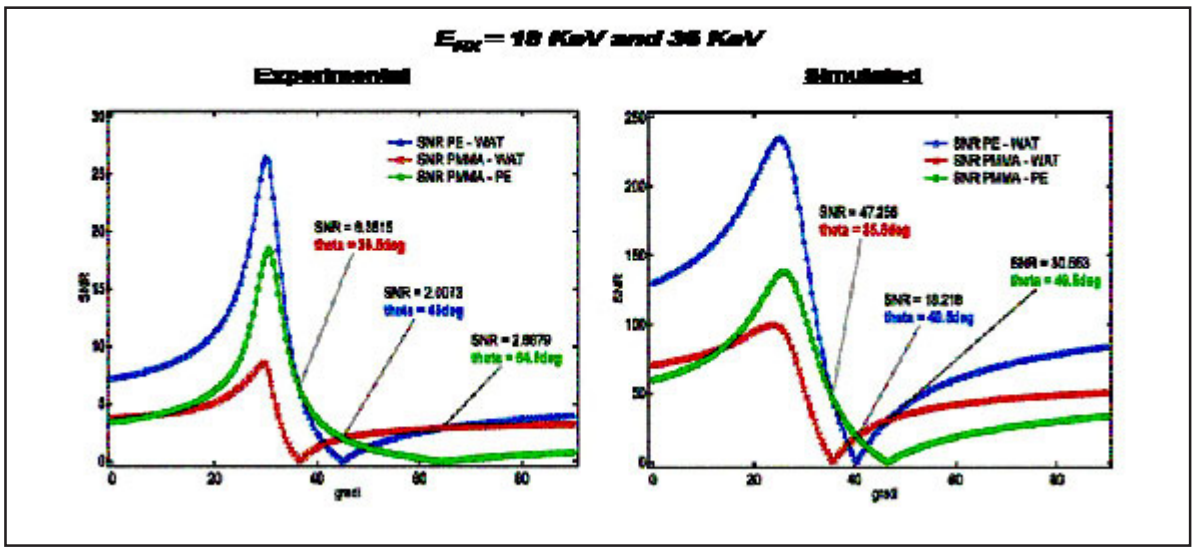

Figure 12. Signal-to-noise ratio vs. projection angle for the pairs of materials PE-water (triangles), PMMA-water (crosses) and PMMA-PE (squares), obtained with the mammographic phantom data (left) and with a simulation program (right).

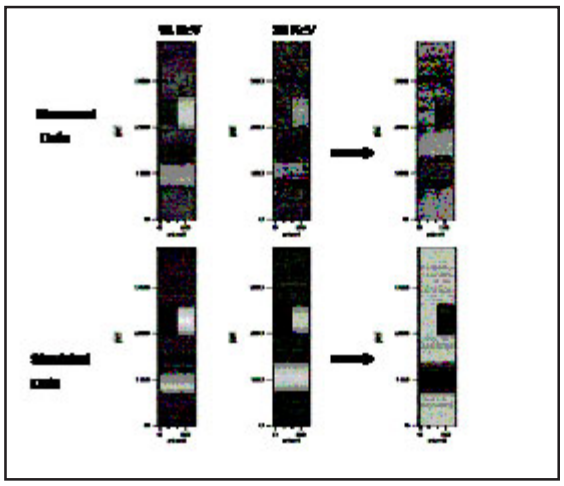

Figure 13. Images of the mammographic phantom taken at low energy and high energy, and combined image (right), for experimental data (top) and for simulation (bottom). Energies of 18 and 36 keV.

Angiographic imaging

A dedicated fixed energy angiographic beam line based on the quasi-monochromatic beams [5] has been installed at the Bologna University. We have performed a test with our 384-channel prototype and an angiographic phantom (see figure 14) containing four small tubes (1 or 2 mm diameter) filled with an iodide solution at various concentrations.

One of the images obtained off-line by logarithmic subtraction between a high energy (35.5 keV) and a low energy (31.5 keV) image is presented in figure 14, for a concentration of 92.5 mg/ml, which represents 1/4 of the standard concentration presently used in clinical practice. The background structures present in the phantom are effectively removed by this procedure. A summary of the signal-to-noise ratios obtained with 1 mm diameter tubes is shown in figure 15 as a function of the iodated concentration, together with a theoretical

calculation based on the structure of the phantom. The noise contrast was evaluated over one pixel only. Usable values of the SNR are achieved down to 92.5 mg/ml concentration, and in some cases even for 46.25 mg/ml.

A detailed simulation of the angiographic phantom has been carried out with the MCNP transport code [12]; the detector has been described taking into account the passive layer (dead silicon region in edge-on configuration) as well as the active silicon volume. The simulation results presented in [13] show a fair agreement with the experiment, both for profiles and for two dimensional images.

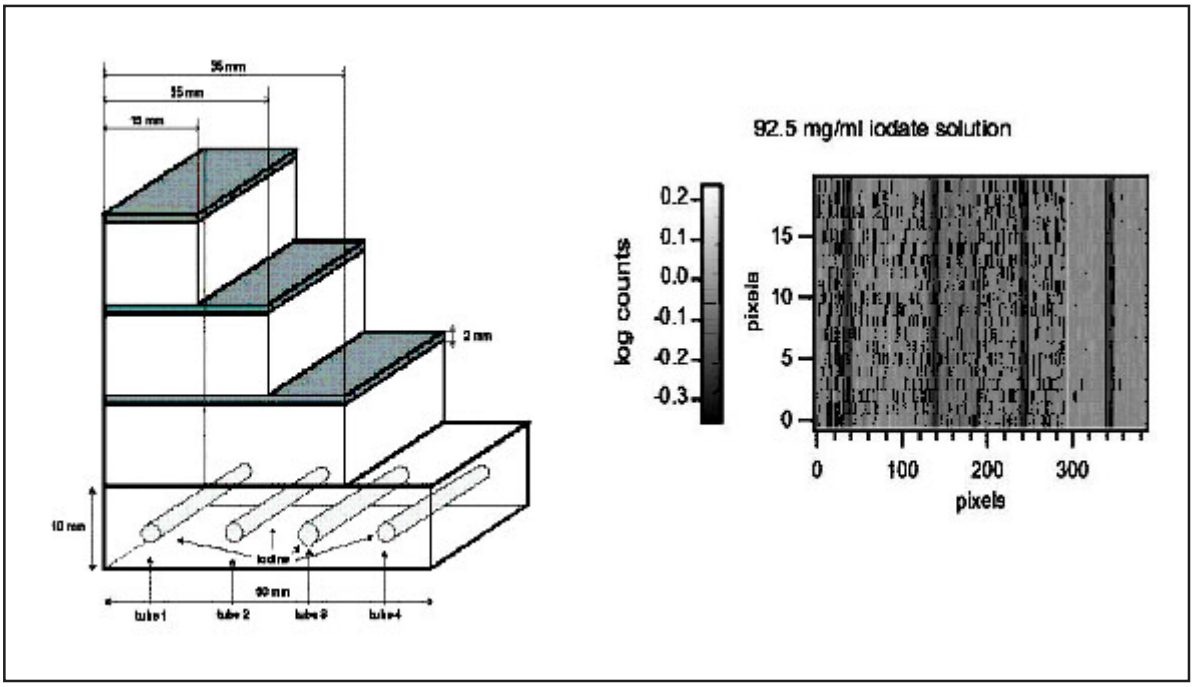

Figure 14. (Left) The angiographic phantom. Four steps of PMMA and three layers of aluminium provide the background structure, while 4 tubes in the lower part can be filled with the iodate solution. (Right) Logarithmically subtracted image of the angiographic phantom for 1 mm tubes at 92.5 mg/ml concentration.

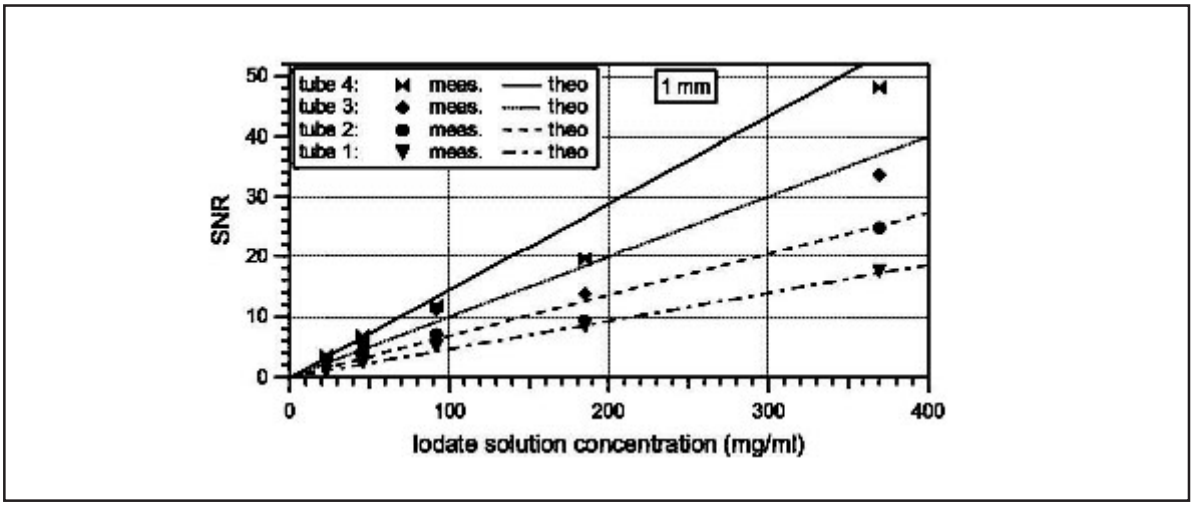

Figure 15. Measured (points) and calculated (lines) SNR values for the angiographic phantom vs. iodide concentration, for 1 mm diameter tubes.

SUMMARY AND OUTLOOK

We have developed a relatively simple linear X-ray detector for scanning mode radiography, based on a 100 μm pitch silicon microstrip detector and on the RX64 ASIC. Prototypes with 128 and 384 strips of
10 mm length have been built and tested with internal calibration, fluorescence X-rays and quasi-monochromatic beams in the energy range from 8 to 36 keV. The obtained energy resolution (about 150 rms electrons, i.e. 1.3 keV FWHM at the Ag K_α peak at 22.1 keV) is well adapted to the energy spread of the presently available quasi-monochromatic beams. The efficiency for photoelectric conversion in edge mode with 10 mm active silicon (preceded by about 0.8 mm inactive silicon) is sufficient to perform double energy mammography (for example at 18 and 36 keV) and double energy angiography at the iodine K-edge.

Recent preliminary imaging results with a mammographic phantom consisting of PMMA, PE and water indicate that contrast cancellation between PMMA and water can be obtained by the projection method, keeping a signal-to-noise ratio of 16 for polyethylene. Imaging tests with an angiographic phantom containing 1 mm tubes indicate that it is possible to obtain good contrast at iodate concentrations well below the current clinical practice one of 370 mg/ml. The first results on the performance of the double threshold version of the RX64 ASIC show that the Equivalent Noise Charge is only 30% higher than the one obtained with the standard ASIC, in spite of the increased complexity and level of digital noise inside the ASIC. Extensive simulations have been developed with both the GEANT 3.21 and the MCNP transport codes, which are in fair agreement with the experimental results.

Future developments will include the following points:
• implementing larger detectors to match the image size required in the clinical applications;
• measuring the DQE and MTF of the system using the capillary output X-ray beam at MiTAC, Antwerp University;
• implementing synchronization of X-ray counting with the diastolic phase of the hearth cycle for coronary angiography;
• considering the possibilities for angiography at the gadolinium K-edge at 50 KeV;
• building a full-size mammography detector with the double threshold version of the RX64.

ACKNOWLEDGEMENTS

We are grateful to B. Pini for help with assembly of detectors and ASICs, to E. Filoni for the layout of the pitch adapter and to F. Rotondo for help with cabling. R. Wheadon gave us precious assistance in setting up the automated bonding procedure. This work was supported by the Ministero dell' Università e Ricerca Scientifica e Tecnologica (MURST) of Italy under contract N. COFIN-2000-MM02095297-003, and partially supported by the Polished State Committee for Scientific Research. CEADEN's researchers acknowledge the support from the ICTP Programme for training and research in Italian laboratories (ICTP-TRIL).

REFERENCES

[1] ÁLVAREZ, R.E., MACOVSKI, A., Phys. Med. Biol., 21 (1976)733.
[2] LEHMANN, L.A., et al., Med. Phys., 8(1981)659.
[3] GAMBACCINI, M., et al., Narrow energy band X-rays via mosaic crystal for mammography application, Nucl. Instr. Meth. A, 248(1995)365.
[4] TUFFANELLI, A., et al., Dichromatic source for the application of dual-energy tissue cancellation in mammography, in SPIE Medical Imaging *2002,* SPIE Proceedings 4682(2002)21.
[5] TUFFANELLI, A., et al., Novel x-ray source for dual-energy subtraction angiography, in SPIE Medical Imaging 2002, SPIE Proceedings 4682(2002)311-319.
[6] GRYBOS, P., et al., IEEE Trans. Nucl. Sci, 48(2001)466.
[7] GRYBOS, P., et al., Microelectronics Reliability, 42, (2002)427.
[8] BOLLINI, D., et al., Energy resolution of a silicon detector with the RX64 ASIC designed for X-ray imaging Nucl. Instr. Meth. A, 515(2003)458-466.
[9] JANSSENS, K., et al., Use of Microscopic XRF for Non-destructive Analysis in Art and Archaeometry, X-ray Spectrometry, 29(2000)73-91.
[10] RAMELLO, L., et al., Results about imaging with silicon strips for Angiography and Mammography, in VII Mexican Symposium on Medical Physics, AIP Conference Proceedings, 682(2003)14 - 23.
[11] FABBRI, S., et al., Phys. Med. Biol., 47(2002)1-13.
[12] MCNP4C - Monte Carlo N-Particle Transport Code System, Tech. Rep., Oak Ridge National Laboratory (2001).
[13] CEBALLOS, C., et al., Monte Carlo simulation of a silicon strip detector response for angiography applications. First approach., in VII Mexican Symposium on Medical Physics, AIP Conference Proceedings, 682(2003)185-191.

Received: December 16, 2003
Accepted: February 4, 2004

DISTRIBUTION OF VACANCY GENERATED BY THE GAMMA IRRADIATION IN YBCO SUPERCONDUCTORS

Antonio Leyva Fabelo, Carlos Manuel Cruz, Katherin Shtejer Díaz,
Centro de Aplicaciones Tecnológicas y Desarrollo Nuclear (CEADEN),
Calle 30 No. 502 e/ 5ta Ave. y 7ma, Miramar, Playa, Ciudad de La Habana, Cuba
aleyva@ceaden.edu.cu

DISTRIBUCIÓN DE LAS VACANCIAS GENERADAS POR LA RADIACIÓN GAMMA EN LOS SUPERCONDUCTORES DE YBCO

Resumen

Se estudia la distribución de las vacancias en el material superconductor desde los puntos de vista macroscópico y microscópico. El primero, de manera indirecta relaciona la distribución espacial de la energía depositada por la radiación gamma en el volumen de la muestra, con la probabilidad de ocurrencia de defectos estructurales. En las zonas donde la energía depositada es superior, es también donde se concentra el mayor número de defectos. Este estudio se realizó con los programas EGS4 y MCNP-4C para diferentes condiciones experimentales. Se demostró que existe una alta no-homogeneidad en la distribución de energía depositada, y por consiguiente, en la distribución de los defectos generados, dependiendo su perfil de la energía de la radiación incidente y de otros factores experimentales. A escala microscópica, se estudió la probabilidad de distribución no uniforme de las vacancias generadas como resultado de los procesos de ionización, y se introdujo un modelo que explica el incremento del espesor de las junturas débiles intergranulares con dosis de irradiación a partir del fortalecimiento del movimiento difusivo de los defectos estructurales en los granos superconductores estimulados por el transporte de la radiación gamma.

Abstract

The vacancies distribution in the superconducting material is studied from two points of view: macroscopic and microscopic. The first one follows an indirect way that relates the spatial distribution of the deposited energy by the gamma radiation in the sample volume, with the probability of structural defects occurrence. The zones where the deposited energy is higher are also where is concentrated the greater number of defects. This study was accomplished using the programs EGS4 and MCNP-4C for several experimental conditions. It was demonstrated that exists a high non-homogeneity in the deposited energy distribution and therefore in the distribution of the generated defects, depending their profile of the incident gamma energy and other experimental factors. At microscopic scale, the probability of vacancies generation as a result of the ionizing processes was studied and it was introduced a model that explains the increment of the thickness of the weak intergrain superconducting junctions upon gamma irradiation, taking into account an enhancement of the diffusive motions of the crystal defects in the superconducting grains caused by the transport of the gamma radiation.

Key words: barium oxides, ceramics, cesium 137, cuprates, depth dose distributions, gamma radiation, high TC superconductors, physical radiation effects, spatial distribution, superconductivity, transition temperature, yttrium oxides

INTRODUCTION

It is well known, that the electrical and magnetic properties of the high temperature superconducting materials (HTSC) are modulated by the existing in the sample crystal structural defects [1,2]. For example, a little modification in the oxygen atom concentration in the chain, as well as in the Cu-O plains in the $YBa_2Cu_3O_{7-\delta}$ samples, induce appreciable changes in its critical temperature (T_c) and critical current (J_c). It has been demonstrated that the oxygen vacancy overdoping, leads firstly to a weakening and after to the inexorably disappearance of the superconducting properties of the sample.

The gamma rays in their transport in the superconducting material interact with the sample by means of three fundamental mechanisms: photo-effect, Compton dispersion and the pair production, according to the quantum energy. As result of these interactions, point defects like "Frenkel pairs" (vacancy and interstitial atoms) may be generated.

Though some authors consider that the point defects generated by the gamma radiation are distributed homogeneously in all the volume of the material, the reality is that while higher is the gamma energy deposited in given region, higher is the probability of appearance of the mentioned defects. While higher is the defects density in given spatial region of the sample, greater will be the effect on the macroscopic properties of the material. The spatial distribution of the gamma induced defects in the sample volume will be called in future "macroscopic distribution" and distribution of the same defects at level of the HTSC grain will be called "microscopic distribution".

Macroscopic vacancy distribution induced by Gamma Irradiation

An alternative way to study the distribution of the vacancies generated by the radiation on a given material is investigating the spatial distribution of the deposited radiation energy in the volume of the target.

Below, through the mathematical simulation of the radiation transport within material we will study this distribution, and the results will allow to determine the more damaged zones and therefore, those zones where the irradiation effects on the macroscopic properties of the material should be higher.

The employed mathematical tools were the commercial code systems EGS4 [3,4] and MCNP-4C [5], taken 1 x 108 incidents photons in order to obtain a good statistics. The energy of incident gamma rays (E_γ) was selected in dependence of the experiment. The variance of each obtained value did not surpass 0.5%. The cutoff kinetic energies were taken of 611 keV (value that includes the particle rest mass energy) for the electrons and positrons, and 1 keV for the photon. As targets of gamma irradiation were taken $YB_{a2}Cu_3O_7$ ceramics with parallelogram shape (2.8 x 16 x 1.5 mm^3) subdivided in 0.4 x 0.4 x 0.15 mm^3 "voxel".

Figure 1 represents the deposited dose distribution (in normalized percents) along a line that crosses the sample through their center in the direction of the incident radiation, for three values of the $E\gamma$.

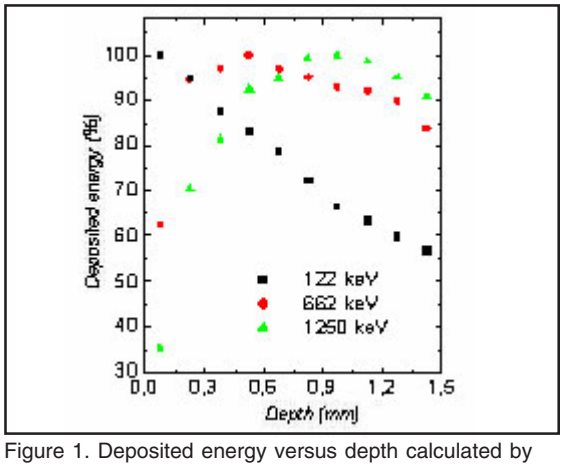

Figure 1. Deposited energy versus depth calculated by EGS4 for the three E_γ.

The curve corresponding to 122 keV shown a monotonous decrement with the deepness while the gamma rays penetrate into the sample volume. At this low $E\gamma$ the more probable interaction mechanism is the photoelectric effect, which take place with a probability ~ Z^n (n = 4 - 5 [6]), then the photons will be absorbed fundamentally by the barium atoms at the nearest to the surface regions.

The emitted photoelectrons will have a maximum initial energy similar to the Eγ and then its range will not surpass 0.1 mm [7]. Due this they will deposit their energy about the place of it origin, practically in the same voxel where took place the first interaction.

For the $E\gamma$ = 662 keV (^{137}Cs) in the figure 1 is observed, that the deposited energy distribution increase with the depth until reaching the maximum at 0.6 mm and then start to decrease. For this energy the main interaction mechanism will be the Compton effect. Now the incident photon no will be absorbed in its first interaction, it will be inelastically dispersed until their energy reduced sufficiently to be absorbed by way of photoeffect mechanism.

When E_γ = 1250 keV (^{60}Co), the behavior of deposited energy with the dose is similar to observed for ^{137}Cs with the difference that now the maximum is found at 0.9 mm. The predominant interaction mechanism continues being the Compton effect, but in this case, the high energy of the incident photons causes that are needed a greater number of dispersions to reach the necessary decay that permit it absorption. This causes that the maximum deposit zone is displaced to a greater depth.

The three up presented curves indicate the existence of an evident non-homogeneity in the spatial distribution of deposited energy in the volume of the superconducting YBCO samples irradiated with gamma rays. Taking into account the existing relationship between deposited energy and the defects generation, then we believe that identical behavior would have the spatial macroscopic distribution of the defects density in the volume of the irradiated target.

Identical simulations were accomplished with the MCNP-4C program using variance reduction techniques to increase the statistics of the experiment and reducing the voxel size in order to increase the spatial resolution.

Figure 2 shows the results of the new calculations for three photon energy values. The behaviors of the curves are similar to the determined with the EGS4 and therefore the analysis is the same. In the dependency of the energy deposited with the depth for the 122 keV gamma rays, the improvement of the statistics and the resolution permitted to identify a displacement of the maximum in tenth of millimeter with respect to the surface not observed previously.

In [8] an experiment that confirm the results of the simulation for bulk YBCO samples irradiated with ^{137}Cs gamma rays was reported.

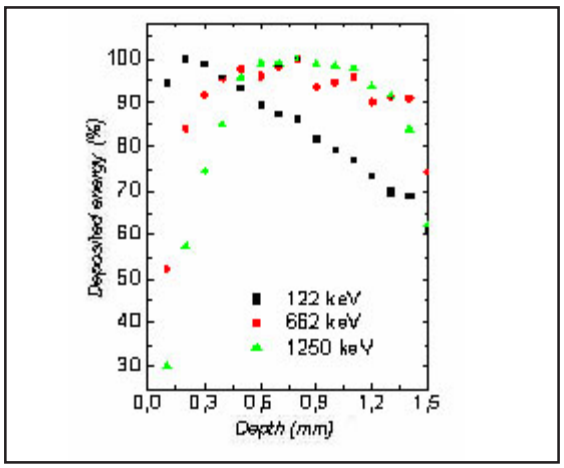

Figure 2. Deposited energy versus depth calculated by MCNP-4C for three E_γ

Microscopic vacancy distribution induced by Gamma Irradiation

Studying the effect of the ^{57}Co gamma radiation on the electrical resistance R with the temperature T in YBCO bulk samples of irradiated at room temperature with different exposition dose D_{exp}, was calculated R_0 and the coefficient of thermal variation $\acute{a}$, so that [9]:

$$R(T) = R_0 + \alpha T$$

Figures 3 (a) and (b) show the behavior of $\acute{a}$ and R0 with the D_{exp} one of the samples and call attention to two facts: a) while for a metal $\acute{a} > 0$ and should not depend of the defects density, observed that when the dose tends to the value that collapse the superconductivity, $\acute{a}$ grows until reaching a maximum and below starts an abrupt drop; and b) R_0, that would have to change linearly with the number of the induced by the radiation defects at low dose, N_{def}, agreed to the relationship (1) [10], it changes nonlinearly.

$$R_0(D_{exp}) = R_0(0) + \frac{m_0 \nu_f}{n_e e^2} \bar{\sigma} N_{def}, \qquad (1)$$

were m_0 and e are the mass and electric charge of electron, $\acute{i}_f$ its velocity in the Fermi surface, n_e electron density and $\bar{\sigma}$ is the dispersion cross section of electrons on defects. If the defects induced by the radiation are distributed uniformly in the intragrain volume, then was expected that $R_0(D_{exp})$ had a linear dependence at low dose. We observe, however, that $R_0(D_{exp})$ only it is linear when $D_{exp} \longrightarrow 0$.

From a) and b), is concluded that the defects are not distributed uniformly inside the intragrain volume; they should concentrated presumably in the grain boundary regions. In this way, while the dose increases, grow the regions with high defects concentration that weaken the intergrain links, modulating the behavior of the electrical conductivity in the normal state and the J_c of the superconductor.

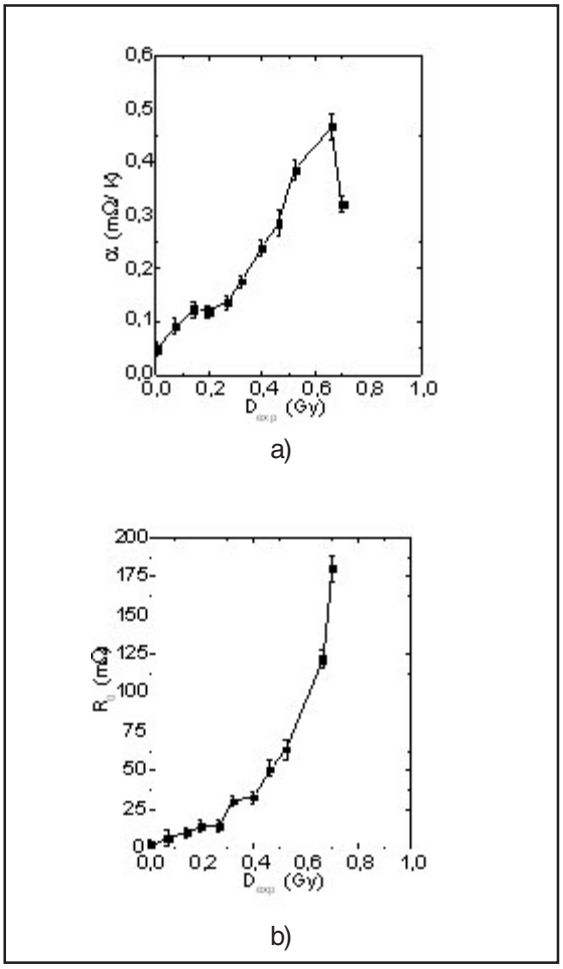

Figure 3. Dependence of α (a) and R_0 (b) with the exposition dose. The curves are to guide the eye.

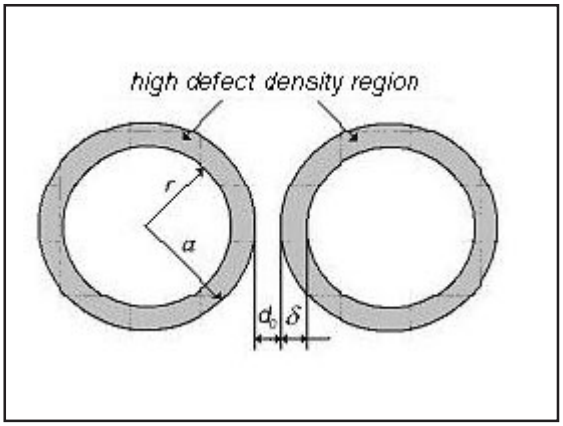

Figure 4. Schematic of two adjacent spherical grains.

The $\alpha(D_{exp})$ behavior is a symptom of the possible occurrence of a metal-semiconductor transition induced by the ^{57}Co gamma radiation in the R(T) behavior.These experimental evidences induce us to formulate a model that explained the observed phenomenon through the probable intensification of the diffusive movements of the defects in the superconducting grains stimulated by the gamma radiation.

In the figure 4 has been represented the structure of a weak link between two adjacent spherical grains of a mean radio *a*, where the thickness d of the junction is determined by the expression:

$$d = d_0 + 2\delta\,, \tag{2}$$

where d_0 is the separation space between the superconducting grains, and δ is the width of the zone with high defects density, fundamentally of oxygen, nearby to the grains boundary (NGB).
It has been supposed that the variations of d with the irradiation time are a consequence of the $\ddot{a}$ increment (d_0 is considered constant) due an intensification of the defects diffusion from the ZFC to the core of the grains stimulated by transportation of the gamma radiation in the superconducting material.

For the description of this process started from the linear diffusion equation of the defects density $n_D(\vec{x},t)$ in presence of a constant and uniform defects production rate G_D inside of each grain, given by the expression:

$$\frac{\partial n_D}{\partial t} = \vec{\nabla}\cdot(D^{\circ}\cdot\vec{\nabla}n_D(\vec{x},t)) + G_D\,, \tag{3}$$

where D° is the diffusion constant of the defects stimulated by the gamma radiation, with the boundary condition:

$$\frac{\partial n_D(r=a,\vartheta,\varphi,t)}{\partial r} = 0\,, \tag{4}$$

In (4) has been neglected the intergrain defects flux with respect to the intragrain.
The initial condition is:

$$n_D(r,0) = n_0(r,\delta_\circ) = \frac{2n_f}{\sqrt{2\pi}}\exp\left[-\frac{1}{2}\left(\frac{r-a}{\delta_\circ}\right)^2\right]$$

$$\text{and}\quad \frac{\delta_\circ}{a} \ll 1 \tag{5}$$

where $\ddot{a}_o$ was taken as a measure of the NBG thickness and it is equal to the quadratic radial dispersion of the defects density with respect to a, and is the mean defects density.

The solution of the problem is obtained using the Variables Separation Method, taking into account that $\ddot{a}_o$<<a:

$$\frac{n_D(r,t)}{n_f} = \frac{\delta_0}{\delta(t)}\left[\frac{n_0(r,\delta(t))}{n_f}\right] + \left[\frac{G_D t}{n_f} + \frac{3(\delta_\circ - \delta(t))}{a}\right], \tag{6}$$

where,

$$\delta^2(t) = \delta_\circ^{\,2} + D^{\circ}\cdot t \tag{7}$$

In (6), we have: $\frac{G_D t}{n_f} << 1$, because the defects density induced by the gamma radiation in the measurement time interval *t* is very small, given the few variation of the material intrinsic properties, as is reported in [11]. Taking this and the condition (5) in account, results that the main term in the right side of the equation (6) is the firs one, therefore the calculation of the quadratic dispersion of the *r* with respect to a is just $\ddot{a}$(t), given the gaussian character of $n_0(r,\delta(t))$ (the coefficient $\frac{\delta_\circ}{\delta(t)}$ does not depend of *r*). Due this, the thickness $\ddot{a}$ after an irradiation time *t* will be $\ddot{a}(t)$. According to the expression (7), $\ddot{a}^2(t)$ increases during the irradiation process as $D^0.t$, a typical Einstein's parabolic behavior for diffusive processes [12]. As conclusion of the preceding study, the variation with the irradiation time of the weak link thickness is expressed by:

$$d(t) = d_o + 2\sqrt{\delta_\circ^{\,2} + D^{\circ}\cdot t} \tag{8}$$

To evaluate the proposed model, were taken the reported values in [11] of the $d(t)$ (figure 5), obtained form the J_c measurements through the application of the Chen model [13]. The samples were irradiated with a ^{57}Co source at room temperature as is described in [11].

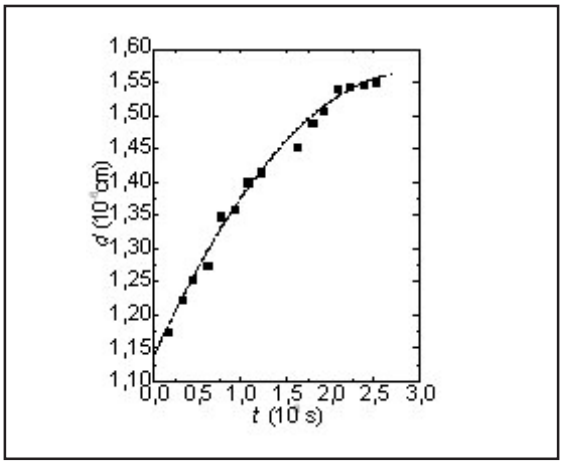

Figure 5. Fitting of the $d(t)$ dependence using the diffusive model.

The fitting of the $d(t)$ data through the expression (4) has been represented with a continuous line in figure 6. The calculated diffusion constant $D^0 = (2.5 \pm 1.5) \times 10^{-20}$ cm^{2}s^{-1} and $d_0 = (0.86 \pm 0.60) \times 10^{-6}$ cm. Though the relative errors are high, the values calculated for both variables are within the correct orders of corresponding magnitude. In particular the value of D^0 is within the variation limits of the constant that characterizes the diffusion processes of impurities and interstitial substitutions in solid materials.

In [8] was reported the dependence of the intracrystalline diffusion constant with the temperature for the oxygen in YBCO samples, given by the expression:

$$D(T) = 1.80 \cdot 10^{-1} \exp(-1.23 \cdot eV / kT) \quad (9)$$

Evaluating this expression at room temperature obtain for the oxygen diffusion constant $D(300\ K) = 0.95 \times 10^{-25}$ cm^{2}s^{-1}. This value is smallest in five orders than D^0, and it is a result of the stimulation effect on the diffusion induced by the gamma radiation on this material. If we assumed for D^0 a behavior with the temperature [14,15] similar to expressed by the equation (9):

$$D^{\circ}(T) = D^{\circ}_0 \exp(-E^{\circ}_a / kT), \quad (10)$$

and compare both values, it is clear, that the increase in five orders of D^0 with respect to D at room temperature only is possible due to a drastic decrease of the activation energy ΔE_a as result of the presence in the material of the secondary electrons created by photons through the Compton interactions and photoeffect mechanism. These electrons upon abandoning their more stable energetic positions in the crystal can provoke the weakening of the interatomic bonds making more probable the oxygen atoms migration to neighboring more stable crystallographic positions.

ACKNOWLEDGEMENTS

This study was supported by the Nuclear Energy and Advanced Technologies Agency of the Ministry of Science, Technology and Environment of Cuba through the project PRN/7-2/1.

CONCLUSIONS

A high non-homogeneity in the deposited energy distribution and therefore in the distribution of the generated defects, mainly oxygen vacancy, was observed in the gamma irradiated YBCO samples, depending their profile of the incident gamma energy and other experimental factors.

The defects are not distributed uniformly inside the intragrain volume; they should concentrate in the grain boundary regions. When the gamma exposition dose increases, grow the regions with high defects concentration that weaken the intergrain links. Evidences of an enhanced diffusive motion of oxygen vacancies process assisted by ^{57}Co gamma radiation on YBCO ceramic samples were found. The behavior of the junction thickness d with irradiation time was well described; particularly, a parabolic diffusion like dependence of the width of the grain boundary regions with the irradiation time was proved.

REFERENCES

[1] CAVA A., BATLOG B., CHEN C. H., Phys. Rev. B, 36 (1987)5719-5722.
[2] TINKHAM, M., Helv. Phys. Acta, 61, 4(1988)443-446.
[3] NELSON, W. R., HIRAYAMA, H., ROGER, D.W.O. SLAC Rep.265, Stanford Linear Accelerator Center. Stanford, California, 1985.
[4] www.ehssun.lbl.gov/egs/egs.html.
[5] Monte Carlo N-Particle Transport Code System, RSICC Computer Code Collection, contributed by Los Alamos National Laboratory, New México, 2001.
[6] EVANS, R. D., The Atomic Nucleus, Published by McGraw-Hill, New York, 1955.
[7] www.physics.nist.gov/PhysRefData/Star/ Text/Estar.html
[8] LEYVA, A., ALFONSO, O., CRUZ, C., Nucl. Inst. Meth. B, 174 (2001)222-224.
[9] KITTEL, C., Introducción a la Física del estado Sólido, 2da edición, publicado por Reverté S. A, Madrid, 1965.
[10] TROFIMSHUK, E.I., TURSUNOV, I.E., Aplicación del método de la electroresistencia en la metalografía radiacional, IAE-4991/11, Moscú, 1990.
[11] MORA, M., CRUZ, C., LEYVA, A., SANDÍN, J. C. Y, QUESADA D., Nucleus, 18 (1995)21-24.
[12] BOKSHTEIN, B. S., Difusión en Metales, Editorial Mir, Moscú, Capítulo 2, 44, 1978.
[13] CHEN, L., ZHANG ,Y. H., J. Appl. Phys., 66 (1989) 186.
[14] KITTEL, Ch., Introduction to Solid State Physics, 4th Edition, Edición Revolucionaria, Instituto Cubano del Libro, Chaper, 19, 1972.
[15] SCHULZE, G.E.R., Metallphysik, Akademie-Verlag, Berlin, 1974.

Received: December 16, 2003
Accepted: February 4, 2004

A MONTE CARLO INVESTIGATION OF SATURATION THICKNESS AND ATTENUATION COEFFICIENT FOR BACKSCATTERED AND TRANSMITTED ELECTRONS OF CONTINUUM SPECTRUM

Arian Abrahantes Quintana, Rafael Díaz Valdés

Centro de Aplicaciones Tecnológicas y Desarrollo Nuclear (CEADEN), Calle 30 No. 502 e/ 5ta Ave. y 7ma, Playa, Ciudad de La Habana, Cuba
arian@ceaden.edu.cu, rdiaz@ceaden.edu.cu

INVESTIGACIÓN POR EL MÉTODO DE MONTE CARLO DEL ESPESOR DE SATURACIÓN Y COEFICIENTE DE ATENUACIÓN PARA ELECTRONES RETRODISPERSADOS Y TRANSMITIDOS DE ESPECTRO CONTINUO

Resumen

La literatura no dispone de datos confiables sobre la retrodispersión de electrones en diferentes medios, sobre todo para los electrones de espectro continuo. Los parámetros de materiales que dependen o podrían inferirse de esos datos podrían presentar ciertas incertidumbres. En 1978, K. K. Sharma y M. Singh determinaron el valor del espesor de saturación para los electrones retrodispersados y el coeficiente de atenuación en algunos metales para las fuentes de radisótopos de $^{90}Sr/^{90}Y$ y ^{204}Tl en un montaje experimental particular. En este trabajo se calcularon nuevos valores de esos parámetros mediante la transportación de electrones en materiales diferentes según el método de Monte Carlo. Se encontró que el espesor de saturación dependía del número atómico del material y se propuso una explicación para interpretar el comportamiento obtenido. Además, los resultados del coeficiente de atenuación y el espesor de saturación diferían de los reportados por Sharma. También se mencionan consideraciones sobre la relación empírica de Sharma para la intensidad de las partículas beta retrodispersadas.

Abstract

Reliable data on electron backscattering in different media are not available in literature, even more for electrons of continuum spectrum. Material's parameters which depend or could be inferred from those data might have some uncertainties. Back in 1978, K. K. Sharma and M. Singh determined the value of saturation thickness for backscattered electrons and attenuation coefficient in some metals for radioisotopical sources of $^{90}Sr/^{90}Y$ and ^{204}Tl in a particular experimental set up. In this work, new values of those parameters were calculated by Monte Carlo transport of electrons in different materials. The saturation thickness was found to be dependent of the material atomic number and an explanation was proposed to interpret the obtained behavior. Furthermore, results of attenuation coefficient and the saturation thickness differred from those reported by Sharma. It is also mentioned a consideration to Sharma's empirical relation for backscattered intensity of beta particles.

Key words: Monte Carlo method, attenuation, backscattering transmission, strontium 90

INTRODUCTION

Determination of material's parameters have some simple methodologies. First, a theory is built up then parameters are evaluated theoretically. An experiment is designed to compare those evaluations with real materials and the approach might be proved. The experiment must fulfill the conditions of good geometry and the necessary corrections to obtain reliable parameter's values. Scientists also collect experimental data and propose quasi theoretical solutions to fit them. On the other hand, calculation power achieved by modern computers have allowed researchers to change those methods.

Researchers have taken advantages of the fact that many interactions in Nature, including interactions of nuclear particles with materials and its constituents, has been fairly well described by many theories. They have gathered in powerful codes the best theories to know the behaviour of particles in presence of different materials. Electrons haven't escaped due to its importance in areas as different as microscopy, nuclear physics or solid state physics. Electrons backscattering have been extensively studied in an experimental or theoretical way but, a consistent theory hasn't been found yet. Everhart [1] proposed a simple theory to explain the behaviour of backscattered

electrons of low energies based on a single elastic scatter collision assumption. Also Archard [2] developed a theory based on the complete diffusion of electrons.

The backscattering process may be achieve by a single collision event with a nucleus with an abrupt change in electron's direction or a multiple collision process. Due to the wide range Coulomb's force, multiple collision events provoke a small deflection on the electron trajectory. The average of the square electron's deviations, $\langle \Theta^2 \rangle$, because of multiple scattering, is proportional to material's density and square atomic number. Deviations are also inversely proportional to the fourth potency of kinetic energy of the impinging electron,

$$\langle \Theta^2 \rangle \propto \frac{dZ^2}{T^4} \qquad (1)$$

Many studies have shown the existence of certain saturation depth of the backscatter intensity. This parameter was defined by Everhart [1] as the ratio number of backscattered electrons from a thick flat target to the number of incident electrons. Sharma [3] determined it experimentally for radioisotopical sources (i.e. continuum spectrum).

Sharma's experiment consisted in *a* ring-type source of radius a, surrounding an end-window Geiger-Muller detector of radius *d*. Targets of radius *b* were positioned at a distance *c* from the center of the source and at a distance e from the center of the detector in an axially symmetric geometry. Frujinoiu [4] have calculated backscattered fraction and saturation thickness for mono-energetic electron beam using MCNP in a geometry like the one modeled in this work.

In Sharma's paper [3] was derived a theoretical relation (expression 2) to describe the behaviour of backscattered intensity as function of thickness,

$$I = \frac{Z^n t}{A} \exp(-\Sigma t) \qquad (2)$$

where: *I*, backscattered intensity; *C*, energy and geometry factor for every source-to-sample and sample-to-detector configuration; *Z*, atomic number; *n*, backscattering index; *A*, mass number; *t*, sample thickness and Ó, attenuation coefficient of the sample.

The energy and geometry factor was written as:

$$C = \iint \Phi(E_0) \left(\frac{\Omega_s}{4\pi}\right) \left(\frac{d\sigma_\beta}{dE}\right) N_0 \left(\frac{\Omega_d}{4\pi}\right) \varepsilon(E) dE dE_0 \qquad (3)$$

where: $\Phi(E_0)$, spectral distribution of the source $(d\acute{o}_\beta/dE)$, cross section for backscattering of an electron of initial energy (E_0) and final energy *E* from a target of hydrogen *Z=1; ε=(E)*; detector efficiency; N_0, Avogadro's number; $\dot{U}/4\eth$, geometry factor corresponding to source-to-sample *(s)* and sample-to-detector *(d)* effective solid angle. Mathematical expressions for geometry factors [5] didn't consider the attenuation of electrons in air. They were written as:

$$\frac{\Omega_s}{4\pi} = 0.5\left[1 - \left(1 + \frac{b^2}{c^2\left(1 + a^2/c^2\right)}\right)^{-1/2}\right]$$

$$\frac{\Omega_d}{4\pi} = 0.5\left[1 - \frac{1}{(1+\xi)^{1/2}} - \frac{3\xi\gamma}{8(1+\xi)^{3/2}} + \gamma^2\left(\frac{5\xi}{16(1+\xi)^{3/2}} - \frac{35\xi^2}{64(1+\xi)^{5/2}}\right)\right] \qquad (4)$$

where: $\hat{\imath} = d^2/e^2$ and $\tilde{a} = b^2/e^2$. Values of geometry factor reported were $\dot{U}_s/4\eth$ times $\dot{U}_d/4\eth$

Attenuation coefficient is also reported in literature. It is important in shielding calculations and dosimetry in general. Attenuation coefficient of a specific material was defined as:

$$\Sigma = N\sigma/\rho \qquad (5)$$

where: *N*, atom density of the material; ρ, mass density and σ, cross section of every process undergone by any particle interacting with the material. Experimental works have concluded this parameter slightly depend with atomic number when continuum spectrum is involved. This is a general behavior assumed in literature and it has been proved in a different sort of experiment.

The aim of this work was a Monte Carlo's approach to electron's backscattering of continuum spectrum. Due to the lack of data referred to this area, Monte Carlo simulations were used in this work to compare values of saturation thickness and attenuation coefficient reported in literature. That's why backscattered and transmitted probability were characterized as function of scatterer's thickness.

METHODS AND MATERIALS

Among Monte Carlo codes, MCNP is a powerful and versatile program that has long been used to transport photons, neutrons and electrons as well. MCNP version 4C [6] contains a number of enhancement that make the code particularly well suited to transport electrons between 1 keV and 1 GeV.

The input file used a cylindrical slab of 10 cm radius. The slab's depth depended on the value of the range of electrons at the specific material. Range of beta particles was calculated by [7]:

$$R_{Al} \approx 110\left(\sqrt{1 + 22.4E_m^2} - 1\right) \quad [mg/cm^2]$$

$$0.2 < E_m < 5\,MeV$$

$$R_X = R_{Al}\frac{(Z/A)_{Al}}{(Z/A)_X} \qquad (6)$$

where: R_{AL} range of beta particles in aluminium with maximum energy E_m in MeV units; R, range of beta particles with maximum energy E_m in MeV units and X, element of interest. This slab was divided in cells, normally on the electron beam direction, which depended on the material, too. As this was kept in mind, the running time was minimized. A fine description of the curves of backscattering and transmitting electrons versus thickness was also achieved. To obtain materials of different thicknesses, each of these cells were filled with either a void or a material like those reported in table 1. Columns 5 and 6 show cell dimensions for every material.

Surface source of 5 cm radius of parallel beam of continuum spectrum was used. Two spectra were evaluated: $^{90}Sr/^{90}Y$ and ^{204}Tl. The spectral distributions were calculated with a Fortran code which made use of Feister results [10] in numerical evaluation of the Fermi beta-distribution function. The thallium spectrum was a straight calculation but strontium-yttrium spectrum was a combination of two spectra.

Tallies were defined as the number of electron that crosses the incident surface at an angle larger than 90° (i.e. backscattered) with respect to the original direction of the beam and those crossing the rear surface (i.e transmitted). The backscatter and transmit probability were obtained for every thickness of each material. Tallies' results were recorded with relative errors lesser than 1 % in every calculation.

RESULTS

Table 2 gives a comparison of the target thickness for which backscattered fraction becomes maximum. There are differences between Sharma's results and the calculated ones. These disagreement was imputed to the fact that Sharma's experimental arrangement didn't obey good geometry conditions to determine saturation thickness. These conditions were achieved by the simulated experiment because it was scored every backscattered or transmitted particle. Also theoretical corrections, expression 4, may be incomplete. For instance, corrections to absorption of electrons in air either in their source-sample or sample-detector pathway should be included.

At materials with effective atomic number less than 6 calculated results showed differences on values of saturation thickness in about a 30%. These behavior was found for both sources which disagree with Sharma's results, too. He concluded an independence between atomic number and the saturation backscattering intensity [5].

An explanation may be account assuming that: deviations of electrons of the impinging direction are ruled by expression 1 and saturation depth must be set by high energies electrons of the spectrum. Therefore, in materials with low mass density and atomic number, high energies electrons have a straight path throughout the material. It means larger, less deflected and smooth trajectories of the impinging electrons. So, the electrons which directly contribute to saturated backscattering intensity will be those created in the material (secondary electrons) and less energetics electrons of the spectrum. So, saturation thickness is reached before the expected value.

In materials with larger mass density (greater than 2.0 $g.cm^{-3}$) or atomic number, deviations angles are bigger. Hence, there must be certain probability that electron´s pathway, which reach deeper within the material, have abrupt direction changes and they still will contribute to backscattering fraction. These behavior might explain the saturation depth's increment.

Tables 3 and 4 give a comparison of attenuation coefficient for both beta emitters. They were obtained by plotting the logarithm of transmitted fraction of beta particles versus thickness and fitting a linear regression. The slope of the line is the attenuation coefficient. In the case of $^{90}Sr/^{90}Y$ beta emitters the contribution of 2.28 MeV radiation of ^{90}Y and 0.546 MeV radiation of ^{90}Sr have been separated by extrapolating the contribution of the former to lower energies and then subtracting it from the latter.

Table 1. Material characteristics of simulated targets

Material	Density (g/cm^3)	Z_{eff}	Elemental composition (Weight Fraction)	Cell(μm) $^{90}Sr/^{90}Y$	Cell(μm) ^{204}Tl
$(CH_2)_n$ [a]	0.940	4.84	H 0.144 C 0.856	50	30
WT [b]	1.020	5.85	H 0.081 C 0.672 N 0.024 O 0.199 Cl 0.001 Ca 0.023 [c]	50	30
LiF	2.635	6.82	Li 0.268 F 0.732 [d]	50	30
Al	2.700	13	Al 1	50	30
Cu	8.920	29	Cu 1	20	10
Pb	11.340	82	Pb 1	10	10

a Polyethylene
b 'solid Water'
c See cite [8]
d See cite [9].

Table 2. Comparison of saturation backscattering thickness reported by Sharma and present work

Material	^{204}Tl Reported ($mg.cm^{-2}$)	^{204}Tl Present work ($mg.cm^{-2}$)	^{90}Sr/^{90}Y Reported $mg.cm^{-2}$)	^{90}Sr/^{90}Y Present work ($mg.cm^{-2}$)
$(CH_2)_n$	NR[a]	78 ± 2	NR	211 ± 2
WT	NR	78 ± 1	NR	219 ± 3
LiF	NR	110 ± 4	NR	316 ± 5
Al	50 ± 4[b] 54 ± 4[c]	113 ± 4	190 ±10[d] 195 ±10[e]	324 ± 7
Cu	56 ± 4[b] 54 ± 4[c]	115 ± 5	190 ±10[d] 195 ±10[e]	321 ± 9
Pb	53 ± 4[b] 54 ± 4[c]	113 ± 6	198 ±10[d] 200 ±10[e]	325 ±11

[a] Not Reported. [b] Results with geometry factor of $8.2*10^{-4}$,
[c] Results with geometry factor of $13.7*10^{-4}$,
[d] Results with geometry factor of $16.5*10^{-4}$, [e] Results with geometry factor of $2.0*10^{-4}$

Table 3. Comparison of attenuation coefficient reported by Sharma and present work for ^{204}Tl

Material	Reported $*10^{-2}$ (cm^2mg^{-1})	Present work $*10^{-2}$ (cm^2mg^{-1})
$(CH_2)_n$	NR[a]	2.51 ± 0.02
WT	NR	2.80 ± 0.01
LiF	NR	2.61 ± 0.04
Al	1.7 ± 0.1[b] 1.8 ± 0.1[c]	2.83 ± 0.03
Cu	1.6 ± 0.1[b] 1.5 ± 0.1[c]	3.02 ± 0.02
Pb	2.1 ± 0.1[b] 2.2 ± 0.1[c]	4.07 ± 0.02

[a] Not Reported.
[b] Results with geometry factor of $8.2*10^{-4}$
[c] Results with geometry factor of $13.7*10^{-4}$

Table 4. Comparison of attenuation coefficient reported by Sharma and present work for ^{90}Sr/ ^{90}Y

Material	^{90}Y Reported $*10^{-3}$ (cm^2mg^{-1})	^{90}Y Present work $*10^{-3}$ (cm^2mg^{-1})	^{90}Sr Reported $*10^{-2}$ (cm^2mg^{-1})	^{90}Sr Present work $*10^{-2}$ (cm^2mg^{-1})
$(CH_2)_n$	NR[a]	4.35±0.03	NR	1.24±0.03
WT	NR	4.41±0.06	NR	1.25±0.03
LiF	NR	4.68±0.08	NR	1.15±0.05
Al	5.8±0.2[b] 4.5±0.2[c]	5.61±0.01	4.8±0.2[b] 3.2±0.2[c]	1.15±0.05
Cu	6.5±0.2[b] 4.4±0.2[c]	7.10±0.02	5.5±0.2[b] 3.5±0.2[c]	1.43±0.08
Pb	6.5±0.2[b] 5.1±0.2[c]	9.68±0.02	5.7±0.2[b] 3.6±0.2[c]	2.01±0.08

[a] Not Reported.
[b] Results with geometry factor of $16.5*10^{-4}$
[c] Results with geometry factor of $2.0*10^{-4}$

Values reported by Sharma differ from calculated ones. A comparison with reported values, for instance those reported in [10], for aluminium (25.6 cm^2g^{-1} for ^{204}Tl and 4.7 cm^2g^{-1} for ^{90}Y) agree with results obtained through MCNP in both cases. Sharma's results disagree for ^{204}Tl. Disagreement were also ascribed to good geometry factors as was noticed above. Electron's attenuation coefficient, as calculated ones showed, slightly depend with atomic number but, in accurate shielding calculations, which include many materials, assume a single attenuation coefficient may be erroneous.

CONCLUSIONS

By using MCNP, saturation thickness and attenuation coefficient were obtained for continuum spectra in different materials. Data obtained through MCNP showed differences with reported values. Disagreements were imputed to the fact that good geometry conditions wasn't fulfilled in previous experimental works. So, experimental determination of material's scattering parameters, such as those reviewed in this work, should be handled with care because, later, they will be utilized in dose calculations which might directly harm human health.

Besides, it was found an odd behavior of saturation thickness which contradict literature affirmations. It was proposed an explanation for these result. Calculations and experiments are inprogress to justify our approach.

ACKNOWLEDGEMENTS

Authors wish to thank Jong-Wha Chang for providing us the Fortran code to perform the calculation of beta spectrum for different beta emitters, to Steve Seltzer and Yong-Ki Kim and theirs uninterested help. We thank Guido Martín, Roman Padilla and Juan C. López for their suggestions regarding manuscript preparation.

REFERENCES

[1] EVERHART, T.E., J. Appl. Phys. 31(8)1960.
[2] ARCHARD, G.D., J. Appl. Phys. 32(8)1961.
[3] SHARMA, K.K., SINGH, M., J. Appl. Phys. 50(3)1979.
[4] FRUJINOIU, C , BREY, R.R., Radiat. Prot. Dosim. 97(3)2001.
[5] SHARMA, K.K., SINGH, M., J. Appl. Phys. 51(4)1980.
[6] BRIESMEISTER, J. F., 2000 MCNP: A general Monte Carlo N-particle transport code, Version 4C. RSICC Computer Code Collection (Oak Ridge National Laboratory) Report LA-13709-M.
[7] NEMETS, O.F., HOFMAN YU B., Nuclear Physics Handbook (Naukoba Dumka, Kiev (1975)92 (Russian Edition).
[8] Tissue Substitute in Radiation Dosimetry and Measurements, (Bethesda MD: ICRU Publications) Report 44 ICRU 1990.
[9] ICRU 1984, Radiation Dosimetry: Electron Beams with Energies betwwen 1 and 50 MeV. (Bethesda MD: ICRU Publications) Report 35.
[10] FEISTER, I., Phys. Rev. 78, 1950.

Received: December 16, 2003
Accepted: February 4, 2004

STUDY OF THE GAMMA IRRADIATION EFFECTS ON THE GRAIN BOUNDARY PROPERTIES IN YBCO SUPERCONDUCTORS USING THE AMBEGAOKAR-HALPERIN MODEL

Larisa Curbelo Garea[1], Antonio Leyva Fabelo[2], Carlos Manuel Cruz Inclán[2]

[1]Facultad de Física de la Universidad de La Habana, Vedado, Ciudad de La Habana, Cuba
[2]Centro de Aplicaciones Tecnológicas y Desarrollo Nuclear (CEADEN), Calle 30 No. 502 e/ 5ta Ave. y 7ma, Miramar, Playa, Ciudad de La Habana, Cuba
aleyva@ceaden.edu.cu

ESTUDIO DE LOS EFECTOS DE RADIACIÓN GAMMA EN LAS PROPIEDADES DE LAS FRONTERAS DE LOS GRANOS EN SUPERCONDUCTORES YBCO UTILIZANDO EL MODELO DE AMBEGAOKAR-HALPERIN

Resumen

Se midieron las características de corriente-voltaje en capas gruesas y muestras masivas superconductoras de altas temperaturas críticas de $YBa_2Cu_3O_{7-ä}$ previamente expuestas a diferentes dosis de radiación gamma. Los resultados experimentales se compararon con la predicción realizada utilizando el modelo disipativo de Ambegaokar-Halperin. Se encontró que el A-H ajusta de forma consistente todos los datos experimentales. Se calcularon la corriente crítica y la resistividad eléctrica de las junturas débiles intergranulares a partir de los resultados del ajuste y se relacionaron con la dosis de exposición gamma. Los cambios observados en las propiedades de las junturas débiles intergranulares con la dosis se discuten en el texto.

Abstract

The current-voltage characteristics of several high-temperature superconducting $YBa_2Cu_3O_{7-ä}$ thick films and bulk samples have measured. The experimental results were compared to the prediction of dissipation in superconductors made by the Ambegaokar-Halperin model. Found that the A-H model consistently fit all the data well over the entire range of measured values. The critical current and electrical resistivity of the junction was calculated using the fitting results and related to the gamma exposure dose. The observed changes in the grain boundary properties with the dose were analyzed in the text.

Key words: barium oxides, ceramics, cesium 137, cuprates, depth dose distributions, gamma radiation, high TC superconductors, physical radiation effects, spatial distribution, superconductivity, transition temperature, yttrium oxides

INTRODUCTION

The irradiation of high critical temperature superconducting material (HTS) with ^{60}Co gamma rays let carrying out studies in simulated space conditions [1], where future applications of this advanced material will be target of an aggressive radiational environment. Others fields of HTS technological application as, for example, particle accelerators, nuclear fusion reactors, etc., where gamma ray background is very high, required the more possible complete knowledge about the behavior of such materials under conditions of safe operation [2].

From the theoretical point of view, the gamma rays are very specific generators of point defects in the crystalline lattice, allowing us to accomplish fundamental studies, as those related with the phenomenon of flux pinning.

The irradiation of the superconducting samples and their current-voltage characterization using conventional transport methods, make easy to elucidate the dependence with the dose of important parameters as the transport critical current (J_{ct}) and the transition critical temperature (T_c). If wanted to obtain more specific information, for example, about the gamma induced change on

the properties of intergrain weak links, it is needed then to process mathematically the acquired experimental information. Fitting the current-voltage curves *V(I)* using some of the dissipating models, facilitates to determine parameters as the critical current of the junction and its electrical resistance.

Considering that the majority of HTS applications in the microelectronic field is based on the use of the Josephson effect, that allows the electric current to pass without dissipation through those mentioned weak links, the present work is dedicated, using the dissipative model of Ambegaokar-Halperin [3], to determine the dependence of the more relevant weak link parameters with the gamma exposition dose.

MATERIALS AND METHODS

Thick films (thickness ~ 15 ì m) of $YBa_2Cu_3O_{7-ä}$ (YBCO) grown by spray-pyrolysis on non-textured ZrO_2(Y) substrates [4], and bulk YBCO samples sintered by solid state reaction [5] were appropriately protected from the environmental humidity and irradiated at room temperature with different exposition doses (D_{exp}) in an ^{60}Co Gamma chamber ($E_{ã}$ = 1250 keV) model MPX-ã-25M, with a ã source calibrated to a power dose of 0.101 Gy s^{-1}. The measurement of the *V(I)* curves at two values of applied external magnetic field (H_{ext} = 0 and 100 Oe) were carried out using the four probe method [6] with Ag electric contacts. The obtained *V(I)* curves were fitted to the A-H model by means of the program MATHEMATICA [7] using the Levenberg-Marquart method [8]. According to A-H model, the dependence of the voltage of the junction V_j with the current I_j is expressed by means of the equation:

$$V(\alpha,\gamma) = \frac{2}{\gamma} R I_{cj} \frac{\exp(\pi\gamma\alpha)-1}{\exp(\pi\gamma\alpha)} \left[\int_0^{2\pi} I_0(\gamma \sin\frac{\theta}{2}) \exp(-\frac{\gamma}{2}\alpha\theta) d\theta \right]^{-1} \quad (1)$$

where R_j is the electric resistance of the junction, I_{cj} its critical current, Io is the modified function of Bessel, á= I_c/I and ã is the effective noise parameter. The equation (1) can also be expressed in the following form:

$$\eta(\alpha,\gamma) = \frac{V_j}{R I_{cj}}, \quad (2)$$

On the base of the simple weak link model and considering that the voltage-current dependence in the sample can be approached to the *V(I)* dependence in a simple junction, in [9] authors determine the voltage drop in the whole sample *V* for a polarization current *I* as:

$$V(I,\gamma) = \frac{L_1}{d} V_j \left(\frac{I d^2}{L_2 L_3}, \gamma \right) \quad (3)$$

Where L_1 is the longitudinal dimension of the sample, L_2 and L_3 the transversal dimensions and d is the media distance between two junctions, which participate in the transport process. Introducing (2) in (3) the next equation is obtained:

$$V(I,\gamma) = a\eta(bI,\gamma) \quad (4)$$

Where a, b and ã are parameters related with the *V(I)* characteristic through:

$$a = \frac{L_1}{d} R_j I_{cj}, \quad (5)$$

$$b = \frac{d^2}{L_2 L_3 I_{cj}}, \quad (6)$$

$$\gamma = \frac{\hbar I_{cj}}{e k_B T}, \quad (7)$$

The equation (4) is used in order to fit the current-voltage curves according to the model A-H, taking a, b and ã as the fitting parameters. From these parameters using equations (5-7) the values of R_j and I_{cj} were calculated.

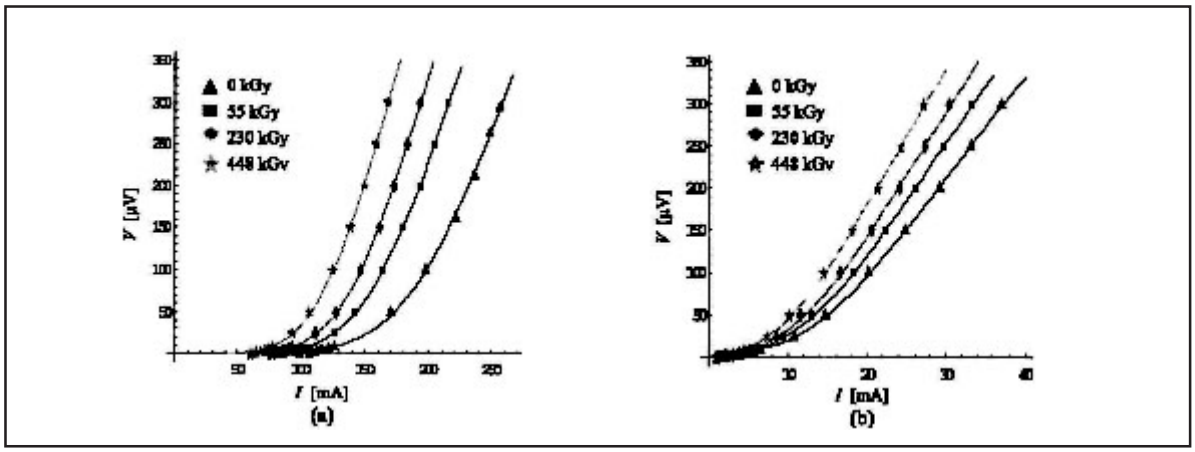

Figure 1. Current-voltage curves of YBCO thick film irradiated with ^{60}Co at different D_{exp} and H_{ext} = 0 Oe (a) and H_{ext} = 100 Oe (b). Continuous lines show the fit from A-H model.

RESULTS AND DISCUSSION

The figures 1 (a) and (b) show the current-voltage experimental curves for different values of D_{exp} of one of the studied thick films, measured in absence of external magnetic field and when it is 100 Oe.

In these two figures is observed, that with the increment of the D_{exp} the V*(I)* curves move to the left, evidencing the monotonous decreasing of the transport critical current. At the same time, the curves slopes increase, and this suggests the existence of a material degradation process stimulated by the gamma rays, which take place inside the superconducting grains and as well as in the weak link regions. This process is not very strong if we keep in mind that the changes in the slopes are not significant. In figures 1 (a) and (b) with continuous lines are presented the theoretical curves obtained as result of fitting the experimental data to the A-H model. The fitting parameters are shown in the tables 1 and 2. As shown, the A-H model describes satisfactorily the experimental data, what is corroborated through the high values that the determination coefficient in all the cases. The figures 2 (a) and (b) show the dependence with the dose of R_j and I_{cj} for the thick films.

With the progress of the irradiation the number of structural defects grows and lead to the increment of the number of scattering centers of the charge carriers. Due this, the electric resistance of the junction increases, just as it is observed in the figure 2 (a), causing the weakening of the Josephson junctions and therefore, the decrease of the I_{cj}, like it is evidenced in the figure 2 (b). With the increment of the number of the dispersion centers, also takes place a process of diffusion of the defects, mainly vacancies of oxygen atoms, from the grain boundaries toward its core [10] producing the increase of the effective junction thickness, phenomenon that also contributes to the degradation of the intergrain links and therefore to the fall of the J_{cj}.

Table 1. A-H model fitting parameters for YBCO thick film at H_{ext} = 0 Oe

D_{exp} (kGy)	a (μV)	Error (%)	b (1/mA)	Error (%)	γ	Error (%)	R^2
0	388.78	11.2	0.007419	3.68	5.60946	4.73	0,99949
55	345.12	8.34	0.009242	2.88	5.673[illegible]	4.07	0,99950
230	337.99	7.56	0.010331	2.59	5.64651	3.74	0,99959
448	330.44	9.96	0.011883	3.44	5.17971	4.36	0,99935

Table2. A-H model fitting parameters for YBCO thick film at H_{ext} = 100 Oe

D_{exp} (kGy)	a (μV)	Error (%)	b (1/mA)	Error (%)	γ	Error (%)	R^2
0	126.405	4.85	0.081120	3.11	2.47887	2.89	0,99972
55	126.336	5.94	0.090324	3.82	2.43144	3.33	0,99959
230	133.940	6.97	0.094761	4.42	2.34994	3.37	0,99952
448	126.96	6.82	0.108929	4.44	2.27005	3.38	0,99954

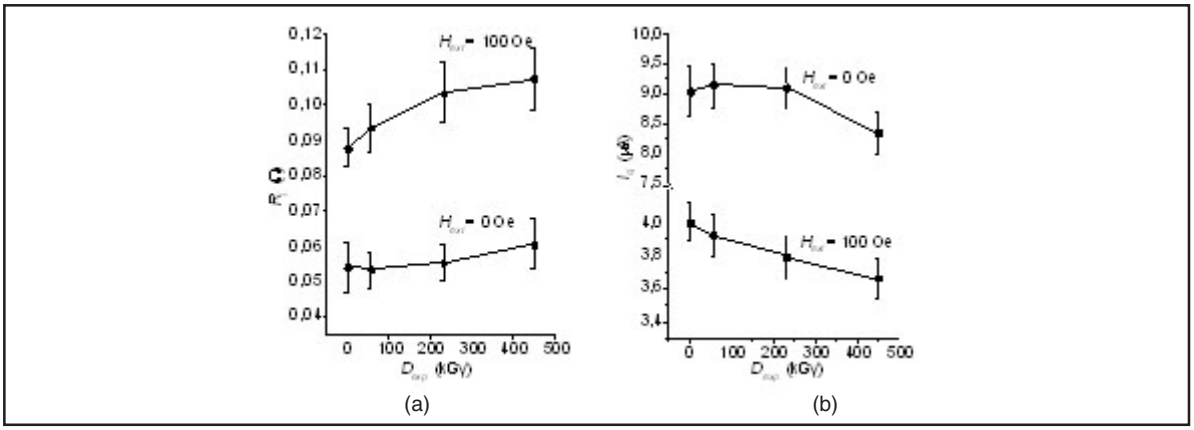

Figure 2. Dependence of the electric resistance (a) and the critical current (b) of the junctions in YBCO thick film irradiated with ^{60}Co at different D_{exp} and H_{ext}.

As it was expected, when the magnetic applied field increases, the parameters that characterize the junctions are depressed. The measurement of *V(I)* in bulk samples of YBCO were only carried out at null values of H_{ext} and the curves obtained for a representative sample at different levels of the D_{exp} are presented in the figure 3.

With the increase of the exposition dose, a similar phenomenon previously observed for thick films, is observed now for bulk samples: the displacement of the curves toward the lower values of current and the increase, now very significant, of their slopes.

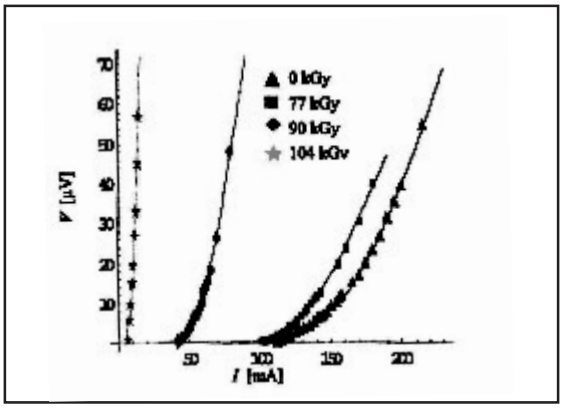

Figure 3. Current-voltage curves of YBCO bulk sample irradiated with ^{60}Co at different D_{exp} and H_{ext} = 0 Oe. Continuous lines show the fit from A-H model.

The degradation of the superconductivity in these samples takes place faster and for smaller gamma exposition dose. For D_{exp} > 110 kGy, the percolate superconductivity totally disappears above the 77 K.

The continuous lines in figure 3 show the theoretical curves obtained from the A-H model fitting of the *V(I)* for the bulk sample. Observe that the model continues describing the experimental results satisfactorily in the whole interval of currents and studied dose.

The table 3 shows the values of the fitting parameters. The coefficient of determination corroborates the quality of the adjustment.

The behavior with the dose of the intergrain junctions parameters in a massive sample calculated from the data of the table 3 is presented in figure 4 (a) and (b). There is appreciated that at the beginning of the irradiation process the junctions transport properties seem be improved, but surpassed 70 kGy takes place a remarked deterioration of the same ones.

This behavior can be related with the gamma radiation ability, at low doses, to stimulate some equilibrium ordering of the atoms in the lattice leading to a more uniform distribution of oxygen and vacancies in the Cu-O basal planes. As result of this reordering is observed an enhancement

Table 3. A-H model fitting parameters for YBCO bulk sample at H_{ext} = 0 Oe

D_{exp} (kGy)	a (μV)	Error (%)	b (1/mA)	Error (%)	γ	Error (%)	R^2
0	75.9695	8.40	0.00886	2.36	6.5943	3.201	0.9986
77	41.414	8.61	0.01169	2.57	8.2959	5.879	0.9973
90	63.5391	10.60	0.02431	3.20	6.3924	4.782	0.9981
104	123.666	14.25	0.10276	5.19	3.8486	7.909	0.9896

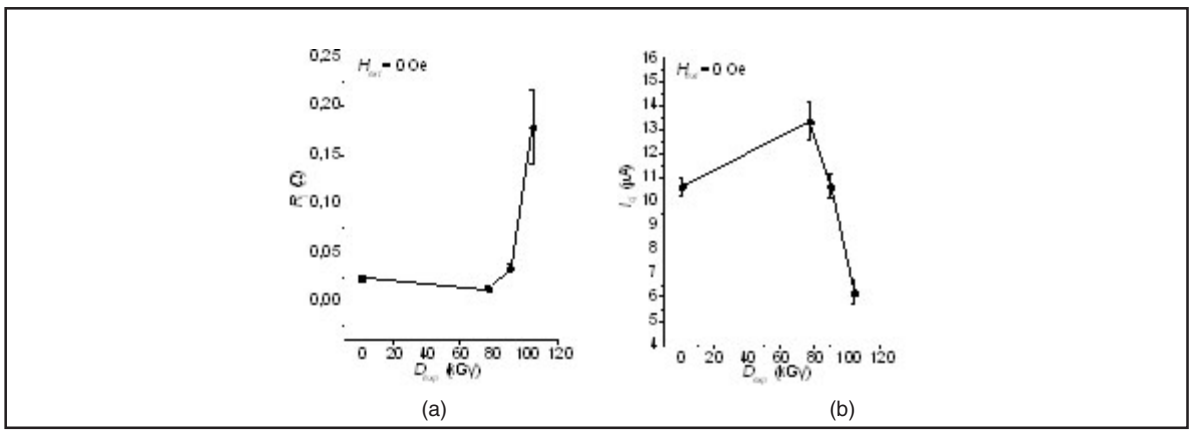

Figure 4. Dependence of the electric resistance (a) and the critical current (b) of the junctions in YBCO bulk samples irradiated with ^{60}Co at different D_{exp} and H_{ext} = 0 Oe.

of the superconducting properties. This phenomenon has been reported in the literature as an intragrain effect [11-13], but the current experiment suggests that a similar process, although more discreet, it can be taking place in the intergrain junction too. Due to the criticality of the weak links, the defects overdoping induced by the gamma rays, produces an immediate deterioration of transportation properties. This takes place when threshold exposition dose is reached, and in our experiment for YBCO bulk samples $D_{exp}^{threshold} \sim 70$ kGy.

Comparing these results with those obtained for the YBCO thick films observes that in the bulk samples the effects the degradation process of the intergrain regions with the exposition dose is higher. It is a consequence of the method of growth and synthesis of the superconducting samples that benefits the film propitiating the formation of intergrain region with smaller defects density, higher intergrain coercion and some preferential grain orientation.

CONCLUSIONS

The Ambegaokar-Halperin dissipative model satisfactorily describes the current transport phenomenon in YBCO superconducting thick films and bulk samples exposed to the ^{60}Co gamma rays. The characteristic parameters that characterized the current transport in the intergrain junction were calculated, observing that, with the increase in the exposition dose they are depressed. For the bulk samples the possible manifestation of the structural reordering stimulated by the gamma radiation below a threshold dose was observed in the weak link regions. The thick films appear more resistant to the gamma irradiation damage than the bulk samples.

ACKNOWLEDGEMENTS

This study was supported by the Nuclear Energy and Advanced Technologies Agency of the Ministry of Science, Technology and Environment of Cuba through the project PRN/7-2/1.

REFERENCES

[1] RITTER, J.C., NISENOFF, M., PRICE, G., WOLF, S.A., IEEE Trans. Magn., 27(1991)2533-2536.
[2] LIU, P. I., "Introduction to Energy and Environment", published by Van Nostrand Reinhold, 1993.
[3] AMBEGAOKAR, V., HALPERIN, B. I., Phys. Rev. Lett., 22(1969)1364.
[4] MORA, M., LEYVA, A., RUBIO, E., PUPO, I. Y LÓPEZ, D., Revista Cubana de Física, 14(1996)111-114.
[5] LEYVA, A., CRUZ, C., ARAGÓN, B., J SUÁREZ,. C. Y MORA, M., Reporte de la Comisión de Energía Atómica de Cuba, CEAC-R, No.1/91(1991)1-11.
[6] SCHRODER, D. K., Semiconductor material and device characterization, publicado por John Wiley & Sons Inc., New York, capítulo I (1990)2-21.
[7] Programa MATHEMATICA v. 4.0, www.wolfram.com and www.mathsource.com
[8] NASH, S. G., SOFER, A., Linear and nonlinear programming, published by McGraw-Hill, New York, 1996.
[9] PUICA, I., POP, I., STIRBET I., CIOBANU, GH., MAZZETTI, P., POPESCU, I., M., Supercond. Sci. Technol., 9(1996)517-522.
[10] CRUZ, C., LEYVA, A., Revista Cubana de Física, 19, No. 2 (2002).
[11] RANCEL, R., GALVÁN, D. H., ADEM, E., F. MORALES, A. LICEA-CLAVERIE, M. B. MAPLE, J. Supercond., 12, 5 (1999)641-648.
[12] ALBISS, B. A., HASAN, M. K., AL-AKHRAS, M. A., AL-OMARI, I., A., SHARIAH, A., SHOBAKI, J., AZEZ, K. A., H. OZKAN, Physica C, 331(2000)297-301.
[13] LEYVA, A., CRUZ, C., M., BOUZA, J., DIEZ, J. C., ANGUREL, L. A., MORA M., Revista Cubana de Física, 19, 1(2002)49-53.

Received: December 16, 2003
Accepted: February 4, 2004

STERILIZATION OF AMNION GRAFTS UNDER CODE OF PRACTICE OF RADIO-STERILIZATION APPLICATION

Isabel Otero Abreu, Lenay Barrera Barroso, Dania Rodríguez Nápoles

Centro de Aplicaciones Tecnológicas y Desarrollo Nuclear (CEADEN)
Calle 30, No. 502 e/ 5ta Ave. y 7ma.
Miramar, Playa, Ciudad de La Habana, Cuba
iotero@ceaden.edu.cu

ESTERILIZACIÓN DE INJERTOS DE AMNION SEGÚN EL CÓDIGO DE PRÁCTICA DE APLICACIÓN DE LA RADIOESTERILIZACIÓN

Resumen

El objetivo del trabajo fue evaluar la aplicación del Código de Práctica en la producción de injertos amnion bajo nuestras condiciones. Este documento describe los requisitos para asegurar las actividades asociadas al proceso de esterilización por radiación. Se muestra la biocarga de diez lotes de amnion, y los resultados de los experimentos de comprobación de la dosis. Esos resultados apoyan la aplicación del Código de Práctica de Radioesterilización para la producción de injertos de amnion.

Abstract

Our objective on this work was evaluating the Code of Practice application on the amnion grafts production under our conditions. This document describes the requirements in order to assure the activities associated with the process of sterilization by radiation. Are showed the bioburden of ten batch of amnion, and the results of the verification dose experiments. Those results support the Code Practice of Radio Sterilization application for the amnion grafts production.

Key words: grafts, legal aspects, licensing regulations, regulations, biological materials, radiosterilization

INTRODUCTION

International standards have been established for the radiation sterilization of health care products include medical devices, medicinal products (pharmaceuticals and biologics) and in vitro diagnostics [1-4]. Following a prolonged and intensive period of study of the effects of ionizing radiation on tissues and their chemical and biochemical components, tissues are now sterilized routinely by ionizing radiation throughout the world using a variety of methods and practices. Through its Radiation and Tissue-Banking Program, the International Atomic Energy Agency has sought during the period 2001-2002 to establish the Code of Practice for the Radiation Sterilization of Biological Tissues and its requirement for validation and routine control of the sterilization of tissues [5].

This Code sets out the requirements of a process that can ensure that the radiation sterilization of tissues always produces standardized sterile products suitable for safe use as allografts. Although the principles adopted here are the same as those used for the sterilization of health care products, there are substantial differences in practice arising from the physical and biological characteristics of tissues.

For health care products, the items for sterilization come usually from large production batches. For example, syringes are uniform in size and have bacterial contamination arising from the production process, usually at low levels. It is the reduction of the bacterial bioburden to acceptable low levels, which is the purpose of the sterilization process, where such levels are defined by the sterility assurance level (SAL). The destruction of microorganisms by physical and chemical means follows an exponential law and so the probability of a surviving microorganism can be calculated if the number and type of microorganisms is known and if the lethality of the sterilization process is also known [6]. Two methods are used in ISO 11137 to establish the radiation doses required achieving low SAL values [7].

MATERIALS AND METHODS

Code of practice for the radiation sterilisation of biological tissues: Requirements for validation and routine control edited by IEAE at 2002. That document gives us the theoretic considerations useful for verification dose and sterilisation dose calculation.

Bioburden recovery

For verification dose establishment is necessary the bioburden recovery as efficiently as possible. Was selected the tissue sample in according the size batch of amnion graft. The sample for bioburden determination was 10 cm^2 in each study batch for this paper, divided on 10 items of 1 cm^2 per one. For bioburden recovering was applied the ISO 11737-I [2].

The experimental work was make in the Microbiology Laboratory of CEADEN following the standard procedures of operation (SPO) in accord with ISO standards and under good laboratory practices.

Each item was immersed in 50 mL of peptone water. The flask was gentile agitated by 10 minutes at room temperature. After that, the liquid was filtrated by nitrocellulose acetate filter with 0.45 μm of diameter. Each filter was washed with 20 mL of distilled water and it was placed over Triptona Soya Agar layer in sterile plate, that were incubated at 35 +/- 2 °C for 48 hours. After incubation time, count colony was make under microscopy Olympus CH-2. 10 replicas were make.

Determination of recovery efficiency

It was carrying out following the same bioburden recovery experiment, with twice extractions after the first wash, under same conditions.
The extraction recovery efficiency was calculated with data of each washes, employed the next mathematical expression (1):

$$E = \frac{A}{A + B + C} \cdot 100$$

Where: A, B, C are bioburden averages after first, second, and third washes.

Bioburden determination of amnion graft

For this objective we used the expression below showed, where some aspects are take account:

$$B = \frac{X \times d \times 100\%}{E \times d_{SIP}}$$

where: B graft bioburden
X SIP bioburden
d graft size
E recovery efficiency
d_{SIP} SIP size (1 cm^2)

Verification dose experiment

The verification dose was calculated using the Code of Practice where we can find the radiation dose required to achieve given SAL for different bioburden having standard distribution of resistance. The verification dose experiment was perform through a sterility test of the samples of amnio tissue was carried out employing Triptona Soya Broth (TSB) in order to detect the presence of aerobic micro-organisms like is recommending at ISO 11737-II [3].

Samples irradiation

There were irradiated 10 cm^2 at the verification dose calculated. It was used a power self-model PX--30 with ^{60}Co sources. The dose rate was of 3.389 kGy/h. The dose mapping of the process and the installation was done using the Fricke dosimeter [8], while for the routine dose mapping was employed Red Perspex dosimeters [9].

RESULTS AND DISCUSSION

Under our interpretation of the Code of Practice, the first step is the bioburden determination of the grafts to radio-sterilize. Is necessary carry out the bioburden determination for two reasons. In first place for the validation of the sterilization process, in order to determine the sterilization dose or verification doses. In addition, the bioburden determination is useful for the routine control of the production process, in terms of the number and nature of the micro-organisms present at the grafts before the sterilization.

The presented work was carried out with 10 samples of 10 batch of amnion graft elaborated at the Technologies Application and Nuclear Development Center (CEADEN). The samples were selected at random and in the quantity indicated in the Code of Practice.

In the table 1 are showed the results obtained in the experiments of bioburden recovering and bioburden estimate from samples of amnion tissue graft.

In each replica of the experiment of bioburden recovering was determined the employed method efficiency, the average was calculated as 88.1%. In our opinion, this step is necessary since the method proposed is based on the quantity and kind of micro-organisms present in the product at the previous stage of the sterilization. For this, the efficiency of the method employed in order to determine the bioburden is important in the obtaining of resulting reliable, then with this fact is possible to specify the results obtained in the calculation of the verification dose.

Table 1. Bioburden recovered and esteemed from samples of amnion grafts

Batch	Recovered bioburden (ufc)	Esteemed bioburden (ufc)
1	1.3	1.5
2	3.3	3.7
3	2.5	2.8
4	1.9	2.1
5	2.1	2.1
6	1.9	2.2
7	3.3	3.7
8	3.9	4.4
9	4.1	4.7
10	2.5	2.8

Table 2. Verification dose calculated and sterilization dose for esteemed bioburden

Bach	Esteemed bioburden (ufc)	Verification dose	Sterilization dose
1	1.5	1.6	14.8
2	3.7	2.2	16.2
3	2.8	2.0	15.8
4	2.1	1.8	15.3
5	2.1	1.9	15.5
6	2.2	1.8	15.3
7	3.7	2.2	16.2
8	4.4	2.3	16.3
9	4.7	2.4	16.5
10	2.8	2.0	15.8

For this kind of processes, is accepted same or higher efficiency at 80%, therefore the results obtained could be considered right and the conditions in those that it was carried out the experiment, adequate.

With the data obtained in the experiment of bioburden recovering and knowing the efficiency of the employed method is possible to determine the bioburden of each batch of grafts. All the data shown in table 1 were calculated by the mathematical expression that we describe above. This mathematical expression takes in to account the relationship between the bioburden of the portion item sample utilized for the experiment, the dimensions of the item. We consider the efficiency of the process employed for the recovered of the bioburden, also that confers a greater precise at the gotten result.

However, keeping in mind that the determination of the bioburden is the principal stage of the effective of the application of the Code of Practice, because forget the efficiency of the recovering of utilized method extraction, could implicate errors in the verification doses determination.

Once calculated the verification dose for each batch, they are carried out the irradiation of the sample of each one of them, applying good practical of irradiation.

The dose applied for the experiment of verification was calculated employing the fact of the esteemed bioburden. The table 2 show them values calculated of verification dose and sterilization dose for each batch was calculated according to the Code of Practice for the Radiation Sterilization of Tissue Allografts.

The experiment of verification dose was carried out pre-setting a level of insurance of the sterility according to the quantity of samples, which implicates that the calculated dose will eliminate the population of micro-organisms with a proportional probability at the SAL, if the same has a standard distribution of resistance. If the result of the sterility test of the graft irradiated at the verification dose show two or fewer positive, the test is accepted.

Once that we has been calculated the verification dose for each batch, it is necessary check the resistance of the polluting population by means of a tests sterility, then this is a rehearsal designed in order to determine if viable forms of micro-organisms are present in the graft.

The sterilization is an example of process in that the efficacy could not be verified for retrospective inspection and tests at the product [10]. The exposition at a validated sterilization process, and carefully controlled, it is not the only associate factor with the provision of guarantee of that the product will be sterile and that it is adequate for the use at the that is destined. Is also very important know the microbiological quality of the product before the irradiation [11].

The sterilization is the process for which all the types of micro-organisms are already eliminated (in terms of their inability in order to reproduce). This implicates that the sterility is defined like an absolute condition, that is to say like a free state of live microorganisms. Therefore are assumed that only it is possible find sterile products or not sterile. However this creates a conflict with the mathematical concepts of the probability of the sterility. According to this, then the sterility is not an absolute condition and for it the better possible

result is that the probability of existence of sterility is acceptably high [12]. Another authors had recommended dose below 25 kGy as sterilization dose for amnion grafts, like us [13].

CONCLUSIONS

The Code of Practice for Radio-sterilization is applicable to amnion production make under our conditions.

The Code of Practice for Radio-sterilization application permitted to reduce the sterilization dose to under 20 kGy for amnion grafts.

ACKNOWLEDGEMENTS

We thank to Dr. Dania Yi from América Arias Maternal Hospital.

REFERENCES

[1] Sterilization of Health Care Products- Requirements for Validation and Routine Control-Radiation Sterilization. ISO 11137, 1995.
[2] Sterilization of Medical Devices- Microbiological methods- Part 1: Estimation of the population of micro-organisms on product, ISO 11737-I 1994.
[3] Sterilization of Medical Devices- Microbiological methods- Part 2: Test of sterility performed in the validation of sterilization process. ISO 11737-II, 1994.
[4] Sterilization of Health Care Products-Radiation Sterilization Dose Small or Infrequent Production Batches. ISO/TR 13409/1996.
[5] Code of Practice for the Radiation Sterilization of Biological Tissues: Requirements for Validation and Routine Control., I.A.E.A (2002).
[6] ARTANDI, C., Microbiological Control Before and After Sterilization: Its Effect on Sterility Assurance. In Experiences in Radiation Sterilization of Medical Products. IAEA 159(1974)3-14.
[7] DE RISIO, J.R., Sterilization Concepts and Methods of Sterilization Employed by the Hospital and Industry. Johnson & Johnson Sterilization Sciences Group Usa, 1992.
[8] PRIETO, F. CHÁVEZ, Influencia de diferentes factores en la calibración de los dosímetros Perpex (Red and Clear). Nucleus 15 (1993)16-19.
[9] PRIETO F., et al., Dosimetría para la puesta en marcha del irradiador de laboratorio PX--30. CIEN-R 10/97, 1997.
[10] BRUCH, W.C., Process control Release of Terminally Sterilized Medical Device. Food and Drug. Administration Silver Spring Marylen, USA, 1991.
[11] ANON, A., Recommendation for the Sterilization of Medical Devises and Surgical Products. European Consideration of Medical Supplier Associate. 84(1984)1-5.
[12] PHILLIPS, G. O., Radiation and Tissue Banking. World Scientific Publishing (2000)315-353.
[13] YUSOF, N., Gamma Irradiation of Tissue Grafts, Proceedings of the 4th International Conference on Biomedical Engineering, Singapore, 7-10 December (1994)49-51.

Received: December 16, 2003
Accepted: February 4, 2004

PHYSICAL-CHEMICAL MODIFICATION OF SODIUN ALGINATE ALGIMAR BY IRRADIATION

Manuel Rapado Paneque[1], Sonia Altanés Valentín[1]
Anselmo Ferrer Hernández[2], Dianelys Sainz Vidal[1], Christine Wandrey[3]

[1]Departamento de Radiobiología
Centro de Aplicaciones Tecnológicas y Desarrollo Nuclear (CEADEN), Calle 30 No. 502 e/ 5ta Ave. y 7ma, Playa, Ciudad de La Habana, Cuba

[2]Departamento de Química Macromolecular,
Centro de Biomateriales, Universidad de La Habana, Cuba

[3]Institute of Chemical and Biological Process Sciences
Swiss Federal Institute of Technology (EPFL)
Lausanne, Switzerland
rapado@ceaden.edu.cu

MODIFICACIÓN FÍSICO-QUÍMICA EN ALGINATO DE SODIO ALGIMAR IRRADIADO

Resumen

El artículo presenta los resultados relacionados con estudios sobre la viscometría, la densitometría y la espectroscopía infrarroja de los efectos inducidos por la radiación gamma en alginato de sodio Algimar. La disminución de la viscosidad intrínseca y la masa molar indican que el cambio principal en la escisión fue el proceso dominante para el sistema irradiado en los estados líquido y sólido. La poca variación en el volumen específico, y los resultados infrarrojos muestran que la degradación en cadena ocurrió sin cambios significativos en la estructura química. Los resultados tienen una implicación práctica en el campo de la radiomodificación y la radioesterilización del alginato de sodio para la formación de microcápsulas.

Abstract

The effect of gamma radiation on the physical-chemical properties of sodium alginate Algimar has been investigated. Dilution viscometry, densitometry, and FTIR spectroscopy served to identify modifications. Decreasing intrinsic viscosities clearly revealed chain cleavage for both solid alginate and alginate in aqueous solution. The invariance of the partial specific volume and infrared results indicate that chain degradation occurs without significant change of the chemical structure. The obtained results have practical implication in the field of radiation modification and sterilization of sodium alginate used for microcapsule formation.

Key words: alginates, capsules, gamma radiation, mechanical properties, radiolysis, radiosterilization

INTRODUCTION

Sodium alginate, a polymer isolated from algae, has found increasingly interest for biomedical applications due to its advantageous, partly unique, properties but also to its low costs. Some of the applications require sterile materials. For this purpose irradiation techniques seem to have advantages since they do not require any additives, which can contaminate the final sterile product with toxic residuals [1]. However, the effect of irradiation on the alginate characteristics has not been described yet concerning its use as material for microcapsule formation. Therefore, the aim of the study presented herein was to identify the influence of the absorbed dose of gamma radiation on the molar mass and chemical structure of the sodium alginate. These parameters are known to affect the network structure of alginate complexes and, as a consequence, the mechanical strength and stability of microcapsules produced from alginate.

MATERIALS AND METHODS

Sodium alginate (Algimar FAC Bach Na-0069) was supplied by the Biomaterial Center of the University of Havana Prior to use all solutions were

filtered (0.22 ì m micron cellulose filter, from Schleicher & Schuell Germany).

Viscometry

The intrinsic viscosity [η], was extrapolated according to Huggins (equ. 1) plotting the reduced viscosity, η_{red}, vs. the polymer concentration, c [2].

$$\eta_{red} = (\eta_{rel} - 1)/c = [\eta] + [\eta]^2 k_H c \quad (1)$$

η_{rel} represents the relative viscosity, the ratio of the flow time of the polymer solution and the solvent. Viscosity measurements were performed in 0.1 M NaCl at 25°C using a capillary viscometer (Viscologic TI 1, SEMA Tech, France).

The viscosity molar mass of sodium alginate was calculated from the Mark-Houwink Sakurada equation [3].

$$[\eta] = KM^{\alpha}_{v} \quad (2)$$

Where K and α are constants. K= 2.0 x 10^{-2} ml/g, and α= 0.83 [4].

Density measurements

The partial specific volumes were calculated from a concentration series of density measurements carried out at 20°C using a Digital Precision Density Meter DMA6OIDMA6O2 (Anton Paar, Graz, Austria).

Infrared spectroscopy

All-were registered using a ATI Mattson Genesis FTIR with a spectral range of 4000-1000 1/cm; employing 10 ì g samples.

Ionizing irradiation of the samples

Alginate samples were irradiated in sealed glass ampoules in vacuum or under oxygen atmosphere in a ^{60}Co gamma source, at the Center of Technological Applications and Nuclear Development (CEADEN), Havana, Cuba. The activity of the radiation chamber was 10 kCi and the dose rate was 3.28 kGy/h, according to Fricke and ceric sulfate dosimetry. The applied doses were in the range of 1 to 100 kGy. Both alginate powder and alginate solutions were irradiated.

RESULTS AND DISCUSSION

The conditions under which irradiation occurs can significantly influence the properties of the final materials. Alterations in the molecular structures of the polymers appear as changes in the chemical or physical properties. Alginate belongs structurally to polysaccharides for wich is known that the irradiation conditions can significantly influence the properties of the final materials [5]. Alterations in the molecular structure of the polymers provoke changes in the chemical or physical properties [6]. The effect of ionizing radiation on the chain length of sodium alginate was viscometrically monitored.

Plots of the intrinsic viscosity as a function of adsorbed doses are presented in figure1.

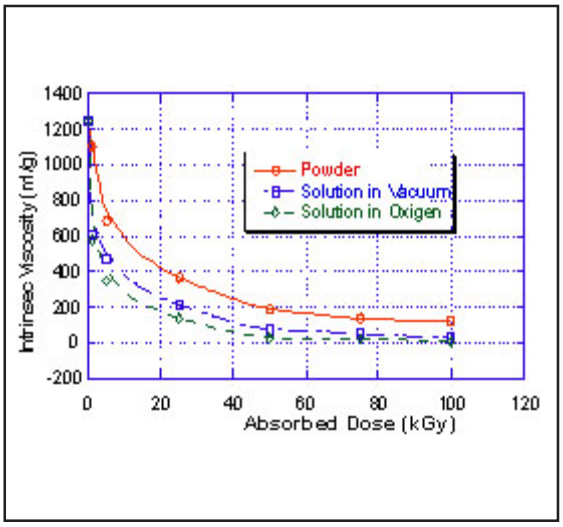

Figure 1. Intrinsic viscosity of sodium alginate as a function of absorbed dose, and influence of the medium conditions.

It is obvious that the system viscosity decreases exponentially if the absorbed radiation dose increases. The distinct decrease of this parameter indicates that main chain scission is the dominating process. These results can be explained by the fact that irradiation of polymers can produce a complex cascade of events such as electron ejection, exited state formation and finally C-C scission [7]. The beneficial effect of decreasing viscosity in the case of formation of small capsules is reported by Stevenson [8], that it facilitates the rate of mass transference of nutrients and cell products. In order to calculate the radiation chemical yields of scission, the number average molar mass Mn was correlated with Mv as follows [9]:

$$\overline{M}n = \overline{M}v\left[(a+1)\sqrt{(a+1)}\right]^{-1/a} \quad (4)$$

for the random distribution. Furthermore, the dose dependence of the number average molar mass was transformed to the coordinates resulting from the statistical theory of radiation cross linking and scission proposed by Charlesby [10] (figure 2).

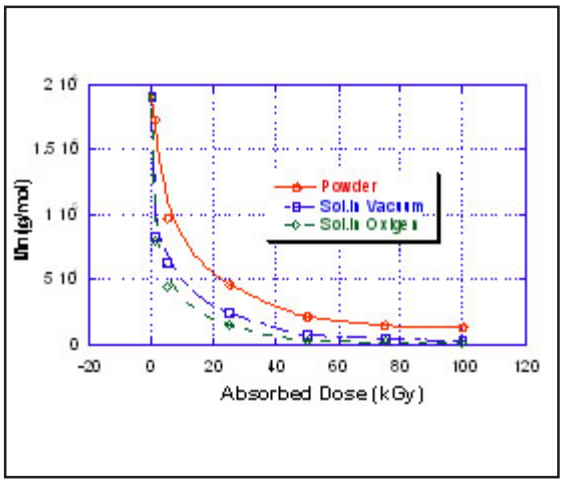

Figure 2. Number average molar mass as a function of absorbed dose and system conditions.

Since one gram of polymer contains Na/ M_n molecules after absorbed dose D and Na/M_{no} at the beginning, one obtains:

$$1/M_n - 1/M_{no} = G(s)D/100\ Na \qquad (5)$$

Where: M_{vo}, M_v denote the number average molar mass before and after irradiation with dose D; G(S) is the radiation chemical yield of scission and Na is Avogadro's number (figure 3).

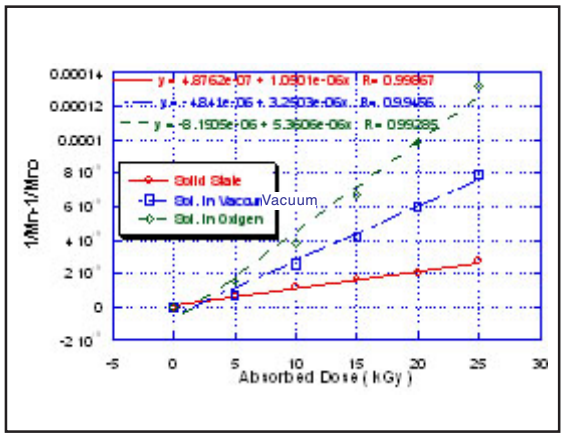

Figure 3. Reciprocal of Number average molar mass, of sodium alginate as a function of absorbed dose and medium conditions.

Radiation yields of scission, calculated from the linear correlation were G_s= 1.1ì mol J^{-1} for the samples irradiated in solid state, G_s= 3,2 ì mol J^{-1} for irradiation in vacuum, and G_s= 5,3 ì mol J^{-1} in oxygen, respectively. These results are in agreement with those reported for other irradiated polysaccharides [11].

Whereas the decrease of the molar mass of sodium alginate with increasing absorbed radiation dose could clearly be demonstrated, the densities measurements did not reveal systematic structural modification (see figures 4,5). The density values scatter within an error of ± 5%.

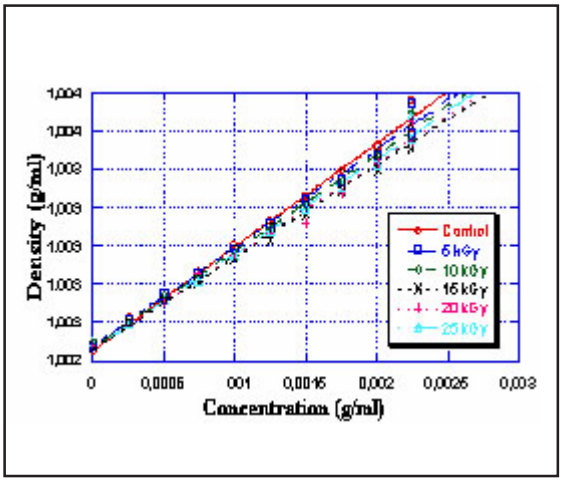

Figure 4. Density of non-irradiated and irradiated sodium alginate, using 0.1 M NaCl as solvent.

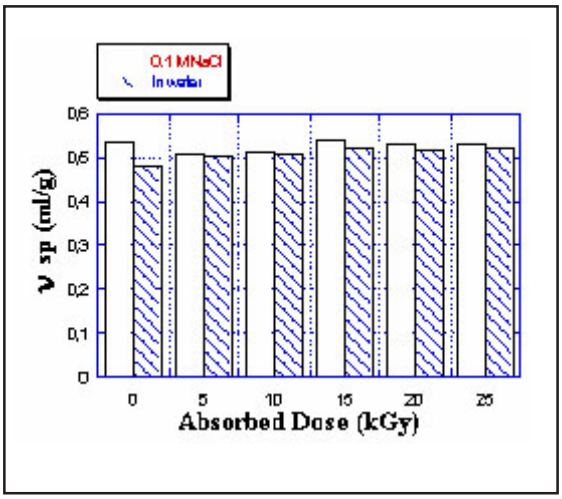

Figure 5. Dependence of the partial specific volume, (n), of sodium alginate on the absorbed dose.

In general, the partial specific volume (ν) of polymers depends on the chemical structure but not on the molar mass if end group effects can be neglected. As figure 5 demonstrates, using the partial specific volume (ν), as a measure for structural change, the system is stable up to absorbed dose of 25 kGy. It should be noticed that the partial specific volume is slightly higher for the sodium alginate in 0.1M NaCl as solvent, than for sodium alginate in water resulting from different solute-solvent interactions. This implies that chain degradation occurs without significant modification of the chemical structure. This interpretation was confirmed by the IR results (see figure 6).

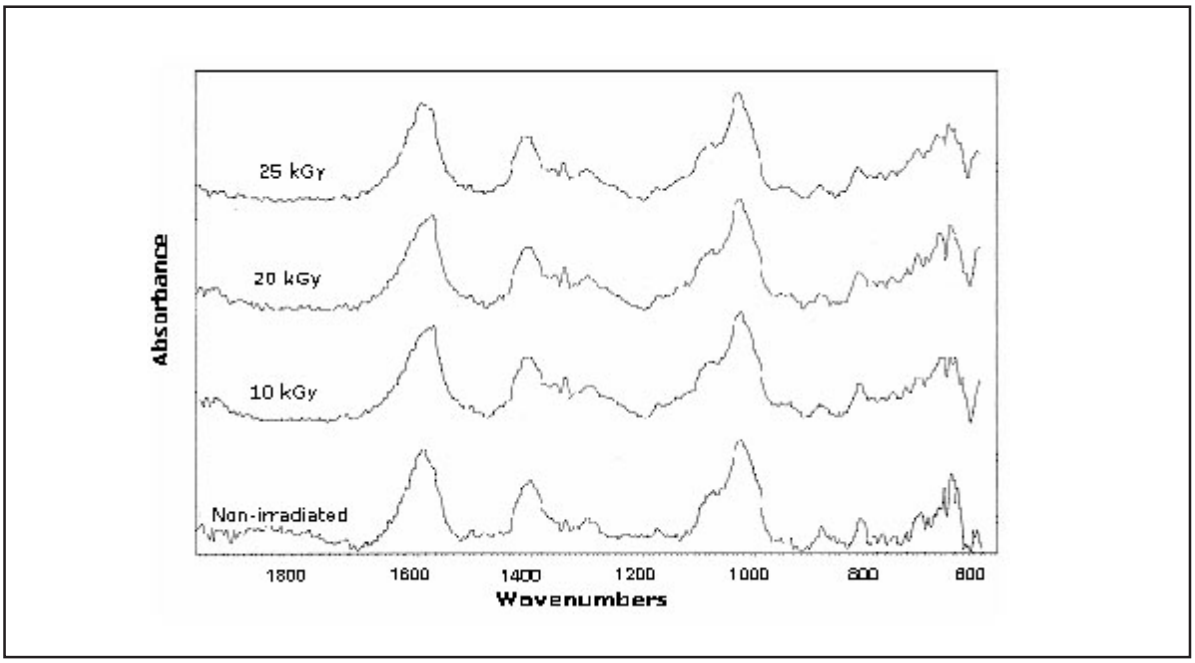

Figure 6. FTIR Spectra of sodium alginate Algimar, irradiated and non-irradiated.

Spectra are sensitive to functional groups for instance carboxylic group of the sodium alginate which shows a characteristic bond at wave number 1404 cm^{-1} as a reference [12].

Comparing all the spectra of the irradiated sodium alginate powder up to adsorbed doses of 25 kGy they do not reveal any significant difference to the spectra of non-irradiated sodium alginate Algimar. That indicates that the chemical structure is not significantly altered by absorption of such a dose.

CONCLUSIONS

Viscometry, densitometry, and FTIR spectroscopy are suited to study the influence of gamma radiation on the stability of sodium alginate. Viscosity measurements quantitatively revealed the extend of chain degradation as a function of the applied radiation dose. Less degradation was identified for the solid material in comparison to alginate in solution. From density measurements in water and NaCl solution, as well as from FTIR spectra, can be concluded that no significant chemical modification occurred for adsorbed doses up to 25 kGy.

The results obtained have a practical impact on the radiation sterilization of sodium alginate in with subsequent utilization for microcapsule formation. It has to be considered that main-chain degradation occurs if a certain radiation dose is exceeded. Moreover, the results of the study support the estimation of the extend of the irradiation influence as a function of the experimental conditions in practical applications.

ACKNOWLEDGEMENTS

We would like to express our thanks to Prof. David Hunkeler for his helpful discussions. The financial support by the budget of the Valorization Cuba Project is gratefully acknowledged as well.

REFERENCES

[1] KOST, J., GOLDBART, R., In: Natural and modified polysaccharides. Biomaterials Forum, London Butterworths scientific Publications17, 13 (1996).
[2] FREEMAN, W.J., Encyclopedia of Polymer Science and Engineering, Vol. 3, Eds, John Wiley & Sons, New York (1985)290.
[3] KURATA, M., TSUNASHIMA, Y., In: Polymer Handbook, Eds., John Wiley & Sons, New York (1989)VII/10.
[4] HEYRAND, A. et al., Physicals Properties of phycolloids In: Introduction to Applied Psychology, Hagere (1990)151.
[5] BOVEY, F.A., The effects of ionising radiation on natural and synthetic high polymers. Interscience Publishers, Inc., New York, 1958.
[6] MUZZARELI, A.A., In : The Polysaccharides, Vol.3, G.O. Aspinall (Ed.) R Academic Press, New York, 1984.
[7] CARLSSON, D.J., CHEMELA, S., Polymers and high-energy irradiation. Elsevier Science Publishers, London (1990)109-113.

[8] STEVENSON, W., SEFTON, M., J. Biomaterials, Vol.8 (1987)449-457.
[9] TABATA, Y., In: CRC Handbook of Radiation Chemistry, CRC Press (1999)743.
[10] ULANSKI, P., ROSIAK J., J. Radiat. Phys. Chem. 39(1) (1999)53-57.
[11] LEO, W.J., McLOUGHLIN, A.J., MALONE, D.M, Biotecchnol. Prog. (1990)6, 51.
[12] SOON-SHIONG, HEINZ, P., et al., Natural and modified polysaccharides Lancet (1998)343.

EFFECT OF THE IRRADIATION TEMPERATURE AND POST-IRRADIATION TIME IN THE RESPONSE OF THE RED 4034 PERSPEX DOSIMETERS

Enrique Fco. Prieto Miranda, Manuel Plasencia Gutiérrez, Gisela Barrera González

Centro de Aplicaciones Tecnológicas y Desarrollo Nuclear (CEADEN)
Calle 30, No. 502 e/ 5ta ave. y 7ma, Playa, Ciudad de La Habana, Cuba
efprieto@ceaden.edu.cu

EFECTO DE LA TEMPERATURA DE IRRADIACIÓN Y EL TIEMPO DE POST-IRRADIACIÓN EN LA RESPUESTA DE LOS DOSÍMETROS RED PERSPEX 4034

Resumen

En el control del proceso de irradiación para el rango de altas dosis uno de los sistemas dosimétricos más empleados como dosímetro de rutina son los Perspex, debido a que es un sistema reproducible, de fácil manipulación y rápida lectura. En este sistema, al igual que en otros, su respuesta está afectada por diferentes factores, los cuales provocan una sobreestimación en el valor de la dosis absorbida si estos no son considerados. En el trabajo se estudió la influencia de la temperatura de irradiación y el tiempo post-irradiación en el valor de la dosis absorbida de los dosímetros Red 4034 Perspex Batch EN, lo cual permitió obtener valores exactos de dosis absorbidas en el control del proceso de irradiación.

Abstract

To control the radiation processing in the high dose range one of the dosimetric systems more employed as routine dosimeters are the Perspex, due that it is a reliable system, of easy manipulation and quick measurement. In this system, at the same as another, the response is affected for several factors, it which produce an overestimation in the absorbed dose value if they are not take account. In the present paper was studied the influence of the irradiation temperature and the post-irradiation time in the absorbed dose value of the Red 4034 Perspex dosimeters Batch EN, it which would allow us to obtain accurate absorbed dose value in the radiation processing control.

Key words: calibration, dosemeters, irradiation, Perspex, temperature monitoring

INTRODUCTION

In the radiation processing control at industrial scale is important provide dosimetric systems present a number of characteristics as are easy handle, quick readout, equivalent absorption at biological tissue and a wide measurement dose range. For these reasons the Red Perspex dosimeters are thoroughly employed as routine dosimeters in the process control.

The first factors studied to know their influence in the response of the Red Perspex dosimeters they were errors in the measurement wavelength, the bandwidth, water content and the dose rate, this last being object of study since the first have been thoroughly standardized [1]. However at present, the factors more studied that affect the dosimetric system response are the dose rate, the irradiation and storage temperatures as well as the post-irradiation time.

On the other hand, it has been found in the literature that exists a light dependence of the response in the temperature range of 20 at 43°C during the irradiation [2-4], the effect of high temperature during the immediate time after the irradiation could produce errors in the estimation of the dose with relation at calibration and storage temperatures of the laboratories, for example at 23°C [4,5].

In dependence of irradiation facility design and the operation procedures, the irradiated dosimeters could remain at elevated temperatures for several hours or days before the measurement. Therefore the conditions found in the practice of the relation temperature/

measurement time could be thoroughly different at the employed in the calibration classical method [6] and in the practical application of these dosimeters the best dosimetric accuracy is to be expected for readings carried out shortly after irradiation, but this is not always possible, in practice, particularly in the case of exchange and intercomparison of dosimeters irradiated at different facilities and in many occasion the operator could not carry out the measurements immediately concluded the irradiation, everything which constitutes possible errors in the measurement of the absorbed dose as a function of the time lapsed before the readout [2].

To take account the studies carried out on the influence of the dose rate, irradiation and storage temperatures and measurement time after the irradiation it is could to point that these affect the response of Red Perspex dosimeters of a combined manner, depending on the determined values for each factor. For this reason in the present paper was studied the influence of the irradiation temperature and the elapsed time before measurement in the response of the Red 4034 Perspex dosimeters Batch EN.

MATERIALS AND METHODS

In order to know the effect of the irradiation temperature in the response of these dosimeters three temperature values were selected, 10, 25 and 29,5°C, due to the last value is the irradiation chamber temperature without cooling system, the value of 25°C corresponds at the temperature with which the most part of products are irradiated and the value of 10°C since many investigations are carried out for this temperature value. The dosimeters were irradiated at dose values of 5 and 25 kGy and dose rate of 2.2 kGy/h, which was determined employing the sulfate ceric dosimeter [7].

In the case of the study to know the effect of elapsed time before measurement the dosimeters were irradiated for dose rate of 5, 15, 25, 40 and 50 kGy, with a dose rate value of 1,28 kGy/ h, with irradiation temperature of 40°C and storage temperature of 30°C and they were measured at 2 hours, 7, 14, 21 and 28 days after irradiation.

All the irradiations were carried out at temperature of 25 ± 1°C in a self-shielding research irradiator, type PX-ã-30, with ^{60}Co sources, it were carried out four replicas for radiation dose in correspondence with the standards of the American Society for Testing and Materials (ASTM) [8], the dosimeters were placed in the center of the inferior part of the irradiation chamber in a lead jacket with polyethylene foam in order to get the electronic equilibrium conditions.

The induced absorbance values (K) by the radiation in the dosimeter were measured in a LKB-Biocrom Ultrospec II 4050 spectrophotometer, for a wavelength value of 640 nm, temperature of 25 ± 1°C and a relative humidity 60%. The thickness (X) of each dosimeter was measured with a micrometer of precision of ± 0,01 mm. The induced specific absorbance value (K*) of each dosimeter was determined for the following expression:

$K^* = K / X\ (cm^{-1})$

RESULTS AND DISCUSSION

Table 1 is shown the K* values obtained for the studied irradiation temperatures and the absorbed doses and in the table 2 the relative errors (Er) values for the different temperatures, where it is observed for the high absorbed dose value and high irradiation temperature values exist significant difference it which does not occur for the minor dose value, it to take account that the uncertainty in the measurement of the induced specific absorbance in the Red Perspex dosimeters is of 2%, it is in agreement with the results found for high temperature values and another batch kind of Red Perspex dosimeters [9-10].

Table 1. K* values for studied irradiation temperatures and absorbed dose

Temperature (°C)	10	25	29.5
Dose (kGy)	K*	K*	K*
5	0.8483	0.8376	0.8570
25	2.6017	2.5964	2.6787

The table 3 shows the K* values obtained for the studied doses and the different times of measurement after the irradiation concluded while in the table 4 is shown the relative errors at 2 hours of measurement with relationship at the other times, where it is observed that until the dose value of 25 kGy and 14 days of measurement there is no significant difference and for last times at this dose value there is significant difference. However for high absorbed dose, 40 and 50 kGy, from the first 7 days of measurement exist significant difference. These results demonstrate the influence of the elapsed time before measurement in the response of this dosimetric system, which are in agreement with they results obtained by Whittaker and Prieto in another kind of Red 4034 Perspex dosimeter Batch [6, 11, 12].

Table 2. Relative error values for different temperatures

Dose (kGy)	Er (%) a 10 °C		Er (%) a 25 °C		Er (%) a 29.5 °C	
	25 °C	29.5 °C	10 °C	29.5 °C	10 °C	25 °C
5	-1.3728	0.9087	1.3919	2.3133	-0.9005	-2.2610
25	-2.5109	2.9584	2.5756	5.6101	-2.0734	-5.3121

Table 3. K* Values for different elapsed times before measurement

Dose (kGy)	K*				
	2 hours	7 days	14 days	21 days	28 days
5	0.079	0.079	0.077	0.073	0.07
15	0.190	0.188	0.187	0.185	0.176
25	0.256	0.253	0.253	0.250	0.242
40	0.330	0.319	0.309	0.283	0.283
50	0.356	0.328	0.302	0.284	0.260

Tabla 4. Relative error values at 2 hours of measurement

Dose (kGy)	Relative error (%) at 2 hours				
	2 hours	7 days	14 days	21 days	28 days
5	0.0000	0.0000	2.5317	7.5819	10.1296
15	0.0000	1.0526	1.5790	2.6316	7.3684
25	0.0000	0.3906	1.1719	2.3438	5.4688
40	0.0000	3.3333	9.0909	14.2424	20.2020
50	0.0000	7.8652	15.1685	20.2247	26.9663

CONCLUSIONS

The response of the Red 4034 Perspex dosimeters Batch EN is sensitive at the variations of the irradiation temperature and the elapsed time before measurement the same as other batch, this effect can be more significant in correspondence at the relation between the absorbed dose values, irradiation temperature and the elapsed time before measurement of the dosimeters, for this reason for their employment in industrial facilities these dosimeters should be calibrate under the same work conditions of the facility in order to avoid a serious overestimation of the absorbed dose value in the radiation processing control.

REFERENCES

[1] WHITTAKER, B., Red Perspex Dosimetry. Manual on Radiation Dosimetry, Marcel Dekker (1970)363-369.
[2] MILLER, A. et al.. Some limitations in the use of plastic and dyed plastic dosimeters, Int. J. Appli. Rad. Isot. 26(1975)611-620.
[3] WHITTAKER, B., et al., Some parameters affecting the radiation response and post-irradiation stability of Red 4034 Perspex dosimeters, Proceeding on High Dose Dosimetry, IAEA, Vienna (1985)293-305.
[4] OLEJNIK, T.A., Red 4034 Perspex dosimeters in industrial radiation sterilization process control, Advances in Radiation Processing, Trans. 2nd. Int. Mtg. Miami, Fl., 1978.Radiat. Phys. Chem. 14(1979)431-447.
[5] BARRET, J.H., Dosimetry with dyed and undyed acrylic plasti, Trends in Radiation Dosimetry. Int. J. Appl. Radiat. Isot. 33(1982)1177-1182.
[6] WHITTAKER, B., WATTS, M.F. The influence of ambient temperature and time on the radiation response of Harwell Red 4034 PMMA dosimetrs. Proc. Symp. On Techniques for high dose dosimetry in industry, agriculture and medicine. IAEA-TECDOC-1070(1999)143-148.
[7] PRIETO, E. FCO., NRIAL, Determination of absorbed dose using the sulfate ceric dosimeter 1992.
[8] ASTM. ISO/ASTM 51276, Practice for Use of a Polymethylmetacrylate Dosimetry System. Prog. Rep. 52, Subcommittee E 10.01 Dosimetry for Radiation Processing, 2002.
[9] WHITTAKER, B., WATTS, M.F., The influence of dose rate, ambient temperature and time on the radiation response of Harwell PMMA dosimeters. Radiat. Phys. Chem. 60(2001)101-110.

[10] AL-SHEIKHLY, M., CHAPPAS, W.J., Effects of absorbed dose rate, irradiation temperature and post-irradiation temperature on the gamma ray response of Red Perspex dosimeters. High Dose Dosimetry for Radiation Processing. Proc. Symp. Vienna, 1990. IAEA. STI/PUB/ 846(1991)419-434.
[11] PRIETO, E.FCO., CHÁVEZ, A., Influence of different factors in the calibration of Perspex dosimeters (Red and Clear). Rev. Nucleus, No. 15(1993)16-19.
[12] VALDEZCO, E.M., et al., Status and prospects of high-dose metrology in the Philippines. High-Dose Dosimetry (Proc. Int. Symp.) IAEA, Vienna (1985)31-46.

Received: December 16, 2003
Accepted: February 4, 2004

CORROSION EVALUATION OF AISI 316L STEEL IN CHLORIDE–PHOSPHATE SOLUTIONS: APPLICATION OF ELECTROCHEMICAL NOISE MEASUREMENT

Victoria Herrera Palma, Pedro Pablo Mayás Villalón
Centro de Aplicaciones Tecnológicas y Desarrollo Nuclear (CEADEN),
Calle 30 No. 502 e/ 5ta Ave. y 7ma, Miramar, Playa, Ciudad de La Habana, Cuba CP 6122
Laboratorio de Materiales Dpto. Análisis y Ensayos
victoria@ceaden.edu.cu

EVALUACIÓN DE LA CORROSIÓN DEL ACERO AISI 316L EN SOLUCIONES CLORURO-FOSFATO: APLICACIÓN DE LA MEDICIÓN ELECTROQUÍMICA DEL RUIDO

Resumen

El objetivo del trabajo fue la utilización del Ruido Electroquímico como herramienta para el diagnóstico del comportamiento del acero inoxidable AISI 316L, expuesto a una solución de cloruro de sodio mezclada con hidrógenofosfato de sodio (Na_2HPO_4) y el dihidrógenofosfato de sodio (NaH_2PO_4). Para este fin se estudia la influencia de la temperatura en el desarrollo de la corrosión por picadura. Se emplean la técnica de Potenciodinámica Convencional y el Análisis del Ruido Electroquímico. Para este último, se comparan resultados de los métodos estadísticos y espectrales de evaluación de señales. No se produce ninguna corrosión por picadura en AISI 316L en la solución estudiada, por lo menos hasta los 120 ºC. En contraste, la falta de estas sales de fosfato en solución de16 g/l de NaCl puede inducir la corrosión por picadura con un subsiguiente desarrollo de moho en la superficie del acero. La Resistencia del Ruido electroquímico R_n, (método estadístico) y la Resistencia del Ruido Espectral R_{sn} (método espectral) se calculan a partir del Potencial y de las Densidades Espectrales de Corriente. Se observa una buena correlación en los resultados.

Abstract

The aim of this paper is the use of the electrochemical noise (EN) as a tool for the diagnosis of the behavior of AISI 316L stainless steel, exposed to a sodium chloride solution mixed with sodium hydrogenphosphate (Na_2HPO_4) and sodium dihydrogenphosphate (NaH_2PO_4).To this purpose the influence of temperature on the development of pitting corrosion is studied.Conventional Potentiodynamic technique and analysis of electrochemical noise signals are used. For this latter, results of statistical and spectral methods of signal evaluation are compared.No pitting corrosion in AISI 316L in the studied solution is developed, at least up to 120 ºC. In contrast, the lack of these phosphate salts in 16 g/l NaCl solution can induce pitting corrosion with a following rust development on steel surface.Electrochemical noise resistance R_n (statistical method) and spectral noise resistance R_{sn} (spectral method) are calculated from the potential and current power spectral densities. A good match is observed.

Key words: gamma spectroscopy, scanning electron microscopy, steels, water chemistry, X-ray fluorescence analysis.

INTRODUCTION

Electrochemical noise has shown some advantages over conventional techniques for evaluating corrosion processes. This technique can be applied without polarization of the probe, not perturbing the ongoing studied event. Therefore, it is being used for monitoring in real time the degradation of industrial components such as water systems, chemical reactors, etc [1].

In laboratory conditions [2,3] electrochemical noise measurements also allow to perform a diagnosis of the material behavior in specific environment conditions. It is well known that austenitic stainless steel is prone to pitting corrosion in chloride solutions. Alloying with Molybdenum enhances sensibly its corrosion resistance. However, even for this material pitting can occur over a critical pitting temperature (CPT) for specific values of chloride concentration and electrochemical potential. Below CPT the material is not damaged.According [4] AISI 316 stainless steel exhibits pitting corrosion over 55 ºC in 0,17M NaCl solution. This concentration has practical interest for some industrial formulations in which phosphate ions are added.On the other hand, there are some references on the passivating

character of phosphates, in spite of their non-oxidating ability. The aim of this paper is the application of Electrochemical noise measurements to analyze the behavior of stainless steel AISI316L in sodium chloride solutions, where sodium hydrogen-diphosphate and hydrogen-monophosphate are added. In spite of the known high corrosion resistance of this material, in practice some pitting events have been observed in industrial systems where such solutions are used.

Conventional polarization techniques and the measurement of electrochemical noise signals are applied. For this last technique results of statistical and spectral analysis are compared.

MATERIALS AND METHODS

Samples with a 1 cm^2 surface were cut from AISI 316L tubes. Elemental composition of steel is specified in table 1. Surface roughness was R_a = 0.25 μm. Pairs of nominally identical electrodes were used for the measurement of electrochemical noise of electrodes voltage and the flowing current between them in a ACM GILL4 Analyzer. Sampling rate was two points per second and the length of the time record was 2048 points. No external polarization was applied to samples.

Table 1. Chemical composition of AISI 316L (weight %)

C	Si	Mo	Mn	Cr	Ni	S	P	Fe
0.016	0.44	2.43	1.55	16.97	13.40	0.0098	0.032	Balance

Time-dependences of noise signals were obtained at 25, 60 and 85°C in chloride-phosphate solution with a composition 16 g/l NaCl + 2.24 g/l Na_2HPO_4 + 2.48 g/l NaH_2PO_4 (pH = 6,4). Heating of the solution was accomplished with submerged electrodes. End temperature was reached in two minutes. At this moment, noise measurements were started. Three replica were used voltage and current noise dependences were analyzed by both statistical and spectral methods [5-7].

According to statistical method, mean current I and potential V, the corresponding standard deviations S_I and S_V where calculated at each selected temperature. For the spectral method, power spectral densities (PSD) were calculated from the time- dependences of potential and voltage fluctuations, applying the fast fourier transformation (FFT). At the same time potentiodynamic polarization dependences were obtained to evaluate the extent of passivity of the steel in the given solution.

Measurements were carried out at 25 and 60°C, in a PS4 electrochemical system and in a ACM GILL8 equipment at a polarization rate 1 mV/s. Finally, samples of AISI 316L were exposed to solution at 120°C during 8 hours in a static miniautoclave with 5 ml volume.

RESULTS

Electrochemical noise

Experimental potential and current time-dependences are shown in figures 1 and 2, respectively.

At 25 and 60ºC the measured replica of potential noise are located in an interval between -200 and +70 mV. At 60 ºC the dependence shows more transient events. At 85ºC potentials are much more negative, between -300 and -450 mV.
In figure 2 the current flowing between the two identical electrodes is shown. Negative or positive values depend on which electrode was activated. A very low current (< 10^{-2} mA/cm^2) is obtained at 25ºC and it is increased with temperature. At 60ºC a high quantity of transients is observed. At 85ºC fewer events are recorded, but the amplitude of fluctuations is higher.

Mean values of current and voltage, their standard deviations and the calculated electrochemical noise resistance R_n are given at each temperature in tables 2 and 3. As it is shown, mean current grows from 3,2 μA/cm^2 at room temperature up to 34,2 μA/cm^2 at 85ºC.

Power spectral densities for potential and current are given in figures 3 and 4, respectively.

Potentiodynamic polarization dependences vs. temperature

Results of polarization curves are given in table 4 and figures 5 and 6. As it is shown, passivity is kept over the studied temperature range. In phosphate solutions for all measured temperature range, corrosion potential shift towards more negative values, relative to their analogous values in NaCl solution, whereas currents are smaller. This difference is diminished with the temperature increment up to 85°C, when anodic current for both environments become similar.

The grow of temperature does not highly affect the extent of the passive zone. However, the protection zone (ΔE_{prot}) drops up to null at 85°C. This fact indicates that material is passive at the corrosion potential. Nevertheless, if the steel already presents pitting corrosion before exposition to solution “old pits”, even a small grow of corrosion potential will cause them to get deeper. New pits, however, will not be formed.

Autoclave tests

The exposition of samples in autoclave at 120°C in solution 16 g/l NaCl + 2.24 g/l Na_2HPO_4 + 2.48 g/l NaH_2PO_4 during 8 hours did not show any surface attack.

Table 2. Calculated statistical parameters of current noise spectra
Material: AISI 316L
Solution: 16 g/l NaCl + 2.24 g/l Na_2HPO_4 +2.48 g/l NaH_2PO_4

T (°C)	Mean Current (mA /cm²) . 10^{-3}	Stantard Deviation,S,(.10^{-3})
25	3.15	1.14
60	6.0	6.4
85	34.2	30.4

Tabla 3. Statistical parameters of potential noise spectra
Material: AISI 316L
Solution: 16 g/l NaCl + 2.24 g/l Na_2HPO_4 +2.48 g/l NaH_2PO_4

T(°C)	Mean value V(mV)	Standard Deviation S	Noise Resistance R_n, KΩ.cm^{-2}
25	-62.3	47.5	18.12
60	-131.6	28.1	4.31
85	-379.4	28.6	1

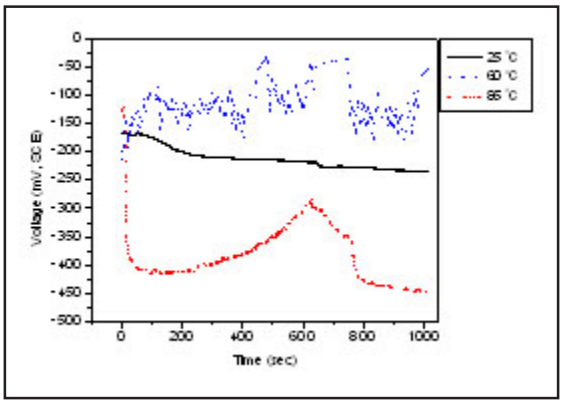

Figure 1. Time dependence of potential fluctuations for austenitic stainless steel AISI 316L in solution 16 g/l NaCl + 2.24 g/l Na_2HPO_4 + 2.48 g/l NaH_2PO_4 at 25, 60 and 85°C.

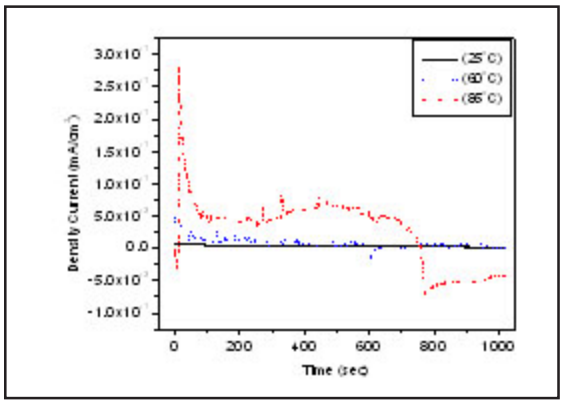

Figure 2. Time dependence of current fluctuations for austenitic stainless steel AISI 316L in solution 16 g/l NaCl + 2.24 g/l Na_2HPO_4 + 2.48 g/l NaH_2PO_4 at 25, 60 and 85°C.

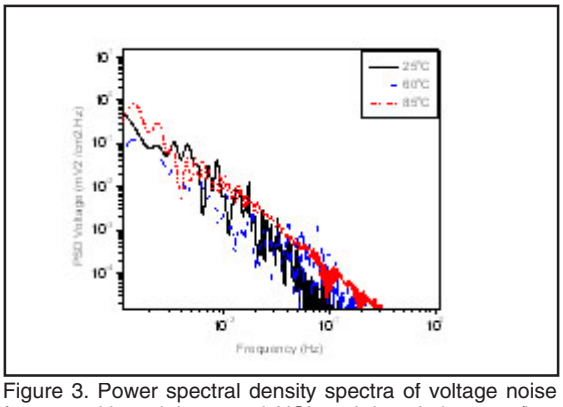

Figure 3. Power spectral density spectra of voltage noise for austenitic stainless steel AISI 316L in solution 16 g/l NaCl + 2.24 g/l Na_2HPO_4 + 2.48 g/l NaH_2PO_4 at 25, 60 and 85°C.

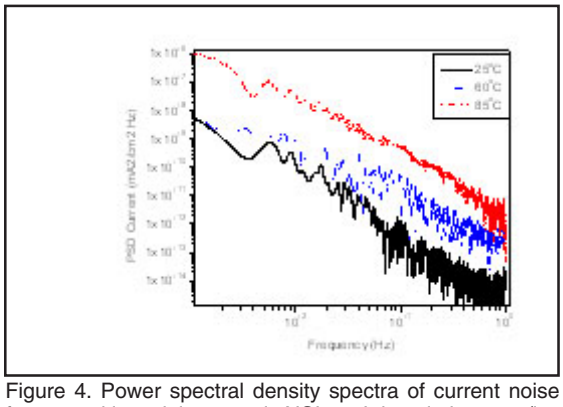

Figure 4. Power spectral density spectra of current noise for austenitic stainless steel AISI 316L in solution 16 g/l NaCl + 2.24 g/l Na_2HPO_4 + 2.48 g/l NaH_2PO_4 at 25, 60 and 85°C.

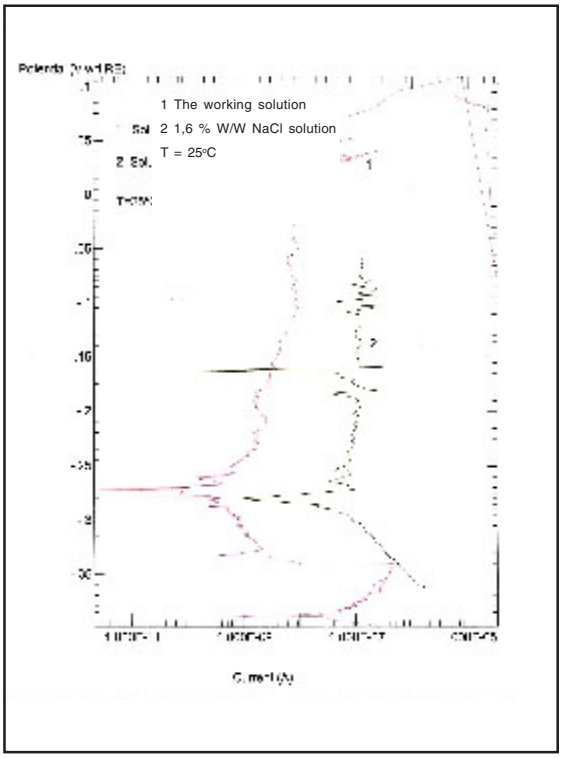

Figure 5. Polarization curve of AISI 316L austenitic stainless steel in 1,6 weight % NaCl solution and the working solution 16 g/l NaCl + 2.24 g/l Na_2HPO_4 + 2.48 g/l NaH_2PO_4 at 25°C.

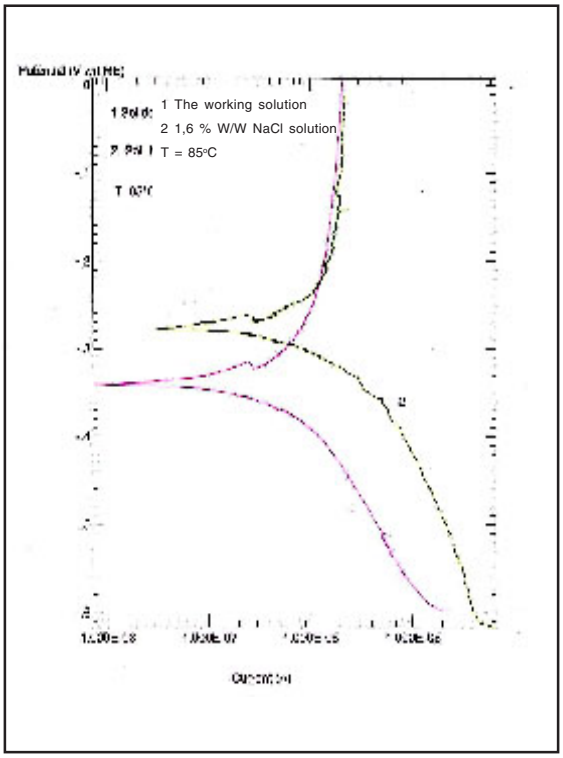

Figure 6. Polarization curve of AISI 316L austenitic stainless steel in 1,6 weight % NaCl solution and the working solution 16 g/l NaCl + 2.24 g/l Na_2HPO_4 + 2.48 g/l NaH_2PO_4 at 85°C.

Table 4. Dependence corrosion potentials vs. temperature for AISI 316L

Temperature (°C)	25	40	60	70	85
E_{corr} (NaCl sol.) mV_{SCE}	- 285	- 250	- 310	- 310	- 280
E_{corr} (Working Sol.) mV_{SCE}	- 275	- 425	- 445	- 445	- 340

DISCUSSION

Electrochemical noise

Time dependences for current noise show that observed fluctuations are given by prepitting events, i.e, metastable pits that repassivate spontaneously. The amplitude of current fluctuations in noise curves is in the range 1-10 μA at room temperature (figure 2). This behavior is in agreement with the effect cited in [5] on the development of metastable pits, which did not propagate additionally. Their depth is only about 0,1-1 μm , being harmless to the material. Nevertheless, in some given conditions these pits could destructively propagate. At 85°C the quantity of prepitting events is greater. The larger current amplitude (figure 2) should be associated to a certain weakening of the steel passive layer. On the other hand, current PSD dependences do not change their slope with the grow of temperature. Instead, they exhibit a shift towards values of spectral density, almost 3 orders higher (figure 4). This effect indicates a grow of the rate of pitting corrosion, according [7], where the influence of the transition from a passive system (carbon steel in a phosphate solution) to a pitted state (addition of chloride ions) was studied.

According [5] the number of events in current PSD curves increase with corrosion rate. Furthermore, from simulated data for stainless steel 316 in 0,1M NaCl, all the spectra is shifted towards higher values of density with the increase in the same order of such factors like the nucleation rate λ of

metastable pits , the mean value of current density I and the mean radius of pits. In fact, calculated in [6] PSD spectra of voltage and current noise show similar behavior to the obtained ones in this paper.

From the PSD dependence of voltage and current the spectral noise resistance R_{sn} is defined as

$$R_{sn} = [V_{FFT}(f) / I_{FFT}(f)]^{1/2} \quad (1)$$

where, $V_{FFT}(f)$ and $I_{FFT}(f)$ are the PSD voltage and current profiles, respectively, as it is shown in figures 3 and 4.

The obtained values for the spectral noise resistance R_{sn} are given in figure 5. The ratio $R_n = S_V / S_I$ which is defined as noise resistance in the Statistical method also shows a decreasing with the grow of temperature, in a similar way as the obtained R_{sn} values do.

Electrochemical noise resistance R_n has been proposed as a measure of the general and local corrosion rate [8,9]. According some authors it has a behavior similar to polarization resistance R_p. Therefore, electrochemical noise measurements should allow to perform a non-perturbative monitoring of corrosion kinetics. During the measurement no external potential is applied, whereas in the conventional R_p Test a slight polarization should be applied. From figure 7 a good agreement between R_n and R_{sn} values is obtained to describe the increase of corrosion process with temperature. The following relationship has been analytically demonstrated elsewhere [9] for electrodes with identical impedances $Z_1 = Z_2 >> R_s$, where R_s is the solution resistance.

$$R_n = Abs(Z(0)) = R_p = R_{sn}(0) \quad (2)$$

Z(0) y $R_{sn}(0)$ are the Impedance and spectral noise resistance at null frequency, respectively.

Similar behavior for electrochemical noise resistance R_n and the polarization resistance R_p was experimentally shown in [5] to describe the transition from a passive state to a locally corroded state, due to a chloride addition, although their respective absolute magnitude differ. Moreover, the action of the added chloride ions induces a decreasing of R_n. A threshold value for spectral resistance exists, under which the material in the installation becomes pitted. It follows that, if this value could be determined , then *on-line* monitoring is possible before pits could be visible.

Potentiodynamic Polarization

A study on the effect of temperature and potential on the inhibitive action of some oxoacid salts for pitting in chloride solutions has been reported elsewhere [10]. The influence of phosphate ions on the pitting corrosion of AISI304 stainless steel was included. According this paper phosphate inhibits efficiently this type of corrosion at high temperature (80 -150°C) in solutions 0,1 M de NaCl + 0.1 M (Na_2HPO_4 +NaH_2PO_4).

Nevertheless, authors suggest the possible development of pits in the above mentioned

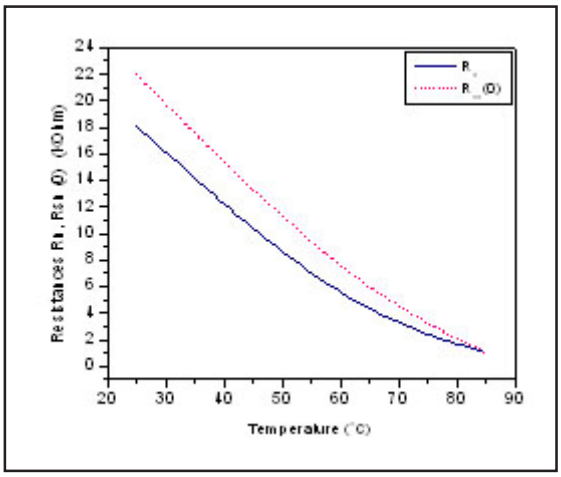

Figure 7. Temperature dependence of electrochemical noise resistance R_n and spectral resistance R_{sn} for austenitic stainless steel AISI 316L in 16 g/l NaCl + 2.24 Na_2HPO_4 + 2.48 g/l NaH_2PO_4).

solution at lower temperatures during the heating process, due to the poor protecting capacity of the resulting passive layer. Moreover, it should be underlined the risk of pitting initiation, due to a scarce concentration of passivating agent.
At the same time, sodium dihydrogenphosphate (NaH_2PO_4), which shows a neutral or slight acid hydrolysis, is not a real steel passivator. On the other hand, sodium hydrogenphosphate (Na_2HPO_4) is as good passivator as sodium phosphate (Na_3PO_4), despite the higher resulting solution pH for the last one [11].

Experimental data obtained from potentiodynamic tests (table 4) show that AISI 316L stainless steel does not develop pits in solution
16 g/l NaCl + 2.24 Na_2HPO4 + 2.48 g/l NaH_2PO_4 (pH = 6,45) at temperatures up to 85°C. The difference between Pitting and Corrosion Potential DE keeps nearly constant. Only the Protection Gap DE_{prot} decreases to cero at 85°C, i.e. , old pits will propagate. Instead, new ones will not appear. For this material anodic current at the passive potentials is higher in NaCl solution without phosphate addition. At the same time corrosion potential is more active.

CONCLUSIONS

1. Critical pitting temperature for austenitic stainless AISI 316L in solution
16 g/l NaCl + 2.24 g/l Na_2HPO_4 + 2.48 g/l NaH_2PO_4 (pH = 6,45) is higher than 85°C.
2. A good match of electrochemical noise resistance R_n and spectral resistance R_{sn} temperature dependences was found.

ACKNOWLEDGEMENTS

Authors wish thank Dr. Francisco Corvo, Head of Corrosion Department of Center for Scientific Research (CENIC) in Havana for his support to the achievement of electrochemical noise measurements.

REFERENCES

[1] HLADKY, K., JOHN, D.G., WORTHINGTON, S.E., HERBERT, D., Corrosion monitoring on stainless steel under condensing nitric acid conditions htp:// www.khdesign.freeserver.co.uk/noiseindex.htm
[2] HLADKY, K., DAWSON, J.L., Corrosion monitoring using low frequency electrochemical noise.
[3] HLADKY, K., DAWSON, J.L., The measurement of localized corrosion using electrochemical noise.
[4] OLDFIELD, J.W., Test techniques for pitting and crevice corrosion resistance of stainless steels and nickel –base alloys in chloride– containing environments. NiDI Technical Series No. 10 016.
[5] PISTORIUS, P.C., Design Aspects of Electrochemical Noise Measurements for uncoated metals: Electrode size and sampling rate, Corrosion Vol. 53, No. 4, April 1997.
[6] COTTIS, R., TURGOOSE, S., Electrochemical Impedance and Noise. NACE International, 1999.
[7] GUSMANO, G., et. al., Ëlectrochemical Noise Resistance as a tool for corrosion rate prediction". Corrosion, Vol.53, No.11(1997)860–868.
[8] BERTOCCI, U., et al., Noise resistance applied to Corrosion measurements. I Theoretical Analysis J. Electrochem. Soc. 144(1)(1997)31-37.
[9] BERTOCCI, U., et al., Noise resistance applied to Corrosion measurements. II Experimental Tests. J. Electrochem. Soc. 144(1)(1997)31-37.
[10] YASHIRO, H., et. al., Effects of Temperature and Potential on the Inhibitive Action of Oxoacid Salts for Pitting in High-Temperature Chloride Solutions, Corrosion, Vol.53 No.4 1997.
[11] Inhibidores de la Corrosión, Curso de postgrado, Maestría en Corrosión, CENIC, La Habana, 1998.

Received: December 16, 2003
Accepted: February 4, 2004

DEVELOPMENT OF A BETA IRRADIATOR FOR QUARTZ LUMINESCENCE ANALYSIS

Mariela Rodríguez Otazo, Arian Abrahantes Quintana, Rafael Díaz Valdés, Luis Baly Gil

Centro de Aplicaciones Tecnológicas y Desarrollo Nuclear (CEADEN), Calle 30 No. 502 e/ 5ta Ave. y 7ma, Miramar, Playa, Ciudad de La Habana, Cuba
arian@ceaden.edu.cu

DESARROLLO DE UN IRRADIADOR BETA PARA EL ANÁLISIS DE LA LUMINISCENCIA DEL CUARZO

Resumen

En el presente trabajo se describe el desarrollo de un irradiador beta de Sr/Y-90. El irradiador, diseñado para ser usado como parte de una instalación para el análisis de la luminiscencia del cuarzo, es capaz de depositar dosis con una velocidad de 100 mGy/s aproximadamente en una capa de granos de cuarzo de 150 μm. El diseño tiene en cuenta el por ciento permisible de dosis dado a una muestra adyacente no irradiada. La operación segura del irradiador se garantiza usando un cierre de seguridad que impide que el irradiador pase al estado abierto precipitadamente.

Abstract

In the present work the development of a Sr/Y-90 beta irradiator is described. Designed to be used as part of an installation for quartz luminescence analysis, the irradiator is capable to deliver doses in a 150 μm layer of quartz grains with a rate of approximately 100 mGy/s. The design takes into account the permissible cross-talk. The safe operation of the irradiator is assured by using a security lock, which prevents the irradiator to pass unadvisedly to an open state.

Key words: luminescence, measuring instruments, thermoluminescent dosemeters, strontium 90

INTRODUCTION

The photoluminescence of natural dosimeters (quartz, feldspars, Al_2O_3) is being widely used in dating and retrospective dosimetry [1-3]. Due the great variability in the composition of such natural materials, even within samples collected in the same place, the response to a given dose could differ significantly [4]. To overcome this drawback, it is necessary to construct a calibration curve for each sample. The complexity of such a procedure, which involves repetitive steps, has made crucial the development of automated readers [5,6].

The beta irradiator constitutes an essential element of these installations. The design of a beta irradiator should comply with four basic requirements. First, in order to be operable, the irradiator is radiologically safe. Second, for dating or retrospective dosimetric applications typical calibrations doses go from 50 mGy up to several Grays. Therefore, the time needed to deliver such a dose range depends in first place on the source activity. To make the irradiation time as short as possible, the irradiator should be capable of delivering a dose rate of approximately 100 mGy/s. There is a third requirement related to the fact that in the vicinity of the sample that is being irradiated, there are other samples that will receive a percent of the dose given to the first one (the cross talk). For a specific arrangement the cross talk should be less than 0.1-0.3%. Finally, to allow automated control, the irradiator should be opened and closed electronically.

Irradiator Design

The basic design scheme is presented in figure 1. A 22 mCi ^{90}Sr/Y source is mounted in a rotating metallic wheel. Turning around the wheel, the source passes from the upper position (closed) to the lower position (open). The wheel is surrounded by a shield to reduce the radiation output and serves as mechanical support.

An appropriated distribution of different materials is used to reduce the photon output to a minimum level. Using the MCNP-4A code, three different configurations were evaluated. These configura-tions were brass-lead, teflon-aluminum-brass-lead and graphite-brass-lead. In all the cases, an external 1 cm wide lead shield is considering. The overall irradiator dimensions are 106 mm diameter and 117 mm height.

As it is shown in the figure 2, the calculated photon output per emitted electron of the two last configurations is two times lower than the brass-lead configuration. Based on technological considerations the teflon-aluminum-brass-lead configuration was selected for further development.

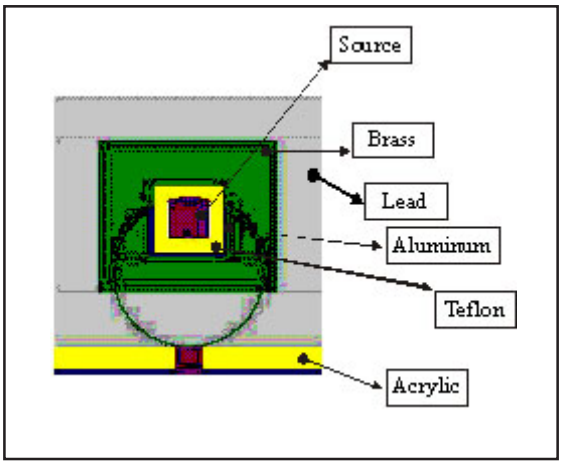

Figure 1. The basic design scheme.

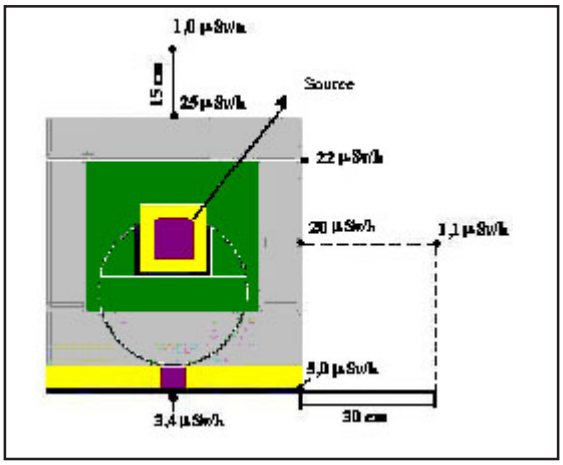

Figure 3.a) Measured dose rate. The irradiator is closed.

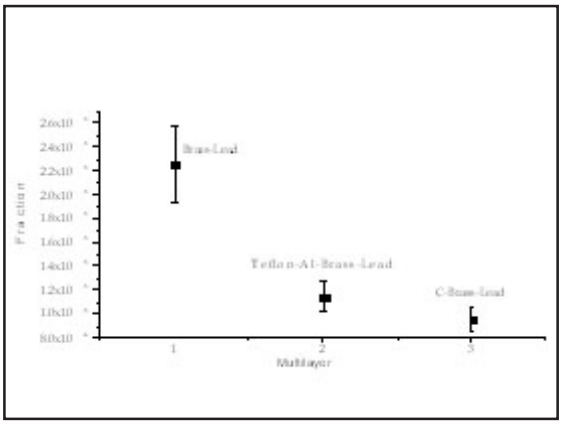

Figure 2. Photon output per emitted electron for different configurations.

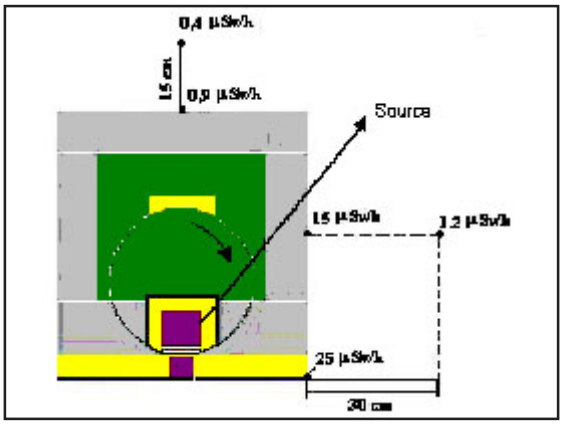

Figure 3.b) Measured dose rate. The irradiator is open.

Shielding Effectiveness

As any other radiation hazard instrument, there are a group of requirements that should be fulfilled. One of these requirements is to assure a permissible level of radiation emission. Figure 3 shows the measurements made in several points of the irradiator surface for the cases when the irradiator is open and when it is closed. The results indicate the sufficient shielding effectiveness of the irradiator.

In order to secure the irradiator operation a mechanical shutter has been introduced. This mechanism prevents the irradiator to pass without command to an open state. The irradiator also possesses a blinking red light indicating the open state of the irradiator. In case of power failure, the irradiator has a mechanism that allows the manual closing. Non-flammable materials are employed in the irradiator construction.

Dose Rate and Cross-Talk

For dating or retrospective dosimetric applications typical calibrations doses go from 50 mGy up to several Grays. The time needed to deliver such a dose range depends in first place on source activity. For such a reason the selection of a proper activity will determine the time efficiency of the sample calibration process. Figure 4 shows the results of the simulation made with the MCNP code of the dose given to a 150 µm mono-layer of quartz laying over a steel disc, when a 30 mCi ^{90}Sr/Y source is used. The graphic indicates a calculated dose rate of 10 mGy/s, which seems low if it is compared with similar arrangements.

To validate the simulation procedure, was carried out an experiment in which the quartz was replaced by GR-200 (LiF,Mg,Cu,P) thermoluminescence dosimeters. Using a reference source, the GR-200 chips were primarily calibrated and then they were irradiated using our irradiator and the TL response was subsequently determined. The results of this study together with the results of the simulation of the dose delivered to these dosimeters are presented in figure 5. As it is observed, the calculated dose resulted to be lower than the experimental value. Later analysis of this result indicates that an underestimation of the source activity has been made due to a wrong geometrical factor.

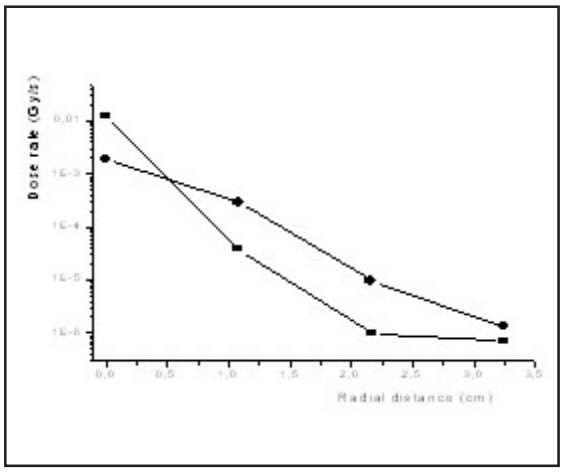

Figure 4. Dose rates vs. radial distance up to the center of the quartz sample. ● Samples are 5 mm below the bottom of the irradiator. ■ Central sample is 10 mm over the bottom, the rest as in the previous case.

Even when the simulation, as it has been made, has a limited value to estimate the absolute dose rate, an estimation of the dose given to quartz samples can be done if the mismatch between the experiment and the simulated value for the dose given to GR-200 (4.72) is extrapolated to the case of quartz samples. In that case the dose rate for quartz would be approximately 58 mGy/s. Such a value is much more alike to the expected one.

In the other hand, the simulation has a great value to assess the cross-talk, i.e. the percentage of dose given to an adjacent non-irradiated sample. Cross-talk can be extracted from figures 4 and 5, specially from cases when the central sample is inside the irradiator aperture. Those are the closest to the real configurations, since the samples are planed to be lifted from a multi-sample holder up to the irradiation position inside the irradiator.

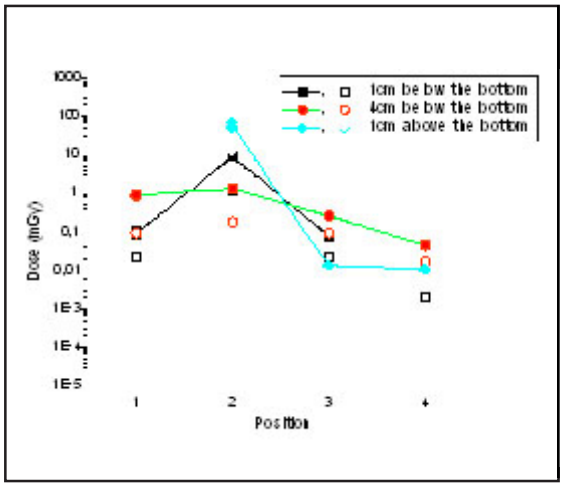

Figure 5. Dose vs. GR-200 horizontal position. Position 1(- 18.8 mm), position 2 (0 mm), position 3 (18.8 mm), position 4 (37.5 mm). Filled symbols represent experiment, unfilled symbols represent the simulation.

The results of the evaluation of the cross-talk are presented in the table. As it is observed, in all the cases the results satisfy the requirement presented above. The significant differences between the results between quartz and the GR-200 are due to certain differences in the experimental conditions. In the real situation the conditions will be closer to the case of the experiment of the GR-200.

Irradiator cross-talk. The position of the samples in the experiment and in the simulation is the same than in the planed installation

Source of calc.	1st adjacent sample %	2nd adjacent sample %
Quartz (simulation)	0.31	0.008
GR-200 (simulation)	0.003	-
GR-200 (experiment)	0.022	0.007

The analysis of figures 4 and 5 allows concluding he convenience of the sample lifting to increase the dose rate while the cross-talk is reduced. For example, according to the results presented in the figure 4, the dose rate in the position of the lifted sample is almost a order higher, while the cross-talk is 50 times lower.

Electronic control

A servomotor has been added to perform the open-close operations. The time used by this system to complete the operation is 1-1.5 s. This system is crucial to perform the electronic control of the irradiator.

CONCLUSIONS

The presented design has proved to meet all the requirements presented to any instrument in its class. It also complies with the needs of the specific destination for which it was designed. Moreover, from the analysis of the dose distribution several recommendations have arisen to the design of the whole installation.

REFERENCES

[1] HOROWITZ, Y.S., Thermoluminescence and Thermoluminescent Dosimetry, Vol. III (CRC Press, Boca Raton) 1983.

[2] BOTTER-JENSEN, L., Development of Optically Stimulated Luminescence Techniques using Natural Minerals and Ceramics, and their Application to Retrospective Dosimetry, Riso National Laboratory, Roskilde, Denmark, 2000.
[3] BOTTER-JENSEN, L., MURRAY, A.S., Optically stimulated luminescence techniques in retrospective dosimetry, Radiation Physics and Chemistry 61 (2001)181-190.
[4] MURRAY, A.S., WINTLE, A.G., Luminescence dating of quartz using an improved single-aliquot regenerative-dose protocol., Radiation Measurements 32(2000)57-73.
[5] BOTTER-JENSEN, L., BULUR, E.G, DULLER, A.T., MURRAY, A.S., Advances in luminescence instrument systems, Radiation Measurements 32(2000)523-528.
[6] BOTTER-JENSEN, L., MEJDAHL, V., MURRAY, A.S., New light on OSL, Quaternary Geochronology 18(1999)303-309.

Received: December 16, 2003
Accepted: February 4, 2004

REVISTAS NUCLEARES DE IMPACTO

· ANNUAL REVIEW OF NUCLEAR SCIENCE (5.471)*

· JOURNAL OF NUCLEAR MEDICINE (4.015)

· RADIOLOGY (3.800)

· NUCLEAR PHYSICS B (3.722)

· EUROPEAN JOURNAL OF NUCLEAR MEDICINE (2.690)

· ATOMIC DATA AND NUCLEAR DATA TABLES (2.545)

· NUCLEAR FUSION (2.475)

· INTERNATIONAL JOURNAL OF RADIATION ONCOLOGY BIOLOGY PHYSICS (2.321)

· RADIATION RESEARCH (2.314)

· PHYSICAL REVIEW C-NUCLEAR PHYSICS (1.842)

· NUCLEAR PHYSICS A (1.821)

· ANTIBODY IMMUNOCONJUGATES AND RADIOPHARMACEUTICALS (1.800)

· RADIOTHERAPY AND ONCOLOGY (1.799)

· AMERICAN JOURNAL OF NEURORADIOLOGY (1.733)

· ADVANCES IN RADIATION BIOLOGY (1.714)

· SEMINARS IN NUCLEAR MEDICINE (1.603)

· PROGRESS IN PARTICLE AND NUCLEAR PHYSICS (1.354)

· ZEITSCHRIFT FUR PHYSIK A-HADRONS AND NUCLEI (1.326)

· RADIOLOGIC CLINICS OF NORTH AMERICA (1.316)

· JOURNAL OF NUCLEAR MATERIALS (1.264)

· NUCLEAR INSTRUMENTS & METHODS IN PHYSICS RESEARCH SECTION A-ACCELERATORS SP (1.188)

· IEEE TRANSACTIONS ON NUCLEAR SCIENCE (1.183)

· JOURNAL OF PHYSICS G-NUCLEAR AND PARTICLE PHYSICS (1.142)

· NUCLEAR MEDICINE AND BIOLOGY (1.132)

· NUCLEAR MEDICINE COMMUNICATIONS (1.078)

· RADIOGRAPHICS (1.078)

· CARDIOVASCULAR AND INTERVENTIONAL RADIOLOGY (1.073)

· NUCLEAR INSTRUMENTS & METHODS IN PHYSICS RESEARCH SECTION B-BEAM INTERACTION (1.073)

( )* **Factor de Impacto**

Instrucciones A Los Autores

PARA PUBLICAR EN CIENCIAS NUCLEARES

Los artículos deben tener una extensión máxima de 10 cuartillas incluidas tablas (un máximo de 5) e ilustraciones (un máximo de 5). Se entregarán en disquete, en Word y en Arial 11. El total de líneas por páginas es 30 como máximo.

Los artículos tendrán el siguiente orden: Resumen (en español e inglés), Introducción, Materiales y Métodos, Resultados, Discusión, Conclusiones, Recomendaciones (opcional), Agradecimientos (opcional), Referencias Bibliográficas y Bibliografía Consultada. Estas secciones deben estar bien definidas, aunque no necesariamente con subtítulos.

Los artículos están sujetos a arbitraje y a la aprobación del Consejo Editorial.

Autor (es): Especificar nombres y dos apellidos así como la institución de procedencia. Los autores deben enumerarse por orden en relación con los experimentos e investigaciones realizadas.

Título: No debe exceder de 100 letras, o 15 palabras, ni contener abreviaturas, fórmulas químicas, ni nombres patentados (en lugar de genéricos). Debe aparecer en español e inglés.

Resumen: No debe exceder de 150 palabras, ni contener siglas, abreviaturas ni referencias bibliográficas. Debe aparecer en pretérito, en español e inglés.

Introducción: Exponer con toda la claridad posible, la naturaleza y alcance de la investigación, revisar las publicaciones pertinentes, indicar el método de investigación si se estima necesario, mencionar los principales resultados de la investigación y expresar la conclusión o conclusiones principales sugeridas por los resultados.

Materiales y Métodos: La mayor parte de esta sección debe escribirse en pasado y dar toda clase de detalles. La finalidad principal es describir y que los resultados sean reproducibles. En los materiales hay que incluir las especificaciones técnicas y las cantidades exactas, así como la procedencia o el método de preparación. Se deben emplear los nombres genéricos o químicos.

Resultados: Debe hacerse una descripción amplia, clara y sencilla de los experimentos, ofreciendo un panorama general pero sin repetir los detalles experimentales de los Materiales y Métodos. Se deben presentar los datos más representativos. La exposición debe redactarse en pretérito.

Discusión: Deben presentarse de forma expositiva los principios, relaciones y generalizaciones que los Resultados indican. Se deben señalar las excepciones o las faltas de correlación y delimitar los aspectos no resueltos. Mostrar cómo concuerdan (o no) los resultados e interpretaciones con los trabajos anteriormente publicados. Deben exponerse las consecuencias teóricas del trabajo y sus posibles aplicaciones prácticas. Resuma las pruebas que respaldan cada conclusión. Los tiempos verbales oscilarán entre el presente y el pasado.

Conclusiones: Deben formularse lo más clara posible. Pueden estar incluidas en la Discusión.

Recomendaciones (opcional)

Agradecimientos (opcional): Se debe agradecer cualquier ayuda técnica importante recibida de cualquier persona que haya colaborado en el trabajo, experimento, o provisión de equipos, materiales especiales, y otros. Pueden utilizarse frases como «doy las gracias a ...»

Referencias bibliográficas: Deben enumerarse solo obras importantes y publicadas. Si una referencia parece absolutamente esencial, se podrá añadir al texto entre paréntesis o como nota de pie de página. Deben cotejarse todas las partes de cada referencia contra la publicación original antes de presentar el artículo. Las referencias en el texto deben hacerse con números entre corchetes en el lugar en que se apliquen y siguiendo un orden consecutivo.

Bibliografía consultada: Deben ordenarse alfabéticamente con números arábigos entre corchetes al final del trabajo. Los títulos de las publicaciones periódicas deben adecuarse al sistema INIS (véase EAEA-INIS-11). No deben incluirse las referencias a trabajos no publicados.

Abreviaturas, siglas y símbolos: Deben ser los aceptados internacionalmente. Las abreviaturas y siglas deben explicarse la primera vez que se mencionan. Los símbolos y caracteres griegos, al igual que los subíndices y supraíndices, deben definirse claramente.

Tablas: Deben ordenarse con numeración arábiga e incluirse al final del trabajo. Los términos, las abreviaturas y los símbolos utilizados en las figuras deben ser los mismos que aparecen en el texto. No utilice caracteres, ni símbolos poco frecuentes (son preferibles los círculos, cuadrados o triángulos en blanco o rellenos). Si son muy complejos deben aclararse en una leyenda concisa. Los símbolos y caracteres deben ser claros y de tamaño suficiente, de manera que al reducirlos para la publicación sean legibles.

Ecuaciones y fórmulas: Deben escribirse con precisión, en especial los subíndices y supraíndices. Evite el uso de exponentes complicados y la repetición de expresiones elaboradas.

Unidades: Como norma general deberá emplearse el Sistema Internacional de Unidades y prescindir de símbolos y abreviaturas inadecuados.

PARA PUBLICAR EN OTRAS SECCIONES

Los artículos de las demás secciones de la revista deben tener como objetivo la difusión, con rigor científico y de forma asequible al público en general, de temas relacionados con la energética nuclear, las diversas aplicaciones de las técnicas nucleares, la seguridad nuclear, la protección radiológica, salvaguardias y no proliferación, energía nuclear e información pública, entre otros. Los trabajos no deben exceder las 10 cuartillas, incluidas ilustraciones y tablas. En las tablas e ilustraciones se seguirán las mismas indicaciones que rigen para los artículos de la sección Ciencias Nucleares. Las secciones son las siguientes: Panorama Nuclear, Ámbito Regulatorio, Salvaguardias y No Proliferación, En la Espiral e Innovación Tecnológica.

Los artículos están sujetos a la aprobación del Consejo Editorial.

INFORMACIÓN GENERAL

Los trabajos que no se acepten se devolverán al autor.

Los autores recibirán de forma gratuita un ejemplar de la revista donde aparece publicado su artículo.

VÍAS DE PRESENTACIÓN

En la redacción de la revista:
Calle 20, No. 4111-4113 e/ 18A y 47, Playa, Ciudad de La Habana, Cuba
correo electrónico: nucleus@cubaenergia.cu